MID-INFRARED AND TERAHERTZ FREQUENCY COMBS FROM QUANTUM CASCADE LASERS

by

Nathan Charles Henry

A dissertation submitted to Johns Hopkins University in conformity with the requirements for the degree of Doctor of Philosophy

Baltimore, Maryland

August 2020

Abstract

Optical frequency combs (FC) allow for extremely high resolution and broadband spectroscopic measurements that are captured contemporaneously rather than through some scanning action. Spectroscopic access to the infrared and THz is highly coveted as many molecular resonances lie in this region. However, due to a lack of available materials, emission of FC in the IR has been difficult, with many attempts resulting in low power and efficiency. In 2014 [1] the first mid-IR FC was characterized from a free-running QCL, requiring no extra elements. However, due to the inherently short upperstate lifetime of the laser, the FC is atypical in that it is not characterized by pulses but rather frequency modulation (FM). While the QCL FC has advanced significantly, it is not fully understood. As a result, spectroscopic measurements can become unreliable, sensitive to environmental changes, and recovery of absolute frequency can be difficult.

To better understand the FC QCL, a set of rate equations adapted from the optical Bloch equations is developed and found to be fully adequate for describing the origins and dynamics of FM FC. This work addresses two modes of operation (pseudo-random and chirped FM) calculating the dynamics of a QCL modeled after real-world measurements. Using specifications of real world QCLs (THz and IR), the gain is modeled under various operational scenarios and the most efficient state is identified. The period of the FM is postulated to be determined by the relative strengths of the various hole burning mechanisms and stability is shown for multiple regimes.

Further work is presented addressing the stability of QCL FCs. We begin by deriving the linewidth of the FC generating QCL and show that indeed it can be just as narrow as more conventional FCs. Subsequent to this work we use a two-dimensional model to achieve an engineered power-law dispersion, which can mitigate offset frequency drift offering the potential to significantly lower the phase noise. It is the hope of the author that this research will be used to develop a deeper understanding of FC producing QCLs that contribute to many fields of human endeavor such as medical diagnostics, remote sensing, time standardization, etc.

Thesis Committee

Jacob B. Khurgin (Primary Advisor)

Professor

Department of Electrical and Computer Engineering

Johns Hopkins Whiting School of Engineering

Susanna M. Thon

Assistant Professor

Department of Electrical and Computer Engineering

Johns Hopkins Whiting School of Engineering

Amy Foster

Associate Professor

Department of Electrical and Computer Engineering

Johns Hopkins Whiting School of Engineering

Acknowledgements

I would like to acknowledge all the support my advisor Professor Jacob Khurgin has provided me, without whom all this would obviously not have been possible. Most often, I quite enjoyed our meetings together regardless of whether we were actually working or just “waxing philosophically”. I would also like to thank Professor Sanjay Krishna who first introduced and guided me through the world of semiconductors and optoelectronics. I would be remiss to forget to mention Professor Pinot Noir of course who provided the opportunity for many thoughtful head scritches throughout my PhD. Along those lines I must also mention our other canine lab member, my companion for 12 years, Caine who spent countless hours waiting patiently under my desk in the hopes we would go to Wyman Park soon. I appreciate the patience and support of my wife Samantha as I went through all stages of the graduate school struggle.

Last but not least, thanks to my mother who always pushed me to learn.

Table of Contents

List of Tables

List of Figures

Chapter 1. Introduction

Optical frequency combs (FCs) have been an exciting subject of investigation and maintain a healthy growth of publications, nearing 20k, due to their countless, obvious and undiscovered, applications in metrology and spectroscopy. Their development in the late 90s owed great thanks to Theodor Hansch and John Hall who shared the 2005 Nobel prize in physics [2, 3]. They have truly revolutionized the precision at which we can measure time, frequency and distance. Impressive advancements have been achieved, in the visible and near-IR spectrum enabling for highly accurate, and rapid measurements. Due to lack of viable materials, the technology has room for development in the infrared (IR) and terahertz (THz) spectral regions which are of particular interest in the world of spectroscopy. While there are various methods available to access these regions, they typically rely on nonlinear frequency conversion which results in lower power and sub-par conversion efficiency, the most promising platform is the quantum-cascade laser (QCL).

QCLs are a dominant technological force for coherent radiation in the mid-IR and THz spectral regions. Frequency combs are typically a result of a coherent pulse train, however, due to their inherently low upperstate lifetimes it is very hard to achieve mode-locking in QCLs, a result of the round trip time, τ_{rt}, being shorter than the upper state lifetime of the laser τ_{21}. In a typical QCL the upper state lifetime is on the order of ~1ps with a cavity roundtrip time of ~100ps. Despite this, the broadband QCL was shown to emit FCs with a stable phase relation in the mid-IR[1][] and THz [4]. Subsequent to this discovery, a frequency domain model was developed [5] and concluded that as the laser oscillates, the broadened gain of the free running

QCL causes multimode operation due to spectral and spatial hole burning; in order to maintain continuous wave operation, necessitated by its fast saturable gain, the QCL must emit a frequency modulated (FM) light Using a perturbative solution of the Maxwell Bloch equations, a modeled spectra of the FC was produced with a strong beat-note, continuous wave operation, and a frequency modulation signal that appeared “pseudo-random”. While the model accurately predicted the spectral signature of a multi-mode laser with a short gain recovery time, it did not explain the characteristics of the FM signal, i.e. why it appeared to be pseudo-random yet periodic with the round trip time. Thus a new time-domain model is developed here and laser dynamics are investigated as a continuation of this previous work.

Intersubband Transitions

An important distinguishing feature of the QCL is that it operates on intersubband transitions (IST) rather than interband transitions. The key to the importance here is that, unlike interband transitions, ISTs can cover many different wavelengths (including IR and THz) while using robust III-V materials rather than exotic materials such as HgTe or PbSe, which come with many challenges. An enabling technology called molecular beam epitaxy (MBE) provided accurate crystal growth down to the atomic layer, and was pioneered by J.R. Arthur and J.J. Lepore [6] in the early 1970s at Bell telephone labs, and even further mastered by A.Y. Cho opening up a flood of quantum engineered devices [7]. The first observation of the intersubband transition was realized by Tsui and Gornick in an electron gas heated by current in an Si/SiO_2 inversion layer[8]. The first intersubband absorption was observed in 1985 by West and Eglash [9] in a GaAs/AlGaAs multi-quantum well, demonstrating the large dipole matrix element and the most important characteristic, that the energy can be tuned by changing the quantum well width.

The first efficient intersubband detector (dubbed QWIP – quantum well infrared photodetectors) was developed at Bell Labs by B. Levine [10] and quickly grabbed the attention of scientists as an actualization of the usefulness of ISTs. Less than a decade later the first intersubband laser was developed, the QCL [11].

As shown in Figure 1 below, if the two materials comprising the quantum well exhibit a type I alignment (Figure 1a.), where the conduction and valence bands of the well material is nested inside the bandgap of the barrier material, the transition energy is determined by the well material as well as the confinement state of the electron and hole. A typical material system for this is GaAs/AlGaAs. If however the transition occurs between the two conduction band envelope functions (Figure 1b.) quantized by the well, it is considered an intersubband transition with an energy that is inversely proportional to the square well width, as shown in equation (0.1), this is typically achieved with ternary and quaternary, III-V materials. Thus the transition energy can be engineered to the desired wavelength

$$E_n = \frac{n^2 \pi^2 \hbar}{2mL^2} \quad , \qquad (0.1)$$

where n is the energy level integer, m is the mass of the carrier, L is the width of the quantum well and $\hbar$ is Planck's constant. Confinement on the scale of tens of angstroms will results in energies in the 100's of meVs for infrared radiation and even smaller for THz radiation.

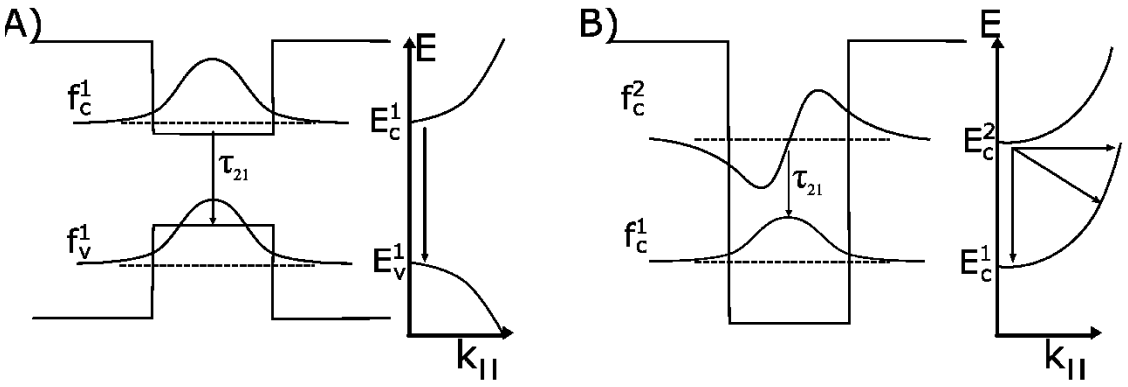

Figure 1- 1 A.) Bipolar, interband transition in a type I quantum well, the transition energy is determined by the material of the well and localization of the electron and holes. B) Unipolar, intersubband transition (IST) where the energy depends solely on the confinement of the quantum well. The dispersion diagram indicates the many possible scattering scenarios (arrows) resulting in a short upperstate lifetime (τ_{21}), this nonradiative transition happens through various processes under the constraint that momentum and energy are conserved.

There are a few consequences to an IST based device that should be discussed. As indicated in the dispersion graph of Figure 1-1b, due to the almost equal curvature of the sub-bands many states are not separated by an energy gap and elastic or inelastic transitions with the proper momentum-exchange will result in scattering to the lower state as signified by the arrows in Figure 1-1, thus the lifetime of the upper lasing level (τ_{21}) is dramatically reduced. There are many various types of scattering transitions, a few will be covered here. Intrasubband scattering, in that scattering occurs in a single band, contributes to carrier thermalization and level broadening however the time scales at which this occur are in the femtosecond scale and thus all bands are typically considered to reside in thermal equilibrium. Intersubband scattering also occurs on a very fast time scale (picoseconds) however its effect on laser performance is unavoidable and consideration must be taken. Intersubband scattering depends on the overlap of the two wave functions, as defined by Fermi's golden rule, as well as the momentum

exchange involved. Thus these scattering rates can be engineered to achieve population inversion in the QCL. While there are many various scattering mechanisms that occur, the three most prevailing are longitudinal-optical phonons (LO), interface-roughness (IFR) scattering, and alloy-disorder (AD) scattering. LO and transverse optical (TO) phonons are elastic waves that propagate in the material and are comprised of vibrations between the cations and anions of the material. They are referred to optical phonons as their resonant energy resides in the optical spectrum due to the movements between atoms being out of phase. Phonons can couple with electrons resulting in transfer of energy and momentum. Skipping the derivation, we can intuitively assume that as the separation between bands approaches the resonant energy of the LO phonon the rate of phonon scattering will increase. This attribute can be used to engineer the laser level lifetimes, as a large separation will increase lifetime (up to a few pico seconds) and a small separation could give a lifetime in the femtoseconds, desirable for quick depopulation of a level. Diagonalization of the two levels, decreasing overlap of the wave functions, is another way to increase lifetime and is often incorporated in THz designs, this however will also reduce the gain. Alloy-disorder and interface roughness [12] scattering are similar processes. Alloy-disorder scattering typically occurs in ternary or quaternary materials such as AlGaAs or InGaAsP, and occurs due to the introduction of aperiodicity into the crystal potential. Similarly interface roughness refers to the smoothness of the barrier walls in the quantum well. Both scattering mechanisms can be taken advantage of in order to favorably control the electron transport [13].

As a result of the almost equal curvature of the intersubbands, the joint density of states is a delta function resulting in quasi-atomic like optical transitions. Essentially the gain

and absorption lines are broadened solely by scattering and nonparabolicity of the two bands. Unlike typical interband lasers, absorption does not occur for energies greater than the gap and the system is transparent at higher and lower energies, as a consequence QCLs have the ability to propagate short and longer wave radiation without absorption. This has many interesting consequences, the most obvious being that it becomes uniquely suited for multi-mode emission as ubiquitous absorption at higher energies does not occur as it does in interband operation.

Lastly, ISB transitions are known to have an extremely large dipole matrix element, a result of the band mixing that occurs in a quantum well. In a zinc-blende lattice the lowest conduction band is a result of mixing between an anti-bonding S and bonding P state. In addition we can take into account spin-orbit coupling and end up with a band diagram as shown in Figure 2b, where the conduction band is a result of mixing between the S and P orbitals (see Figure 2a) and the 3 valence bands, heavy hole (HH), light hole (LH), and split off (SO) are a mixing of p orbitals including parallel and antiparallel orbital coupling.

Dispersion for the conduction band can be calculated as a mixing of the CB with the LH and SO, resulting in an effective mass for the conduction band of

$$m_c^{-1} = m_0^{-1}\left(\frac{\mathrm{E}_P(\mathrm{E}_g + 2\Delta/3)}{\mathrm{E}_g(\mathrm{E}_g + \Delta)} + 1\right) \quad (0.2)\,,$$

where Δ is a spin orbit splitting energy (0.4eV for GaAs), and Ep is related to the momentum dipole moment $E_P = 2P^2 / m_0$. However, when this material is sandwiched into a quantum well, the effective masses of all bands become different than their bulk counterparts.

Most notably, the effective mass in the conduction bands confined in the quantum well is now dependent upon the energy as well as a coordinate of the material.

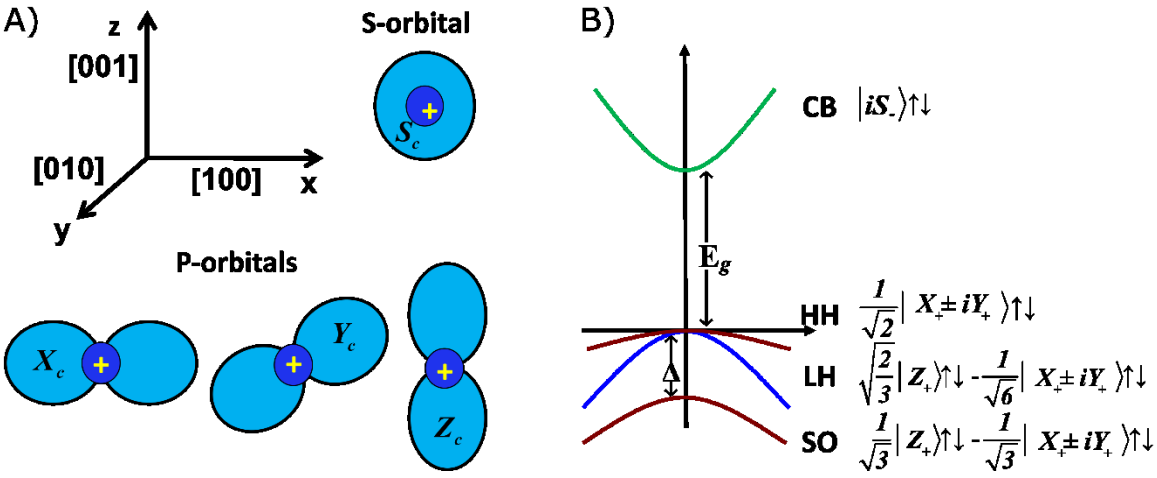

Figure 1- 2 A). Illustration of S and P orbitals and the state variable labels. B) Band dispersion of a III-V zinc blend crystal and the hybridization of the states as derived by k.P method.

Careful derivation reveals that the wavefunction of the conduction band is a mixing of the CB with the light hole and split off bands. The CB does not mix with the HH band due to the projection of its orbital momentum. Thus the wave function is represented as a combination of envelope functions (f_{nm} , see Figure 1-1) and Bloch functions u_n :

$$\Psi_c^m(\mathrm{k}_\perp,\mathrm{r}) = \sum_{n=1}^{3} f_n^{(m)}(z) u_n(\mathrm{r}) e^{i\mathrm{k}_\perp\cdot\mathrm{r}_\perp} = \left[f_c^m(z)\left|iS_-\uparrow\downarrow\right\rangle + f_l^m\left|Z_+\uparrow\downarrow\right\rangle + f_s^m\left|\left(\pm X_+ + iY_+\right)\downarrow\uparrow\right\rangle\right] e^{i\mathrm{k}_\perp\cdot\mathrm{r}_\perp}$$

(0.3),

Where n is either c, l or s for conduction, light hole, or spin off and u_n is the basis states for these bands: $\left|iS_-\uparrow\downarrow\right\rangle$, $\left|Z_+\uparrow\downarrow\right\rangle$,and $\left|X_+ + iY_+\uparrow\downarrow\right\rangle$ respectively, see Figure 1-2. Solving the characteristic equation relates the envelope functions and reveals that m_c is now the energy

dependent effective mass of the conduction band including a small modification from splitting in the valence bands,

$$m_c^{-1}(\mathrm{E}_c^{(m)}) = m_0^{-1}\left(\frac{\mathrm{E}_P(\mathrm{E}_g + \mathrm{E}_c^{(m)} + 2\Delta/3)}{(\mathrm{E}_g + \mathrm{E}_c^{(m)})(\mathrm{E}_g + \mathrm{E}_c^{(m)} + \Delta)} + 1\right). \quad (0.4)$$

While in all practicality this changes the effective mass of the conduction band very little, this mixing becomes important when considering a transition from one conduction band to another. When calculating the momentum dipole moment between two conduction bands, confined in a quantum well, for a TM polarized wave (considering only the Z direction) we arrive at the simple equation

$$p_{12,z} = -i\hbar \,,,_c \qquad \frac{\partial f_c^{(2)}}{\partial z} dz = \frac{m_0}{m_c} p_{12,z}^{*} \quad (0.5)$$

Where $p_{12,z}^{*}$ is a quasi-matrix element of envelope wavefunctions, and does not include mixing. We know the effective mass m_c, of III-V semiconductors if very small ($0.067m_0$ for GaAs) showing indeed how strong the dipole moment is for an IST. Performing a similar calculation for a TE wave (X and Y directions) results in a very small dipole moment, and would have been zero if not for the spin-orbit interaction. TE absorption does occur in doped quantum wells as free carrier absorption however.

While it is true that ISTs are very strong, the origin of this property can be shown to simply be a result of the small amount of energy typically involved in ISTs, which inherently is desired for access to infrared and terahertz spectra. This reasoning is readily illustrated when considering the strength of ISTs in GaN and an interband transition in InGaAs at 1.55 μm, the

dipole moments are essentially equal. If we turn to the oscillator sum rule for an allowed transition:

$$\frac{2}{m}\frac{p_{12}^2}{E_{12}}+\frac{m}{m_c}=1 \tag{0.6}$$

we can substitute the momentum dipole moment and approximate that

$$\omega_{12}z_{12}^2 \approx \hbar \tag{0.7}$$

and the dipole moment of the band to band transition can be estimated as

$$z_{cv} \sim P_{cv}\hbar \qquad \left(\frac{\hbar}{2m_c \mathrm{E}_g}\right)^{1/2} \tag{0.8}.$$

Rewrite the sum rule, substituting for the effective mass in equation (0.2) and

$$z_{12}=\sqrt{\frac{\hbar}{2m_c\omega_{12}}} \qquad \sqrt{\frac{\hbar}{m_0^2\mathrm{E}_g\omega_{12}}} \qquad \frac{\hbar}{m_0\mathrm{E}_g\sqrt{\hbar}} \qquad \sqrt{\frac{\mathrm{E}_g}{\mathrm{E}_{12}}} \tag{0.9}.$$

This eloquently illustrates what was stated earlier, ISTs have a large dipole moment is because they involve relatively small energy. Thus, ISTs are perfectly suited for accessing electromagnetic radiation at small energies (i.e. IR and THz) and their ability to engineer wavelengths using robust and fundamental III-V materials offer a significant advantage over much more challenging material such as HgCdTe.

Quantum Cascade Lasers

Laser action in semiconductors was first demonstrated in 1962 by research groups out of General Electric, MIT and Bell Labs [14], where coherent, infrared (IR) light was stimulated by a gallium arsenide diode. Progress after that was rapid with various heterostructure designs consisting of bipolar, stimulated emission. Emission in the long wave was limited due to a lack of materials, however, the solution came with superlattices and intersubband transitions as investigated in 1971 by Kazarinov and Suris [15]. A superlattice is a periodic repetition of type I or type II quantum wells, as defined earlier. The periodic alteration of the conduction band resembles a Kronig-Penney approximation of a periodic lattice forming sub-bands that can be engineered by the thickness of the constituent layers. In 1993 Gang Sun and Jacob B Khurgin established the feasibility of an intersubband, four-level laser comprised of a repeating superlattice of four quantum wells per period [16]. These demonstrations and technical capabilities developed into the first realization of the QCL in 1994 [11], by a team of researchers working at Bell labs. The active region of a QCL is a superlattice of alternating materials, such as GaAs and $Al_{0.15}Ga_{0.85}As$, commonly grown using MBE. The operation of the laser is engineered by designing the thickness of these layers, which are grown thin enough that quantum effects dominate.

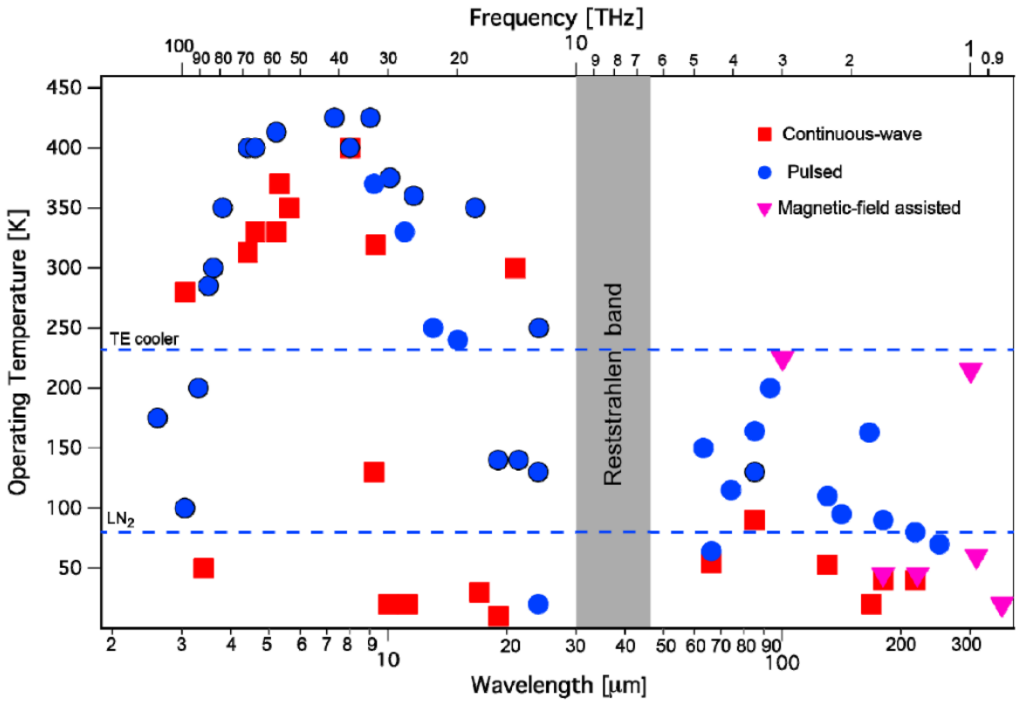

Figure 1- 3. Plot of quantum cascade laser operating temperatures versus wavelength/frequency of emission [17].

Because of this, the QCL has no theoretical limit in wavelength, while in reality the shortest wavelength is limited by the maximum conduction band offset between two materials and the longest wavelength being limited by thermal back filling of the carriers. Additionally the Reststrahlen band limits emission as shown in Figure 1-3, this region is material specific and is where the electromagnetic field interacts with the lattice vibrations (phonons) resulting in absorption. Nevertheless, Figure 1-3 shows an impressive range of spectral coverage by the QCL, under 3um all the way to THz at 450 um [17]. , Not shown is AlGaN/GaN material systems working towards the telecom band (1550nm) [18]. Continuous wave, room temperature operation of QCLs was achieved in 2002 [19] and room temperature operation has now been reported all the way up to $>17\mu m$. The first THz QCLs were realized almost simultaneously in

2002 at Scuola Normale Superiore [20] and at MIT [21]. THz QCLs have now been reported to emit all the way up to 190K [22], however the goal of room temperature operation remains elusive. QCLs have established themselves as the staple semiconductor laser source and are widely utilized in many laboratories. Its applications are now numerous ranging in environmental sensing, process control, imaging, etc and continue to grow with new developments.

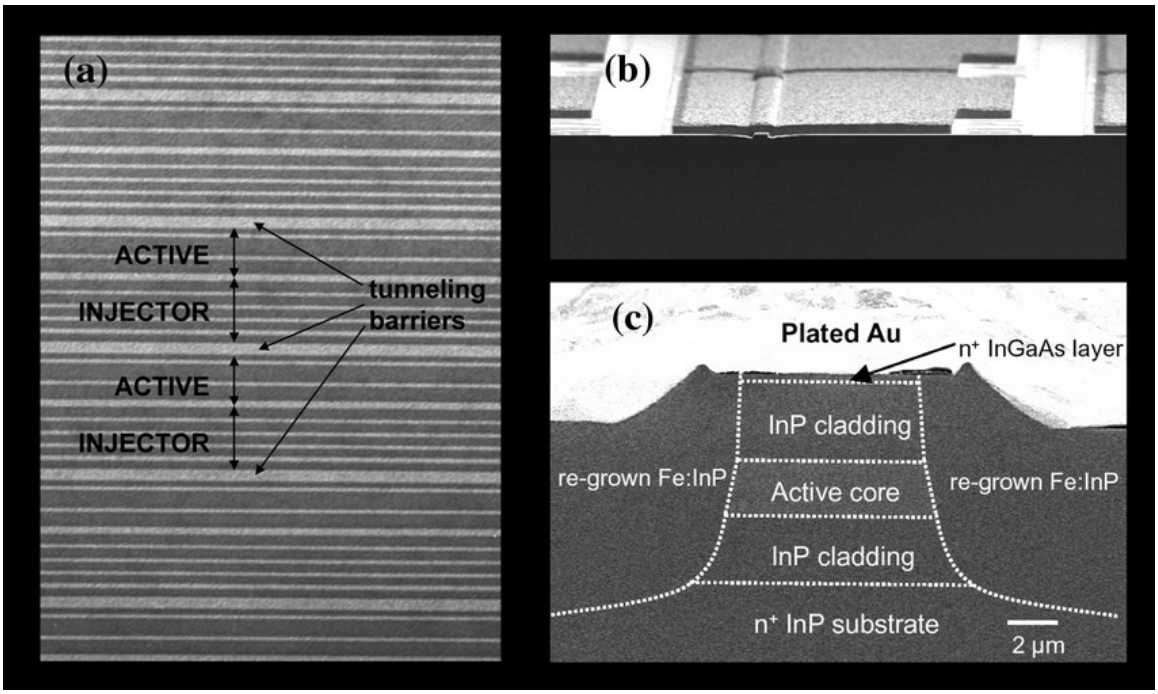

Figure 1- 4. (a) TEM picture of the active region in a 3-quantum well QCL. (b) SEM image of the finished device. (c) Close-up of the laser facet showing the buried heterostructure design. Mid-wave QCLs can have 20 to 30 periods, while THz QCLs can have even more to compensate for loss of gain from the diagonal character of the laser levels. [23]

The QCL is comprised of a superlattice of many periods, each consisting of both an injector and active region. They consist of alternating III-V materials precisely grown using MBE or other various methods. Refer to Figure 1-4a for an image of the grown layers of a high performance

QCL, grown with MOVPE [23]. Subsequent to growth, the device is typically processed into a buried heterostructure design, where the waveguide is etched and overgrowth of the cladding material (typically InP) is performed to help with both optical confinement and heat management, see Figures 4b and c. The design of the optical cavity of the QCL is very dependent on its intended use, see Figure 1-5. At its most basic, the QCL is cleaved at the desired ridge-length and the two remaining facets provide some reflection creating a fabry-perot cavity. These facets can be covered with high reflection (HR) coating, anti-reflection (AR) coating or a tunable reflectivity coating in order to provide more feedback and operate the laser at its highest efficiency. If designing a single-mode QCL often distributed feedback is used and external cavities with gratings are put in place to give better control of the optical cavity modes.

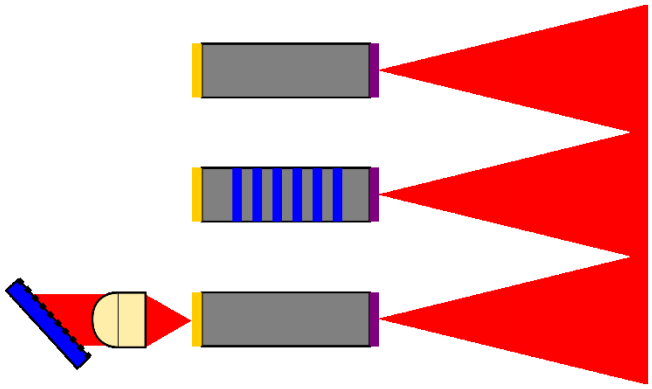

Figure 1- 5. QCL in a Fabry-Perot cavity (top), with a distributed bragg reflector (middle), external cavity QCL with grating to the left of the cavity (bottom). AR coating is in purple, HR in gold, and blue represents wavelength selective elements.

Each period of the QCL consist of four levels as shown in Figure 6a, where the last level in one period acts as the first level of the next. The very simplified band structure of a typical QCL is shown in Figure 1-6b, where each period is comprised of an active region and a

relaxation/injection region. The latter is typically comprised of multiple quantum wells in order to spread out the carrier distribution and prevent backfilling. Electrons are injected into level 2 at a rate of J/e, where J is the current density, and tunnel through the injection barrier at an engineered scattering time τ_{tun}. The electrons then either radiatively relax to level 1 (shown as $h\nu$ in figure 6b) or nonradiatively scatter to the first level at a rate of, τ_{21}^{-1}, or scatter through other parasitic pathways at a rate of τ_{para}^{-1} with the total lifetime of the level being $\tau_2^{-1} = \tau_{21}^{-1} + \tau_{20}^{-1}$. The depopulation rate of the lower laser level, τ_1^{-1}, is reduced by tuning to the LO phonon resonance, the emission of which is shown in Figure 1-6b. Population inversion, Δn, is maintained by the injector barrier, which acts to confine the electrons on level 3/0. The thickness and roughness of the injector barrier enables control of the scatter rates and helps to prevent parasitic tunneling into the next period.

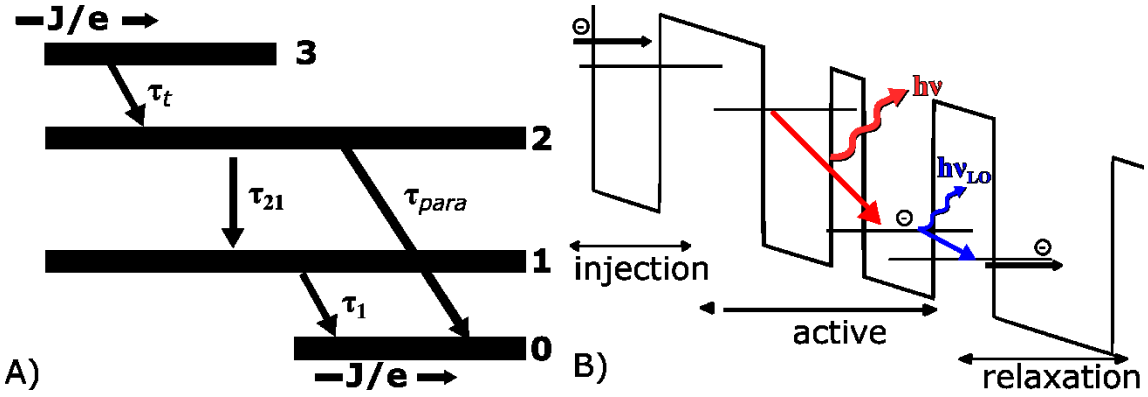

Figure 1- 6. A) Diagram of an electrically injected four-level laser and its scattering rates. B) Simplified band structure and regions of the QCL.

A simple solution of the rate equation for the laser levels diagramed in Figure 1-6a can be used to calculate, for sub threshold operation, the steady state solution revealing the condition for population inversion. If we consider the rate equations for the laser shown in Fig 5a, making the

approximation that electrons are directly injected to level 2, at a rate of J/e, and setting spontaneous and stimulated emission to zero, the rate equation for level 2 and 1 becomes

$$\begin{aligned} dN_2/dt &= J/e - N_2/\tau_2 \\ dN_1/dt &= N_2/\tau_{21} - N_1/\tau_1 \end{aligned} \tag{0.10}$$

where $\tau_2^{-1} = \tau_{21}^{-1} + \tau_{para}^{-1}$ is the total lifetime of level 2, N_n is the population of level n, and the other lifetimes are indicated in Fig 5a. Now at steady state we can calculate the population inversion Δn

$$\Delta N = \frac{J}{e}\tau_2\left(1 - \frac{\tau_1}{\tau_{21}}\right). \tag{0.11}$$

It is readily apparent that to obtain a large population inversion, and therefore gain ($\gamma = \sigma\Delta N$), the QCL must be designed such that $\tau_{21} \gg$ and the lifetime of the upper level (τ_2) is as long as possible. In order to achieve a fast depopulation rate, level 0/3 is separated from the lower lasing level (~36 meV) , on the order of the resonant energy of LO phonons for many III-V materials, greatly increasing electron-phonon scattering and minimizing τ_1. Parasitic relaxation is suppressed via the large momentum-exchange necessary for electron phonon scattering and much work has been performed to control scattering rates to achieve high-performance devices.

Typically electrons are recycled through many periods, thus one electron can excite many photons. The QCL is comprised of many periods which can be grown identically or not, as a result the gain bandwidth experiences much inhomogeneous broadening which can be engineered for a very broad gain and multimode operation. This is useful for broadband

spectroscopy and is incorporated in QCLs designed for FC spectroscopy. Calculating the gain of the laser is a valuable exercise and will be useful for understanding later analysis in the paper. In its most general form the gain coefficient can be expressed as

$$\gamma(\nu) = \frac{\gamma_0(\nu)}{1 + I / I_s(\nu)} \tag{0.12}$$

Where $\gamma_0(\nu) = \sigma(\nu)\Delta N$ is the small signal gain and I_s is the saturation intensity, both of which are derived for a particular laser. The full quantum derivation of these will be reserved for later, however using Einstein's coefficients and a semi classical derivation we can say that the absorption cross-section $\sigma(\nu) = A_{21}\frac{\lambda^2}{8\pi n^2} g(\nu)$, where n is the index, $g(\nu)$ is the linewidth of the gain including both homogeneously broadened Lorentzian distribution as well as an inhomogeneously broadened distribution. A_{21} is Einstein's first coefficient and is the rate of spontaneous radiative emission. Inhomogeneous broadening in the QCL is a very important factor in frequency comb formation as an inhomogeneously broadened gain material will have multiple resonant groups of "atoms" each with their own reservoir and threshold to pull from. As radiation in the cavity increases due to feedback from the mirrors, see Figure 1-5, multimode lasing is sure to occur.

As seen in equation(0.12), as the intensity circulating the cavity grows the gain coefficient is saturated. If the laser is at an intensity equal to the saturation intensity the steady state peak amplitude of the gain is halved. This plays an important role in the laser dynamics and must be considered, $I_s = \frac{h\nu}{g(\nu)\sigma(\nu)\tau_2}$. The saturation of levels in an inhomogeneous

system can be somewhat complex depending on how closely the systems are coupled. However if the groups are not closely coupled, the stimulated emission can saturate one group preferentially resulting in a non-uniform dip in the gain profile, known as a spectral hole. These non-uniform saturation dips act as independent reservoirs for the aligning mode in the cavity. Similarly, if we consider the physical shape of transverse mode emission profiles we realize that some modes will be greater confined to the center of the waveguide as others will be confined towards the edges, resulting in a spatially uneven saturation of the gain, or in other words a spatial hole is burned.

Optical Frequency Combs

Optical frequency combs consist of phase coherent, equidistant laser lines distributed in frequency, see Fig 1-7a. Originally developed as a tool for atomic clocks, FCs have revolutionized the accuracy at which we are able to measure time and space. Clocks based on optical transitions in atoms improve time and frequency resolution due to the high transition frequencies involved. FCs offer a link between the ultra-high frequency of the visible spectrum and the more accessible microwave frequencies through heterodyning, thus enabling measurement at realistically achievable rates. Before FCs, measuring optical frequency was performed via mathematical conversion of a measured wavelength, resulting in relatively poor accuracy. To improve accuracy and measure frequency directly, frequency chains were developed to connect a frequency reference to the optical domain via a series of phase-locked oscillators [24]. These systems were extremely complicated and were comprised of many parts taking up a large footprint. In early 2000s the demonstration of the FC made the previous

method obsolete by replacing the complicated, large set up with a single mode-locked laser that generates a broad spectral output of narrow coherent lines [25].

Individual lines in the frequency comb maintain phase relations producing a stable, periodic waveform in time. Typically this periodic waveform consists of pulses described as

$$E(t) = a(t)e^{j\omega_c t} + c.c. \tag{0.13}$$

With *c.c.* being the complex conjugate. Now if the envelope function, $a(t)$, is a simple gaussian pulse the frequency domain representation is yet another gaussian function, $A(\omega)$ with a span inversely proportional to the pulse duration. However, more generally if (0.13) is periodic it can be described by its Fourier series of optical modes, ω_N,

$$E(t) = a(t)e^{j\omega_c t} = \sum_N A_N e^{jN\omega_N t}, \tag{0.14}$$

where, ω_c is the carrier frequency. Upon close inspection it is obvious that the carrier frequency will most likely not be an exact multiple of the mode spacing, ω_{ax}, and thus the mode frequencies must be shifted by an offset frequency.

$$\omega_N = N\omega_{ax} + \omega_{off} \tag{0.15}$$

Here N is an integer that is typically very large as it connects the microwave domain (ω_{ax}) to the optical domain ω_N, where measurement of the offset frequency is critical for retrieving the absolute frequency and will be discussed later. As a simple exercise to understand the development of combs from a pulse train let us consider two pulses, i.e.

$$E(t) = \left(a(t - \tau_{rt}/2) + a(t + \tau_{rt}/2)\right) e^{j\omega_c t} + c.c.. \qquad (0.16)$$

It is fairly easy to calculate the Fourier transform of (0.16) considering frequency to be real and the pulse separation to be larger than the pulse duration.

$$E(\omega) = A(\omega - \omega_c)\cos(\frac{\tau_{rt}}{2}\omega) + c.c. \qquad (0.17)$$

Which is essentially the spectrum of the original pulse modulated in frequency with a period equal to the inverse of the round trip time. We therefore can see that as the coherent pulses become an infinite train, the spectrum modulation narrows into a comb-like signature with axial spacing equal to the free spectral range (FSR) of the laser, $\omega_{ax} = 1/\tau_{rt}$ and bandwidth inversely proportional to the pulse width. Similarly, if we consider a set of longitudinal modes, the Fourier transform of which is a set of delta functions as seen in Figure 1-7a,

$$E(t) = \sum_{n=(N-1)/2}^{(N+1)/2} A_n \exp\left[-j(\omega_c + n\omega_{ax}) + j\varphi_n(t)\right], \qquad (0.18)$$

the importance of phase coherence is revealed. If we establish both the mode amplitudes and phases to be constant, (0.18) can be reduced to

$$E(t) = Ae^{j(\omega_c t + \varphi(t))} \sum_{n=(N-1)/2}^{(N+1)/2} \mathrm{e}^{jn\omega_{ax}t} = Ae^{j(\omega_c t + \varphi(t))} \frac{1 - e^{jN\omega_{ax}t}}{1 - e^{j\omega_{ax}t}}. \qquad (0.19)$$

Calculating the power spectrum we arrive to a series of pulses as shown in Figure 1-7b,

$$S(t) = A^2 \frac{\sin^2(N\omega_{ax}t/2)}{\sin^2(\omega_{ax}t/2)} = 2A^2 \frac{\sin^2(N\omega_{ax}t/2)}{1 - \cos(\omega_{ax}t)}. \qquad (0.20)$$

Careful analysis of equation (0.20) reveals an infinite pulse train with a period equal to τ_{rt} and the width proportional to the number of modes, N, illustrating the need for a broad gain bandwidth.

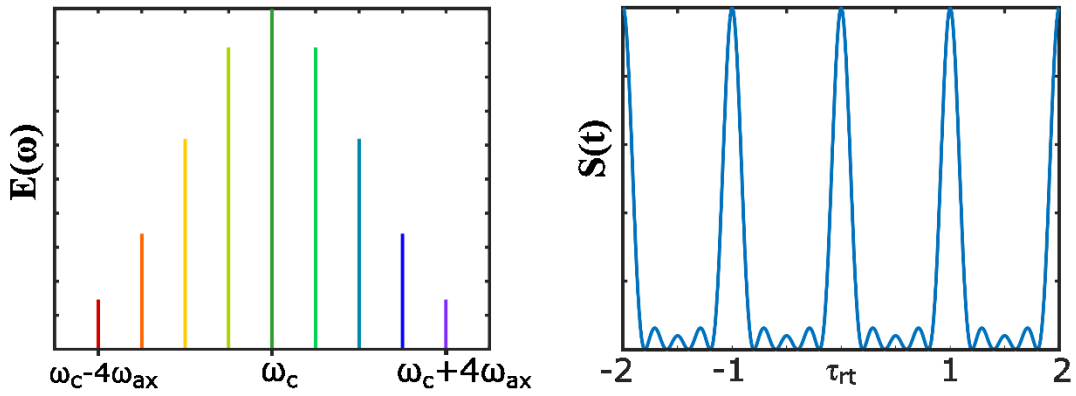

Figure 1- 7. A) Plot of a frequency comb in the spectral domain centered at ω_c with a separation of comb lines equal to the FSR, ω_{ax}. B) Plot of equation (0.20), pulse maximum occurs when $\cos(\omega_{ax}t)=1$.

Frequency combs can be generated by a variety of methods, such as by mode-locked lasers, by microresonators, by non-linear fibers, etc. The first octave spanning mode-locked lasers where Ti:sapphire lasers and are still widely used to access the visible spectrum. Often mode-locked fiber lasers are also used, however they typically have a lower inherent spectral bandwidth. See Figure 1-8 below for a FC generated from an Kerr-lens mode-locked, self-referenced TI:sapphire laser. This particular laser achieved a larger mode spacing of 10GHz such that the modes can be spectrally resolved [26]. The laser consists of ~1200 modes with at least 0.5 mW per individual mode. After broadening by a HLNF, the FC covers the visible spectrum and goes well into the near infrared (NIR) as shown in Figure 1-8c. The frequency comb is referenced with a non-linear f-2f interferometer allowing for measurement of absolute frequency. Lastly, in Figure 1-8b the

FC is passed through a grating and individual modes can be spatially resolved under magnification.

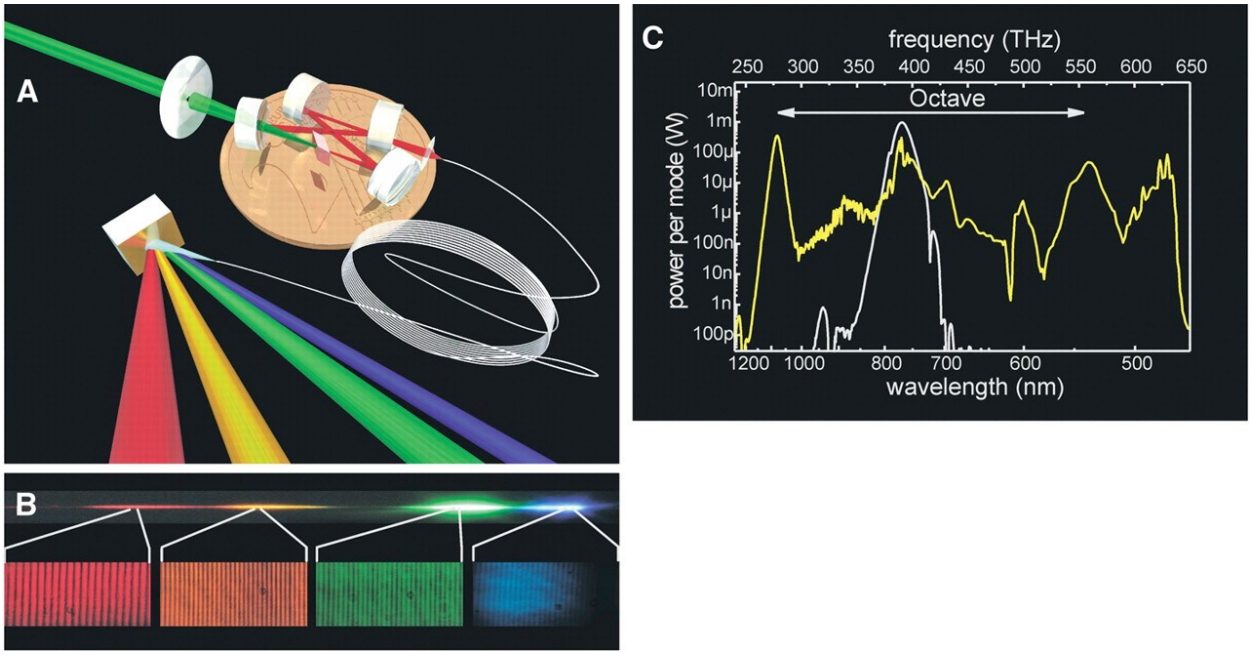

Figure 1- 8. (A) Illustration of the Ti:Sapphire laser cavity with a coin for size reference. The HNLF and grating dispersing the FC are also shown. (B) A Real color image of the dispersed FC and the magnified view of individually resolved modes. (C) Spectral measurements of the laser output before (gray line) and after (yellow line) broadening by the fiber [26].

Microresonators with very high Q factors can be pumped at a very high intensity, triggering degenerate four-wave mixing which can cascade into a frequency comb, these are often reffered to as Kerr microcombs. High Q factors and reduced mode volume increases the light-matter interaction and thus strengthens the third order nonlinear effect. With proper dispersion compensation and spectral broadening these systems can generate a supercontinuum spectrum from a single mode pump laser. In fact, with proper balance of gain and loss, as well as nonlinearity and dispersion, the system can achieve a mode-locked state with pulses circulating the resonator, under a hyperbolic secant distribution these pulses are

called solitons and maintain their shape while propagating at a constant velocity. Realization of this technique offers chip-scale FC spectrometers where CW light can be pumped into a microresonator which generates a FC that is further broadened and self-referenced on the same platform. See Figure 1-9 below for a cartoon of the process and a collection of so called "whispering gallery mode" WGM resonators, named after their macro-counterpart the whispering gallery in St. Paul's Cathedral.

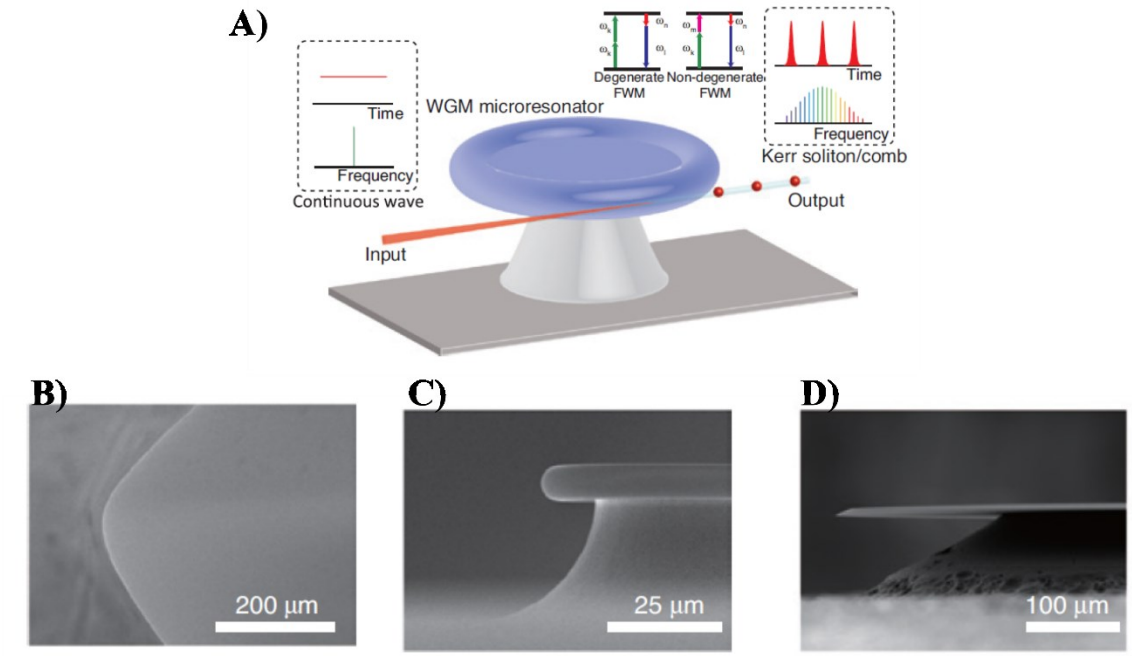

Figure 1- 9. Diagram of an optical frequency comb generated with a Kerr microresonator and a tapered fiber coupler. Scanning Electron Micrograph (SEM) images of microresonators. B) MgF_2 crystalline resonator, C) Silica microtoroid resonator, and D) a Silica microdisk resonator [27].

In order to achieve phase locking in an optical system, the proper condition for a stable solution must be provided. Typically there are two different categories of locking methods, active and passive. An active mode locking scheme involves modulation of the cavity loss (or phase) at a frequency commensurate with the cavity round-trip time. A stable solution occurs for a pulse

whose maximum occurs when the loss is minimum, this solution can fully saturate the gain as opposed to other waveforms which will experience a higher loss and will thus die out. Pulse widths for active modulation is typically larger than that of passive modulation, and can be calculated with the Kuizenga-Siegman theory. This is basically just a balance between pulse shortening as caused by the modulator and pulse broadening as caused by the gain medium. Passive mode locking is a much more powerful method resulting in shorter pulses and is typically achieved using a saturable absorber. A saturable absorber is a material that has a low saturation of absorption meaning that it becomes more transparent with light intensity, obviously the recovery time of this absorbing material is of importance for pulse width and round trip time. In this way no active modulation is needed and the saturable absorber naturally modulates loss, providing the conditions for a stable, ultra-short pulse on the scale of femtoseconds [26].

Non-linear properties of materials are also of utmost importance in the consideration of FC generation. Certain crystals (typically artificial) can exhibit non-linear properties in the presence of radiation. In conventional optics the polarization induced by the light depends linearly on the electric field

$$P(t) = \chi^{(1)} E(t), \tag{0.21}$$

Where $\chi^{(1)}$ is known as the linear susceptibility. In nonlinear optics, the optical response is represented in a power series as

$$P(t) = \chi^{(1)} E(t) + \chi^{(2)} E^2(t) + \chi^{(3)} E^3(t) + \cdots \tag{0.22}$$

Where $\chi^{(2)}$ and $\chi^{(3)}$ are the second and third-order nonlinear susceptibilities. The resulting processes that occur as a result of these nonlinear susceptibilities are conveniently and distinctly organized by these second or third order properties. Typical processes categorized as second-order nonlinearities include, second-harmonic generation (SHG), sum or difference frequency generation (SFG). Third order properties result in the Kerr effect (an intensity dependent refractive index), two photon absorption, third harmonic generation, and four-wave mixing. This can result in many frequency components (modes) in the cavity however typically many of these modes are very low-power, and often no more than one of the frequency components will be present. The reason for this is the requirement of the phase-matching condition which must be satisfied for the nonlinear polarization to noticeably diminish the input frequency at all. The phase matching condition for SFG as an example is

$$\Delta k = k_1 + k_2 - k_3 , \tag{0.23}$$

and the intensity at ω_3 is highest when $\Delta k = 0$, it drops of quickly when this is not satisfied. This condition is often difficult to achieve because the refractive index of materials are typically normal in dispersion, i.e. the refractive index is an increasing function of frequency. As a result the condition matching equation (0.23) for SHG, as an example due to the simplicity, cannot be met

$$2n_1\omega_1 = n_3\omega_3 , \tag{0.24}$$

for an index that increases with frequency as $n(\omega_1) \neq n(2\omega_1)$. This is often overcome with designing for anomalous dispersion or using birefringence of a material to properly phase match.

Frequency Combs generated from QCLs as well as FCs broadened by nonlinear resonators can be locked with four-wave mixing, a third order nonlinearity as mentioned earlier. This occurs when two frequencies are propagating in the cavity, the modulation of the refractive index at the difference frequency essentially creates two sidebands at $\nu_3 = \nu_1 - (\nu_2 - \nu_1)$ and $\nu_4 = \nu_2 + (\nu_2 - \nu_1)$. This can effectively proliferate over a broad spectrum and maintain coherence between the teeth of the FC, so long as the chromatic dispersion is suitable. Achieving phase matching in this scenario is typically achieved by designing the optical system to introduce anomalous dispersion inside the cavity, acting to counterbalance the typical normal dispersion in the hope to obtain a near zero group velocity dispersion. This has been the method used for designing QCLs to emit FCs however recent research [28] has suggested that residual dispersion is a key to a stable laser. Chromatic dispersion can be described as a series approximation

$$k(\omega) = k_0 + \frac{\partial k}{\partial \omega}(\omega - \omega_0) + \frac{1}{2}\frac{\partial^2 k}{\partial \omega}(\omega - \omega_0)^2 + \cdots \qquad \cdots(0.25)$$

Where the zero order term is a phase-shift, the first order term $\partial k / \partial \omega$ is the group delay or the reciprocal inverse of the group velocity, and the second order term is the inverse of the group velocity dispersion. The pulse moves at the group velocity and thus determines the axial spacing or free spectra range (FSR) of the frequency comb, $\Delta\omega_{ax} = 1/\tau_{rt} = v_g / 2L$. Stabilization

of the offset frequency, or even tuning of the carrier frequency can be achieved with loop feedback and control of dispersion in the system. Too much GVD (β_2) will distort the pulse (typically broadening the pulse and adding a frequency chirp) eventually ruin the phase matching condition necessary for four-wave mixing and result in either significant narrowing of the comb or incoherence of the modes. It can be shown that not only GVD but also higher order dispersion influences the axial frequency between individual comb teeth such that

$$\omega_m = \omega_0 + mD_1 + \frac{1}{2}m^2 D_2 + \cdots \qquad (0.26)$$

Where *m* represents the mode index and D_n reprensts the n^{th} order dispersion parameter or change of group delay per unit length as a function of wavelength $D = -\frac{2\pi c}{\lambda^2}\beta_2$. Thus it is typically necessary to compensate for GVD, which is dependent on the driving conditions of the system, the environment and can be introduced by many aspects such as the waveguide geometry, material parameters, gain of the laser, and other optical components. There are many methods to compensating for GVD, most involving introduction of anomalous dispersion into the cavity with Gires-Tournois interferometers (GTIs) [29], special dispersive fibers [30], waveguide coupling[31] , and even plasmonics [32]. Many of these methods have been implemented in the QCL, however dispersion compensation is especially challenging as the shape of the GVD depends strongly on the shape of the gain curve, which itself is determined by the gain saturation and the operational specifications.

Spectroscopy with Frequency Combs

FCs provide a link between optical and microwave frequencies, allowing for detection of frequencies previously inaccessible by even our fastest detectors. We can therefore have access to faster frequencies by heterodyning, or essentially combining two high frequencies to obtain a low frequency determined by their difference. As illustrated by calculating the power of two fields and passing through a low frequency filter,

$$S(t) = \left[A_1 \sin(\omega_1 t) + A_2 \sin(\omega_2 t)\right]^2 = A_1 A_2 \cos(\omega_1 t - \omega_2 t) \qquad (0.27)$$

the frequency $\omega_1 - \omega_2 = \omega_{ax}$, or so called beat signal, can be measured. In some applications it is necessary to obtain the absolute frequency and thus know both the axial frequency, f_{ax}, and the offset frequency, f_{off}, of equation (0.15) . When referencing a full octave spanning comb it is possible to us a technique called self referencing [25], this uses harmonics of the comb light to measure the offset frequency however places demands on the spectral bandwidth of the FC. In f-2f referencing the red wing of the comb is frequency doubled to $2(\omega_{off} + n\omega_{ax})$ and then beat with the blue side of the comb at $\omega_{off} + 2n\omega_{ax}$ resulting in a beatnote that is simply equal to the offset frequency. While this works well for many lasers, the QCL does not emit a broad enough spectrum and even then SHG is difficult due to the lack of peak powers in a pulse. Thus another technique must be implemented.

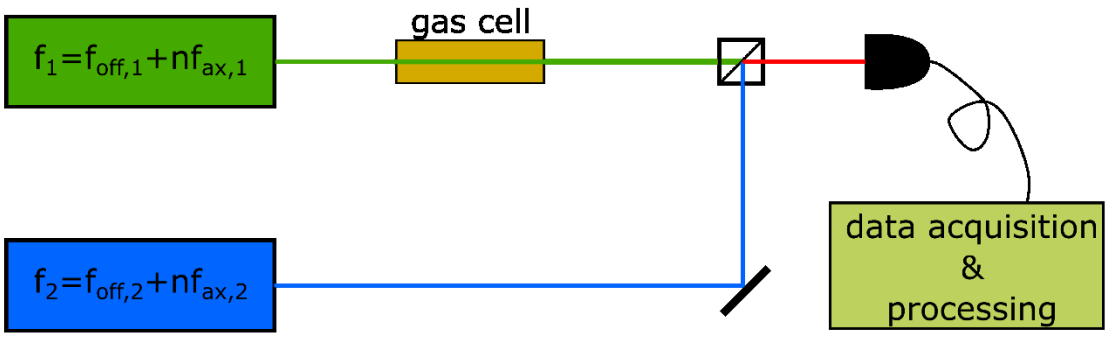

Figure 1- 10. Diagram of dual comb spectroscopy set up where two frequency combs are utilized. The path of one comb samples the absorption of a gas cell and the beatnotes separated by δ are recorded by a photodetector.

Dual comb spectroscopy is advantageous in that it is relatively easy to keep the beatnote frequency within range of the detector and doesn't require a full octave for referencing. This method was proposed in 2002 [33] and is the combination of two frequency combs with slightly different repetition frequencies $f_{ax,1} = f_{ax,2} + \delta$. The experimental set up is shown in Figure 1-10, it consists of the two FC sources in which at least one comb samples the gas under study. The path of the two FCs are then combined and the summation is recorded on a detector, typically a common photo diode. The signal of the detector is referred to as the interferogram and its fourier transform contains the absorption information of the gas sample. If we are to only consider the beat signals of the combined combs with the same order *n*, the beatnote is described as

$$f_{n,1} - f_{n,2} = \left(f_{0,1} - f_{0,2}\right) + n\delta, \qquad (0.28)$$

and the resulting down converted spectrum is shown in Figure 1-11 . Where the amplitudes of the lines can be used to measure the absorption spectra of the investigated sample. The optical

spectrum has thus been accessed at a much lower frequency with a down conversion coefficient or scaling factor given by

$$a = \frac{\delta}{f_{ax}} \tag{0.29}$$

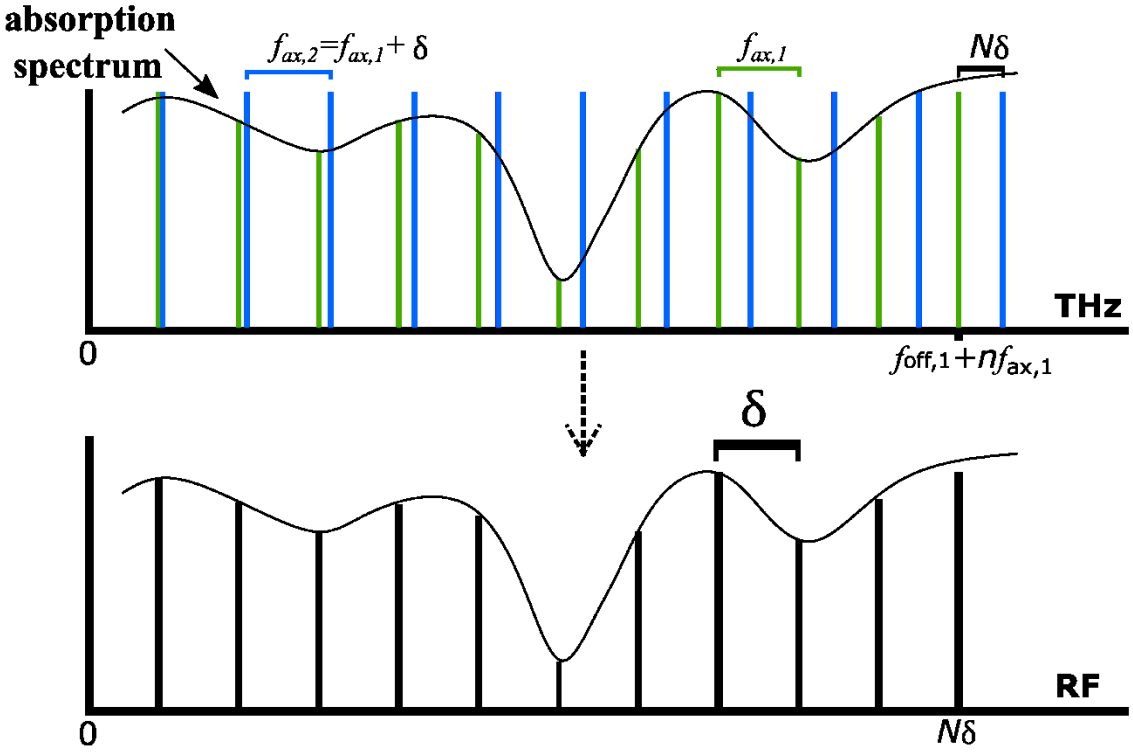

Figure 1- 11. Diagram of the down conversion from beating two slightly different combs together in a dual comb spectroscopy measurement.

Quantum Cascade Laser Frequency Combs

Initially developed in the visible spectrum, there has been a strong push to extend spectral coverage to smaller wavelengths as well as up to mid and far IR regime, and even THz. Unfortunately, FC access to the long-wave and THz regimes have been hindered by lack of viable sources. Typically, generation of FCs in the mid-to-far IR are a result of frequency

conversion which is inherently inefficient leading to small powers in the range of 1nW/mode [34]. FCs are typically generated using mode-locked lasers, micro-resonators and optical downconverters greatly adding to the complexity, power consumption, and size of device. To avoid this complexity a logical choice would be to turn to electrically pumped lasers, which for the LWIR and THz regions implies QCL.

While most FCs are generated from pulses in the time domain, this is theoretically not the only waveform that can result from a frequency comb. Put plainly, frequency combs can result from not only periodic amplitude modulation but also frequency modulation as we can see from

$$S_m(t) = A\cos(\omega t + \beta \sin \omega_m t) = A\sum_{-\infty}^{\infty} j_n(\beta)\cos\left[\left(\omega + n\omega_m\right)t\right]. \tag{0.30}$$

Additionally, the phases of the modes can hold a relation to each other rather than being ubiquitously equal. To calculate the bandwidth of the FC we turn to Carson's rule

$$BW = 2f_m(\beta + 1). \tag{0.31}$$

As mentioned previously, emission in the IR and THz is limited by material available. While spectroscopy in this region is highly sought after, typical methods are fairly limited. Methods requiring a broadband source (e.g. FTIR) rely on moving parts and are very slow. Wavelength tuning of a QCL can be highly accurate however very limited in range. Thus a FC at longer wavelengths is highly desired. The QCL is an obvious candidate however passive mode locking is hard to achieve in QCLs because of their inherently short gain recovery time, as mentioned earlier. The QCL therefore acts like a fast saturable gain or "reverse saturable absorber", and, as

the name implies, will favor a constant intensity rather than a pulse as favored by a saturable absorber. This gives insight into the mode-locking mechanism of the laser as a perfectly frequency modulated laser would be emit a constant intensity. Despite this difficulty, and rather fortuitously, free-running QCLs have been shown to emit stable frequency combs without the introduction of any active or passive elements. Unlike typical frequency combs however, the temporal waveform of the QCL was not a periodic train of short pulses, but rather a semi-continuous waveform. While the temporal waveform does possess some residual AM, the cause of which is discussed, it is mainly dominated by strong frequency modulation (FM).

The first demonstration of a QCL generated FC was in 2012 [1]. This was very exciting work as it opened up improved methods for spectroscopic access to the molecular fingerprint region. The QCL operates under direct electrical pumping and requires no extra elements, other than dispersion compensation, to generate a frequency comb. A frequency comb was proven, as opposed to separate or incoherent multimode emission, due to the line-to-line frequency noise being correlated and a resulting beatnote linewidth that was very narrow. As a broad spectrum is highly desirable no matter the locking mechanism, *broadband* QCLs [35] are used for FC generation. These QCLs achieve a broad gain spectra by designing dissimilar active regions in the cascaded structure such that each emits at a different wavelength. As mentioned earlier, four wave mixing (FWM) plays a crucial role in the generation of frequency combs from QCLs. As with any two level system, the active region of the QCL exhibits strong optical nonlinearities. Serendipitously, the very fast upper-state lifetime of the QCL, while being detrimental to conventional mode-locking, results in a very broadband FWM process [36]. Strong FWM in a QCL was reported in [37] and the results are shown in Figure 1-12 below. The

experimental setup consisted of a single mode QCL and a tunable source (based on difference frequency generation) that were passed through a QCL amplifier into a spectrometer, measuring the generation of two new frequencies. This important work concluded that a large, resonant $\chi^{(3)}$ response arises from the active medium itself and the bandwidth of the FWM process is much wider than typical due to the gain recovery time.

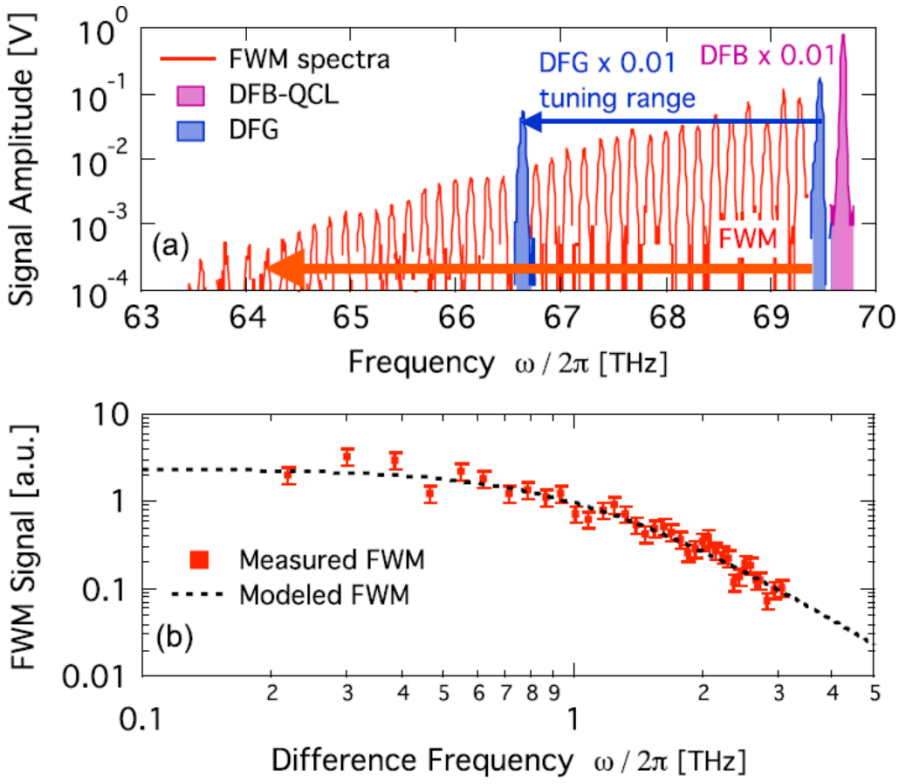

Figure 1- 12. Results from [37]. A) Measured output spectrum of the FWM from the tuning of the DFG source between 69.5 and 66.7 THz. B) Intensity of the FWM signal versus the difference frequency between DFB-QCL and DFG up to a maximum detuning of 3.06 THz.

As detailed earlier, separating dispersion and gain is difficult, however the Maxwell-Bloch model is uniquely qualified to handle both of these contributions. The carrier dynamics of the active region can be represented by optical Bloch equations for a density matrix describing the

laser transition of the two-level system, these equations will be addressed in more detail later on in this dissertation. The Maxwell equations are then used to describe the motion of the electromagnetic wave in the cavity. Solving this system in the frequency domain perturbatively to the third order, using the modes of the laser cavity as a basis, theoretically confirmed FM operation in QCLs generating FCs [5]. Therefore a rationalization was developed for the free-running generation of FCs in QCLs, rather than producing a frequency comb with equal phase relationships, as in the presence of a time-domain pulse, a usable frequency comb simply requires a stable phase relationship between comb lines. One such stable phase relationship results in a constant intensity and a periodic modulation of instant frequency, or FM lasing [38]. As the fast saturable gain of the laser favors constant intensity, yet must go multimode because of various hole burning mechanisms developed from the Fabry-Perot cavity and inhomogeneous broadening, a frequency modulated laser is a comprehensible explanation. Results of the frequency domain model [5] predicted what we refer to as a “pseudorandom” FM signal, in that it is periodic with the roundtrip time yet strongly irregular on shorter time scale.

At the time that these results were published and the phenomenological explanation was developed, definitive, experimental access to the instantaneous power and phase relationship of the FC was not possible. Most phase measurement methods of this sort involved the generation of harmonic frequency via nonlinear conversion and with the lack of a pulse, the high intensity required for these measurements was not available. Not until David Burghoff of MIT develop a method for measuring the phase difference between comb teeth dubbed shifted wave interferometric fourier transform (SWIFT) spectroscopy [39]. During the time it took to

develop this method, broadband QCLs emitting FCs where being experimentally improved with the aim to produce a standardized QCL that emits a reproducible and stable frequency comb. With the development of SWIFTS and the improvement of the QCLs it became apparent that the instant frequency predicted by the model [5] was actually quite different and consisted of a frequency ramp or a quadratic phase relationship between the mode lines [40]. While this experimental evidence contradicts some work of this thesis, the underlying ansatz of this dissertation still holds. There are an infinite number of operational modes of the QCL possible, the dynamics of these modes are defined by many aspects of the laser, which will settle in the most efficient regime given the constraining factors such as group velocity dispersion of the laser (which was not included in [5]), gain saturation, and the design of the cavity (as it alters spatial hole burning). These various factors can push the laser to operate in very different regimes, however all are FM including some amount of AM and all have an instant frequency with an amplitude A_{fm} that is commensurate with the gain bandwidth of the laser. The ramp-FM QCLs [40] are very stable and reproducible devices, the FM signal of which has recently been explained as a cause of residual dispersion in [28], however other designs and operational modes should be considered as well. It is the hope of the author that this work will help to further improve understanding of the various factors involved in the balancing act of QCL operational regimes. A deeper understanding of the underlying mechanisms at play in the laser, rather than simply running an overly complicated model and presenting the results, is the true goal of this work.

Chapter 2: The QCL time-domain mode

In the following section the time-domain model on which much of this work is based on is developed. To provide a complementary model to the frequency domain model described in [5], but also further introduced later in this chapter, as well as to more deeply investigate the various catalysts that define the laser's operational dynamics such as hole burning and gain recovery we devise a model in the time-domain using optical Bloch equations (OBE). Before introducing the model, the rationalization behind this work must be discussed. It has been well known [41] that a laser naturally will operate such that the internal field will experience the least loss under many circumstances. The operational mode with the least loss will also have the lowest threshold and thus will be the first dynamical regime to emerge. This reasoning is known as the maximum emission principle (MEP) and has been illustrated with many mode-locked lasers. True to the MEP, the phases of all the modes in the cavity will adjust to produce a field experiencing the least loss, which with a saturable absorber present will be a pulse that simply arises from amplitude noise. This also implies that the linewidth of all the modes will be minimized as they are inversely proportional to the total output power of the laser [42]. While it is known that the MEP is not necessarily ubiquitous, under an ultra-fast relaxation time this principle is further confirmed by Hamilton's principle [43], which is very applicable to the QCL. This method is used by many theoreticians to predict the behavior of a variety of optical systems [44, 45], furthermore in the writing of this dissertation, this technique has been further developed for QCL FCs [46], confirming that the rationale presented in this work is valid for FCs in which the FSR is constrained by the round trip time τ_{rt}, i.e. no modes are skipped. It is the

goal of this work to develop a deeper understanding of the inner workings of the QCL FC dynamics using a simplified model rather than developing a complicated model that produces results for reasons that can only be speculated on.

Introduction to Susceptibility, classical model

Before delving into the development of the model on which this work is based, it will be useful to introduce the reader to a semi-classical derivation of the interaction between light and a two-level system. This is semi-classical in that the atom or material is quantized where the field is not. This method is applicable when dealing with a great number of photons, such as in a laser, however cannot describe certain aspects of the atom-photon interaction such as spontaneous emission.

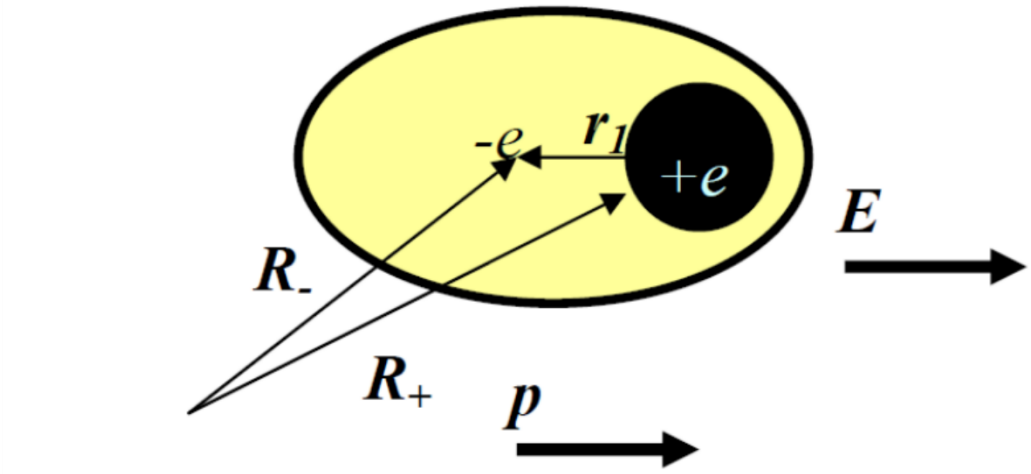

Figure 2- 1. Cartoon of a dipole under an electric field.

Interaction between light and an atom induces a dipole, this dipole depends on the material type however here we will reference polarization in a dielectric where there are no

free charges. However, there are bound charges and these are the source of material polarization. Considering the dipole in Figure 2-1., we can introduce a dipole moment

$$p = eR_{+} - eR_{-} = -er \text{ , } \quad (2.1)$$

where the material polarization is simply the collective dipole moment per unit volume

$$P = V^{-1} \int p(r) r dV \text{ . } \quad (2.2)$$

Which in reference to the field displacement is $D = \epsilon$ or introducing susceptibility,

$D = \epsilon \epsilon$ ϵ Ξ . (2.3)

Before addressing polarization at a semiclassical level it is useful to see the derivation of susceptibility at a completely classical level, where the dipole is simply modeled as two masses connected by a string and the governing equation follows a harmonic oscillator model:

$$m \frac{d^2 r}{dt^2} = -Kr - m\gamma \frac{dr}{dt} - eE \text{ , } \quad (2.4)$$

where γ is the damping in the system and $K = m\omega_0^2 r$ is the atomic resonance frequency. Now we know the field is harmonic and thus the solution of r will follow the field $r = r_0 e^{jkr - j\omega t}$ which when substituted into (2.4)

$$-m\omega^2 r = -m\omega_0^2 r + j\omega m\gamma r - eE \quad (2.5)$$

Giving a susceptibility of

$$\chi(\omega) = \frac{\omega_p}{(\omega_0^2 - \omega^2 - j\omega\gamma)} = \chi'(\omega) + j\chi''(\omega) \quad (2.6)$$

Where $\omega_p = Ne^2/\epsilon$ is the plasma frequency, the value of which is highly significant with respect to the propagation of light through the dipoles or "plasma" and is the frequency at which the *collective* dipoles oscillate. Far from resonance we see that the imaginary component of the susceptibility is approximately zero and the real component settles into a "background" dielectric constant (far from resonance)

$$\chi'(\omega) = \frac{\omega_p^2}{\omega_0 - \omega^2}. \qquad (2.7)$$

Close to resonance we have

$$\chi'(\omega) = \frac{\omega_p^2 / 2\omega_0(\omega_0 - \omega)}{(\omega_0 - \omega)^2 - \gamma^2/4}; \chi''(\omega) = \frac{\omega_p^2}{2\omega_0} \frac{\gamma/2}{(\omega_0 - \omega)^2 + \gamma^2/4} \qquad (2.8)$$

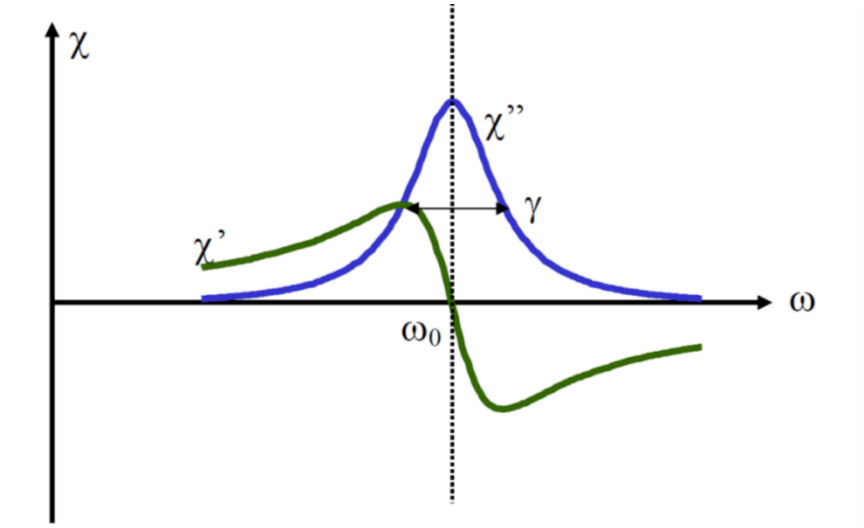

Figure 2- 2. The real and imaginary part of susceptibility close to resonance.

Thus, as shown in Figure 2-2 above, the imaginary part of the susceptibility is significant only near the resonance. The shape of the curve is a Lorentzian with its max value at resonance

$\chi''(\omega_0) = \omega_p^2 / \omega_0\gamma$ and its FWHM is exactly γ thus the dampening can be referred to as spectral broadening. Now, substituting $n^2 = \bar{n}^2 + \chi'(\omega) + j\chi''(\omega)$ into the wave equation (where $\bar{n}$ is the background index from dipoles far from resonance) results in

$$\frac{\partial^2 E}{\partial t^2} - \frac{\bar{n}^2}{c^2}\frac{\partial^2 E}{\partial t^2} = \frac{\chi'(\omega) + j\chi''(\omega)}{c^2}\frac{\partial^2 E}{\partial t^2} = \frac{1}{c^2}\frac{\partial^2 P}{\partial t^2}. \qquad (2.9)$$

Defining the electric field $E(z,t) = A(z)e^{j(\bar{k}z-\omega t)}$ and assuming a slow envelope function $\frac{\partial^2 A}{\partial z^2} << \bar{k}\frac{\partial A}{\partial z}; \bar{k} = \bar{n}\frac{\omega}{c}$ we can substitute and approximate:

$$\frac{dA}{dz} = -\frac{\omega\chi''}{2c\bar{n}}A + j\frac{\omega\chi'}{2c\bar{n}}A \qquad (2.10)$$

Splitting the field at resonance (A(z)) into the amplitude and phase $A = \bar{A}e^{j\Phi}$ and taking the derivative

$$\frac{dA}{dz} = \frac{d\bar{A}}{dz}e^{j\Phi} + j\frac{d\Phi}{dz}\bar{A}e^{j\Phi} \qquad (2.11)$$

Which when compared to equation (2.10) reveals that the real susceptibility only effect phase while the imaginary part affects the amplitude.

$$\begin{aligned}\frac{d\bar{A}}{dz} &= -\frac{\omega\chi''}{2c\bar{n}} = \frac{\alpha}{2}\bar{A} \\ \frac{d\Phi}{dz} &= \frac{\omega\chi'}{2c\bar{n}} = \frac{\alpha}{\gamma}(\omega-\omega_0)\end{aligned} \qquad (2.12)$$

Where we can then define the classical cross section absorption close to resonance

$$\sigma = \alpha / N = \frac{\pi e^2}{2c\bar{n}\epsilon} \quad \sim(\omega) \tag{2.13}$$

Where $g(\omega) = \frac{1}{\pi} \frac{\gamma/2}{(\omega_0 - \omega)^2 + \gamma^2/4}$ is the linewidth due to broadening, a Lorentzian as shown earlier in the case of homogeneous broadening. Now if we quantize the energy levels we see quite surprisingly that this Lorentz model very closely matches the quantum model, with the exception of the so called oscillator strength f_{12} and a 1/3 averaging over dimension

$$\sigma_{21} = \frac{\pi e^2}{2c\bar{n}\epsilon} \quad f \sim(\upsilon), \tag{2.14}$$

which expresses the probability of absorption or emission in transition between energy levels.

Semi-Classical Model of Susceptibility

For many scenarios it is sufficient to reduce the multitude of energy levels in a material to just two levels, this is especially applicable to the laser transition. The pumping of the laser and relaxation from the lower level can be described by a phenomenological process. The interaction of these two-levels with the electric field is described by the Bloch equations. In order to describe these two levels we resort to the bra-ket notation and define a two dimensional state space spanned by the two orthonormal, energy eigenstates $|1\rangle$ and $|2\rangle$ with corresponding energy eigenvalues of E_1 and E_2. The wave functions of these states are defined as $\psi_0(x) = \langle x|1\rangle$ and $\psi_1(x) = \langle x|2\rangle$ and the Hamiltonian of the atom (or really any quantum entity) is given by

$$H_a = E_0|1\rangle + E_1|2\rangle \tag{2.15}$$

We can therefore introduce four linearly independent linear operators, one possible choice of an operator base is

$$\begin{aligned} \mathbf{1} &= |1\rangle\langle 1| + |2\rangle\langle 2| \\ \sigma_z &= |1\rangle\langle 1| - |2\rangle\langle 2| \\ \sigma^+ &= |2\rangle\langle 1| \\ \sigma^- &= |1\rangle\langle 2| \end{aligned} \quad . \tag{2.16}$$

When applied to an arbitrary state $|\psi\rangle = c_0|1\rangle + c_1|2\rangle$, where *c* represents the probability of occupation, the purpose of these operators becomes apparent. Considering that these states are orthogonal, $\langle n \mid m\rangle = \delta_{nm}$ and independent.

$$\begin{aligned} \sigma^+|\psi\rangle &= c_1|2\rangle \\ \sigma^-|\psi\rangle &= c_2|1\rangle \\ \sigma_z|\psi\rangle &= c_2|2\rangle - c_1|1\rangle \end{aligned} \tag{2.17}$$

Thus, the σ^+ operator generates a transition from the ground state $|1\rangle$ to the excited state $|2\rangle$ and the σ^- operator vice versa. Now the σ_z operator represents the population inversion which is equal to its expectation value

$$\langle\psi|\sigma_z|\psi\rangle = |c_2|^2 - |c_1|^2 . \tag{2.18}$$

This two dimensional state space consisting of a ground and excited state basis which can be represented as two vectors, $(0,1)$ and $(1,0)$ respectively. Thus our wave equation is simply

$$|\psi\rangle = \begin{pmatrix} c_2 \\ c_1 \end{pmatrix} \tag{2.19}$$

And the operators defined in (2.17) can also be represented by the matrices

$$\sigma^{+} = \begin{pmatrix} 0 & 1 \\ 0 & 0 \end{pmatrix}$$
$$\sigma^{-} = \begin{pmatrix} 0 & 0 \\ 1 & 0 \end{pmatrix} \tag{2.20}$$
$$\sigma_z = \begin{pmatrix} 1 & 0 \\ 0 & -1 \end{pmatrix}$$

It is worthwhile to now introduce the so called density operator $\rho = |\psi\rangle\langle\psi|$, or can be represented by the 2x2 matrix

$$\rho = \begin{pmatrix} |c_2|^2 & c_2 c_1^* \\ c_2^* c_1 & |c_1|^2 \end{pmatrix} = \begin{pmatrix} \rho_{11} & \rho_{10} \\ \rho_{01} & \rho_{00} \end{pmatrix} \tag{2.21}$$

for the case of a pure state. Thus the main diagonal elements of the density matrix contain the population probabilities of the excited and ground states, which of course add to one. The off-diagonal components represent the expectation value of the positive and negative frequency value of the dipole moment, or in other words the polarization contribution. The density matrix is quite convenient when calculating the expectation value of an operator. For any arbitrary operator, **A**, we can calculate the expectation value by simply taking the trace formula

$$\langle A \rangle = Tr\{\rho A\} = \langle \psi | A | \psi \rangle \tag{2.22}$$

This becomes important when we wish to calculate the polarization of the medium. Which is simply based on the displacement, $\vec{r}$ $\vec{r}_{10}$, *e* being the unit charge of an electron. Thus, using the density matrix we can calculate the polarization of the medium quite easily

$$\langle\psi|\vec{r}|\psi\rangle = \mathrm{Tr}\{\rho\vec{r}\}. \tag{2.23}$$

To calculate this let us look more closely at the expectation value for the dipole moment, which under inversion symmetry (e.g. $\langle 2|\vec{r}|2\rangle = \langle 1|\vec{r}|1\rangle = 0$)

$$\langle\psi|\vec{r}|\psi\rangle = \rho_{11}\langle 1|\vec{r}|1\rangle + \rho_{22}\langle 2|\vec{r}|2\rangle \tag{2.24}$$

Thus we can state that

$$\langle\psi|\vec{r}|\psi\rangle = \rho_{21}\langle 1|\vec{r}|2\rangle + \rho_{12}\langle 2|\vec{r}|1\rangle, \tag{2.25}$$

where $\vec{\mu}_{12} = q\langle 1|\vec{r}|2\rangle = q\vec{r}_{12}$ is the dipole matrix element. Thus returning to equation (2.23)

$$p = \langle\psi|\vec{r}|\psi\rangle = \vec{r}_{21}\rho_{12} + \vec{r}_{12}\rho_{21}. \tag{2.26}$$

The energy of the dipole in an electric field is

$$H_{field} = -\vec{r}\cdot\vec{E}. \tag{2.27}$$

Now, to get insight to the dynamics of the two laser system we investigate the change in the density matrix with time, i.e $\frac{d}{dt}\rho$. Turning to the Schrödinger equation we can derive what is called the von Neumann equation

$$\begin{aligned}\frac{\partial}{\partial t}\rho &= \left(\frac{\partial}{\partial t}|\psi\rangle\right)\langle\psi| + |\psi\rangle\left(\frac{\partial}{\partial t}\langle\psi|\right) = \frac{1}{j\hbar}H|\psi\rangle\langle\psi| - \frac{1}{\hbar}|\psi\rangle\langle\psi|H \\ &= \frac{1}{j\hbar}[H,\rho]\end{aligned} \tag{2.28}$$

Therefore the equation of motion for the density matrix is simply the commutation of the Hamiltonian of the system and the density matrix.

Frequency Domain Model

Before introducing the time domain model on which the majority of this dissertation is based, it is useful to first introduce the frequency domain model developed by Yamac Dikmelik and Jacob Khurgin [5] as it will be referred to often in the subsequent sections. The frequency domain model was the first to confirm that QCLs have a natural state of FM operation producing phase stable FCs and used a set of perturbative solutions to the Maxwell Bloch equations. Here we briefly review this model and its main results. The derivation can be read in the supplementary of [5], however the main equation governing the temporal development of modal amplitudes A_n is

$$\frac{dA_n}{dt} = (G_n - 1)A_n - G_n \sum A_m A_k A_l^* B_{kl} C_{kl} \kappa_{klmn} \tag{2.29}$$

Where the time has been normalized to the photon lifetime, and G_n is the gain in the n^{th} mode $G_n = G_0[1 + n^2(\tau_{coh}/\tau_{rt})^2]^{-1}$, where τ_{coh} is coherence time of the ISB transition and G_0 is the unsaturated gain normalized to the threshold. The coefficients $B_{kl} = [1 + \frac{1}{2}(k^2 + l^2)(\tau_{coh}/\tau_{rt})^2]^{-1}$ and $C_{kl} = [1 - j(k-l)\tau_{21}/\tau_{rt}]^{-1}$ determine how many modes participate in FWM and the amplitude of the coherent population beating, respectively.

Where the G_n is the gain normalized to its threshold value, and the second term on the right hand side describes four wave mixing (FWM) of 4 modes whose frequencies are related by the condition $m = n - k + l$, time has been normalized to the cavity roundtrip time τ_{rt}, the

Lorentizan coefficients $B_{kl} = \left[1 + \frac{1}{2}(k^2 + l^2)(\tau_{coh} / \tau_{rt})^2 \right]^{-1}$, where τ_{coh} is the coherence time in the two level system, controls the number of modes participating in the FWM, $C_{kl} = \left[1 - j(k-l)\tau_{21} / \tau_{rt} \right]^{-1}$, where τ_{21} is the upperstate lifetime, is the coefficient describing the amplitude of the coherent population beating.

Lastly,

$$\kappa_{klmn} = l_c^{-1} \int_0^{l_c} \sin(\mathrm{k}_k\, x) \sin(\mathrm{k}_l\, x) \sin(k_m x) \sin(\mathrm{k}_n\, x) dx \qquad (2.30)$$

is the normalized intermodal overlap in space, signifying the presence of hole burning. Largest of modal overlaps is the self-saturation scenario when $\kappa_{kkkk} = 3/8$. The cross-saturation overlap of two modes is $\kappa_{kknn} = 1/4$ and non-degenerate FWM where $\kappa_{klmn} = 1/8$ supports multi-mode operation with less saturation of the gain. It is important to highlight the key difference between QCLs and other lasers, namely that for a QCLs, $\tau_{21} / \tau_{rt} << 1$ as opposed to $\tau_{21} / \tau_{rt} >> 1$, which is the case for semiconductor diode or solid state lasers. The latter two coefficients, C_{kl} and κ_{klmn}, can elucidate the behavior of the QCL. Regarding the modal overlap, one can calculate that for self saturation (n=m=l=k) the overlap is larger (3/8) than for cross-saturation (k=l,m=n) where the overlap is equal to ¼, and thus multimode operation arising from cross-saturation will have a lower threshold and be the operating regime of choice for the laser. This is simply a frequency domain interpretation of spatial hole burning. Now turning our consideration to C_{kl} we see that for most interband lasers this coefficient is very small because

$\tau_{21} \gg$, however this is not the case for QCLs and that results in strong FWM that couples the frequency and phases of the modes. Therefore significant four-wave mixing (FWM) occurs, however, unlike the diode or solid state lasers, conventional mode-locking is still extremely difficult as mentioned previously. Despite this, the QCL still manages to lock a phase relation between the individual lines in the FC.

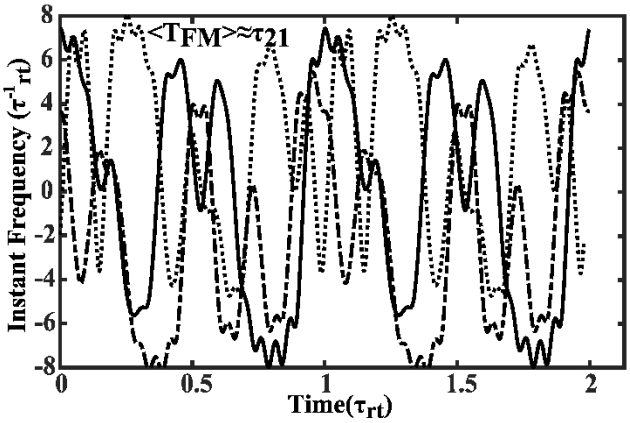

Figure 2- 3. Three results of independent runs of the FD model illustrating the pseudo-random instantaneous frequency modulation.

For a typical free running QCL, the FD model produces a nearly time independent intensity as well as a pseudo-random FM emission. Pseudo in that the FM is periodic with the round trip time, yet strongly irregular on shorter time scales, see Figure 2-3. Successive results of the FD model first appear uncorrelated, but each possess a central oscillation period, T_{fm}, commensurate with the gain recovery lifetime, τ_{21} , and an amplitude commensurate with the gain bandwidth. At the time of writing [5], the explanation of pseudo-randomness was not given, but one can argue that the random nature of the FM is indeed a preferred operating regime of a free running QCL with a well-compensated dispersion. What is meant as the

preferred operating regime is the regime which has the lowest threshold, or that in which the photons, on average, experience the highest net gain as they pass through the active region. This concept of maximum emission is not a new approach and is described thoroughly in [41]. This lowest threshold operation is achieved when spectral HB is mitigated by sweeping the gain and thus saturating the gain evenly. Spatial HB is mitigated via frequency mismatch of the counter-propagating waves that are present in a Fabry-Pérot cavity. We show later that the introduction of AM also potentially reduces spatial HB. The actual shape of the time domain profile will be determined by the level of influence of spectral and spatial HB, and which mechanism dominates. Due to the presence of a slow modulating linear ramp we suggest in this paper that spatial HB plays a more significant role.

Bloch model for FM QCL

We are now prepared to derive the Bloch equations for the two level system, but first we must customize the equation to fit the operational characteristics of the QCL. To do this we reduce the system to two levels and phenomenologically introduce the pumping current and relaxation. Additionally, because the QCL is inhomogeneously broadened to expand the comb bandwidth, we must introduce inhomogeneity to the system as well. This derivation follows work published by the author in 2017 [47].

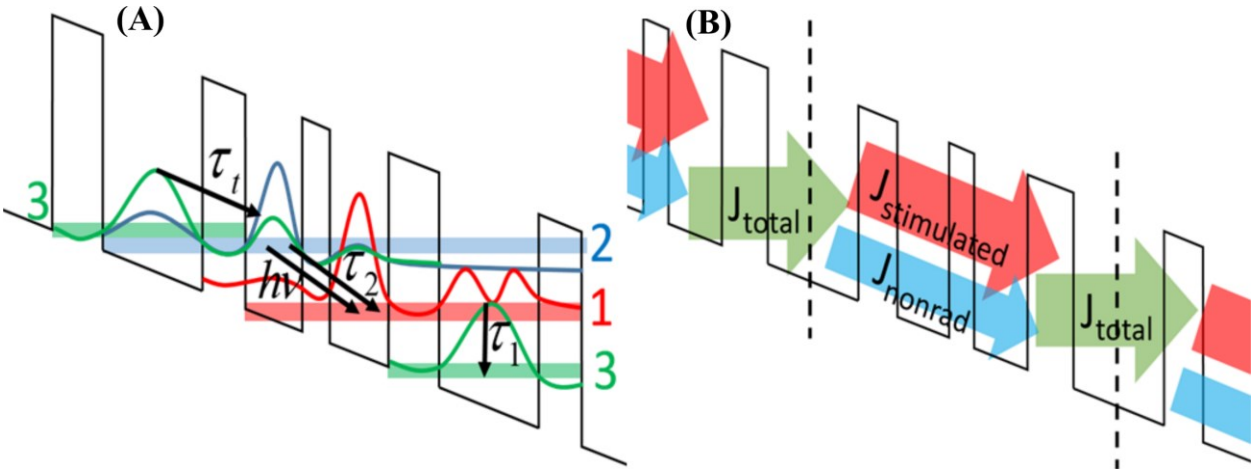

Figure 2- 4. A) Drawing of levels in one period of QCL, and (B) dissection of current, recycled through periodic structure.

First, as shown Figure 2-4A, we approximate each period of the QCL by a 3-level scheme comprised of the injection level (level 3), upper laser level (ULL), and lower laser level (LLL), subsequently followed by the next injection level. As the electrons passes through each period they either undergo a non-radiative transition or contribute to stimulated emission, obviously the regime with the highest stimulated emission current $J_{stim} \sim \gamma(z,t)I(z,t)$ and lowest non-radiative current will be the most efficient.

As shown in Figure 2-4. , the lifetime of the ULL is τ_2 , depopulation of the LLL is achieved at a rate τ_1^{-1} and injection into the ULL from level 3 occurs at a tunneling rate τ_t^{-1} . While it is possible to use density matrix theory for more than two levels and a single period of the QCL is in fact comprised of more than 3 levels it is desirable to reduce the model to a two-level system in order to decrease computational requirements. In a typical THz QCL this approximation is close to the reality while in a mid-IR QCL there are more injector layers between levels 1 and 3, however this difference can simply be addressed by changing injection parameters of the two

level system. The depopulation time τ_1 in our simplified model is the effective time that includes the relaxation rate of LLL per se and the transport through the injector to the level 3.

The inhomogeneously broadened three level system is described by a set of N density matrices $\rho^{(n)}$, with lasing transitions having resonance frequencies $\omega_{21}^{(n)}$ spread around the mean transition frequency $\bar{\omega}_{21}$ according to a normalized distribution function $f^{(n)} = f(\omega_{21}^{(n)} - \omega_{21})$, the shape of which is defined to be super Gaussian. Due to charge neutrality, the populations of the three levels are related to the diagonal density matrix elements as $N_i = N_{2D} \sum_n^N f^{(n)} \rho_{ii}^{(n)}$

where N_{2D} is the two dimensional doping density and $\sum_{i=1.}^{3} \rho_{ii}^{(n)} = 1$ which allows us to not consider $\rho_{33}^{(n)}$ in the rate equations. For each spectral bin the 2x2 density matrix $\rho^{(n)}$ evolves as

$$\frac{d}{dt}\rho^{(n)} = -\frac{j}{\hbar}\left[H_0^{(n)} + H_{filed}^{(n)}, \rho^{(n)} \right] + R^{(n)}, \tag{2.31}$$

where the Hamiltonian of the atom is

$$H_0^{(n)} = \hbar \begin{bmatrix} \omega_{21}^{(n)}/2 & 0 \\ 0 & -\omega_{21}^{(n)}/2 \end{bmatrix}. \tag{2.32}$$

The optical field Hamiltonian as defined in (2.27), setting $E = E_0 \cos(\omega_0 t + \phi_{FM}(t))$ to include the frequency modulation seen in QCLs, come out as

$$H_{field} = \hbar \begin{bmatrix} 0 & \Omega\cos(\omega_0 t + \phi_{FM}(t)) \\ \Omega\cos(\omega_0 t + \phi_{FM}(t)) & 0 \end{bmatrix} \tag{2.33}$$

Where $\Omega = qz_{12}E_0/\hbar$ is the Rabi frequency and z_{12} is the dipole moment of the transition as defined earlier.

We will pause here a moment to discuss what makes a transition "coherent" and how that effects the system. Obviously, Ω is related to the electric field amplitude as shown earlier, and thus is related to the laser intensity. However, the Rabi frequency is also related to the dipole matrix element that couples two states, and thus the population coherently oscillates with the radiation. The coupling of the two states introduces phase into the system and noting that Ω is an angular frequency we can easily see that given the right conditions the population can fully oscillate between excited and not despite the rate equation evaluation saying that maximum population inversion is only ½. The frequency at which the population oscillates is the Rabi frequency.

The phenomenologically introduced pumping /scattering matrix is then

$$R^{(n)} = \begin{bmatrix} \rho_{22}^{(n)}\tau_2^{-1} - \rho_{11}\tau_1^{-1} & -\rho_{11}^{(n)}\tau_{coh}^{-1} \\ -\rho_{21}^{(n)}\tau_{coh}^{-1} & J^{(n)}/qf^{(n)}N_{2D} - \rho_{22}^{(n)}\tau_2^{-1} \end{bmatrix}. \tag{2.34}$$

Here τ represents relaxation times and the subscript represents the level from which the carriers are relaxing, in the case of τ_{coh} , this is the coherence time of the transition. Where coherence is lost due to inter and intra-subband scattering as mentioned in chapter 1. Typical coherence times are sub-picosecond for the QCLs whereas the upperstate, level 2 lifetime of the QCL is also only in the range of 1-10 ps. Continuing, $J^{(n)} = f^{(n)}J$ is the fraction of the total current density J , carried by the fraction of 2D electrons passing through the quantum wells with resonant frequency $\omega_{21}^{(n)}$. Obviously, this means that in the absence of lasing, the density

matrix for each spectral bin is pumped to the same initial state

$\rho_{22,0}^{(n)} = J\tau_2 / qN_D$; $\rho_{11,0}^{(n)} = \rho_{22,0}^{(n)}\tau_1 / \tau_2$ with the population inversion $\Delta\rho_0^{(n)} = J\left(\tau_2 - \tau_1\right)/qN_D$. As the QCL is pumped by a constant current source we can write for the total current density

$$\frac{J}{qN_{2D}} = \frac{\rho_{33}^{(n)} - \rho_{22}^{(n)}}{\tau_t^{(n)}} = \frac{\rho_{11}^{(n)}}{\tau_1^{(n)}}. \tag{2.35}$$

This means that once lasing commences both the tunneling time and the effective depopulation time will change to assure that the current remains constant (but the voltage drop on each QCL period will change). Because $\sum_{i=1.}^{3}\rho_{ii}^{(n)} = 1$, one obtains $J = qN_D/(\tau_1 + 2\tau_2 + \tau_t)$ and the maximum population inversion attainable in the QCL is $\Delta\rho_{\max}^{(n)} = \left(\tau_2 - \tau_1\right)/(\tau_1 + 2\tau_2 + \tau_t) < 1/2$. With doping densities in the $\sim 1\times 10^{10} cm^{-2}$ range and depopulation values in the few ps range one can expect current densities on the order of $500 A/cm^2$ for THz QCLs and in the kA/cm^2 for mid-IR/Long wave QCLS.

With all of the above definitions (2.31) Becomes

$$\begin{aligned}
\frac{d}{dt}\rho_{11}^{(n)} &= j\left(\rho_{21}^{(n)}\Omega - \rho_{12}^{(n)}\Omega\right)\cos(\omega_o t + \phi_{FM}(t)) + \frac{\rho_{22}^{(n)}}{\tau_2} - \frac{\rho_{11}^{(n)}}{\tau_1} \\
\frac{d}{dt}\rho_{22}^{(n)} &= -j\left(\rho_{21}^{(n)}\Omega - \rho_{12}^{(n)}\Omega\right)\cos(\omega_o t + \phi_{FM}(t)) + \frac{J}{qN_d} - \frac{\rho_{22}^{(n)}}{\tau_2} \\
\frac{d}{dt}\rho_{21}^{(n)} &= -j\omega_{21}^{(n)}\rho_{21}^{(n)} - j(\rho_{22}^{(n)} - \rho_{11}^{(n)})\Omega\cos(\omega_o t + \phi_{FM}(t)) - \frac{\rho_{21}^{(n)}}{\tau_{coh}}.
\end{aligned} \tag{2.36}$$

Introducing the rotating wave approximation $\rho_{21} = \sigma_{21}e^{-j\omega_o t - \phi_{FM}(t)}$ and $\rho_{12} = \sigma_{12}e^{+j\omega_o t + \phi_{FM}(t)}$ we obtain

$$\begin{aligned}
\frac{d}{dt}\rho_{11}^{(n)} &= -\Omega\,\mathrm{Im}(\sigma_{21}^{(n)}) + \frac{\rho_{22}^{(n)}}{\tau_2} - \frac{\rho_{11}^{(n)}}{\tau_1} \\
\frac{d}{dt}\rho_{22}^{(n)} &= \Omega\,\mathrm{Im}(\sigma_{21}^{(n)}) + \frac{J}{qN_d} - \frac{\rho_{22}^{(n)}}{\tau_2} \\
\frac{d}{dt}\sigma_{21}^{(n)} &= -j\sigma_{21}^{(n)}(\omega_{21}^{(n)} - \omega_o - \omega_{fm}) - j(\rho_{22}^{(n)} - \rho_{11}^{(n)})\frac{\Omega}{2} - \frac{\sigma_{21}^{(n)}}{\tau_{coh}}.
\end{aligned} \tag{2.37}$$

Now, expressing the level populations as $\rho_{11}^{(n)} = J\tau_1 / qN_{2D}$ and $\rho_{22}^{(n)} = \Delta\rho + J\tau_1 / qN_{2D}$ we immediately get a result for the population inversion $\Delta\rho^{(n)}$ and polarization $\sigma_{21}^{(n)}$ of the nth inhomogeneously broadened transition:

$$\begin{aligned}
\frac{d}{dt}\Delta\rho^{(n)} &= 2\frac{J}{qN_d}(1 - \frac{\tau_1}{\tau_2}) - \frac{2\Delta\rho^{(n)}}{\tau_2} + 2\Omega\,\mathrm{Im}(\sigma_{21}^{(n)}) \\
\frac{d}{dt}\sigma_{21}^{(n)} &= -j\left(\omega_{21} - \omega_n + \omega_{FM}(t)\right)\sigma_{21}^{(n)} - j\Delta\rho^{(n)}\frac{\Omega}{2} - \frac{\sigma_{21}^{(n)}}{\tau_{coh}}.
\end{aligned} \tag{2.38}$$

Finally, after we normalize the time and all relevant frequencies to the coherence time as

$$\begin{aligned}
\tau &= t / \tau_{coh} \\
\Omega' &= \Omega\tau_{coh} \\
\Delta\omega'_n(t) &= \left(\omega_{21}^{(n)} - \omega_o + \omega_{FM}(t)\right)\tau_{coh},
\end{aligned} \tag{2.39}$$

we obtain what amounts to be customized optical Bloch equations (splitting the polarizations, σ_{21}, into real and imaginary parts)

$$\begin{aligned}
\frac{d}{d\tau}\Delta\rho^{(n)} &= \frac{2(\Delta\rho_o - \Delta\rho^{(n)})}{T} + 2\Omega'\,\mathrm{Im}(\sigma_{21}^{(n)}) \\
\frac{d}{d\tau}\sigma_{21}^{(n)} &= -j\Delta\omega'_n(\tau)\sigma_{21}^{(n)} - j\Delta\rho^{(n)}\frac{\Omega'}{2} - \sigma_{21}^{(n)}
\end{aligned} \tag{2.40}$$

where $T = \tau_2 / \tau_{coh}$. We shall refer to (2.40) as the "coherent" equations as it takes into account dynamics of the polarization on a scale comparable to or faster than τ_{coh} .

The Time Domain Model, a Rate Equation Approximation

If, on the other hand, the rate of FM is slower than coherence time, i.e. $d / d\tau << 1$, then the polarization follows the optical field adiabatically as

$$\sigma_{21}^{(n)}(t) = -\tfrac{1}{2} j\Delta\rho^{(n)}\Omega'/[1 + j\Delta\omega'_n(t)], \tag{2.41}$$

and one obtains the "incoherent" or "rate equation" approximation from the dynamics of level populations only.

$$\frac{d}{d\tau}\Delta\rho^{(n)} = \frac{2(\Delta\rho_o - \Delta\rho^{(n)})}{T} - \frac{\Omega'^2\,\Delta\rho^{(n)}}{1 + \Delta\omega'^{\,2}_n(\tau)} \tag{2.42}$$

At this point there is no longer a single term with phase, only the squared Rabi frequency is present and phase is lost, thus this equation represents intensity and population only where

$$I = \frac{\hbar}{q^2 z_{12}^2 2\eta_0} \tag{2.43}$$

Now, before we proceed, it makes sense to introduce the relation between the variables in the rate equation and actual observable parameters of the QCL. We define the instant saturation intensity for each "frequency bin" as

$$I_{sat}^{(n)}(\tau) = \frac{\overline{n}\hbar}{\tau_2 \tau_{coh} z_{21}^{\,2} 4\pi\alpha_o}\frac{(\tau))}{}, \tag{2.44}$$

where α_0 is the fine structure constant and $\overline{n}$ is the background index, and re-write (2.42) as

$$\frac{d}{d\tau}\Delta\rho^{(n)} = \frac{2\Delta\rho_o}{T} - \frac{2\Delta\rho^{(n)}}{T}\left[1 + I / I_{sat}^{(n)}(\tau)\right] \tag{2.45}$$

The mean saturation intensity at which the gain decreases to ½ its original value can be found out as

$$\bar{I}_{sat} = \frac{\bar{n}\hbar}{\tau_2 \tau_{coh} z_{21}{}^2 4\pi\alpha_o} \tag{2.46}$$

where the value of $\Delta\bar{\omega}$'is commensurate with $\Delta\omega_{gain}\tau_{coh}$, i.e. the ratio of inhomogeneous and homogeneous broadening. Using typical values as mentioned earlier and estimating a dipole moment, z_{21} of 4-6nm for THz and slightly smaller (~2nm) for LWIR, we arrive with a saturation intensity in the vicinity of $500 MW / cm^2$. It is important that the laser achieve some level of intensity that is not too much less than $\bar{I}_{sat}$ as the effects gained by FM will not be prevalent otherwise.

We shall also establish a relation between the density matrix elements in (2.40) and (2.45) as well as another observable parameter, gain. For that we first find the expected value of the dipole moment for each transition n,

$$\begin{aligned} \left\langle \mu^{(n)} \right\rangle &= Tr(\rho^{(n)}\mu) = qTr\left(\begin{pmatrix} \rho_{11}{}^{(n)} & \rho_{12}{}^{(n)} \\ \rho_{21}{}^{(n)} & \rho_{22}{}^{(n)} \end{pmatrix}\begin{pmatrix} 0 & z_{12} \\ z_{21} & 0 \end{pmatrix}\right) = \\ &= q z_{21}\sigma_{21}^{(n)} e^{j\omega t} + c.c. \end{aligned} \tag{2.47}$$

The material polarization is then

$$P(t) = \frac{N_{2D}}{W}\sum_N \left\langle f_n \mu^{(n)} \right\rangle = \frac{2N_{2D}}{W}\frac{q^2 z_{21}^2 \tau_{coh}}{\hbar} \sum f_n \sigma_{21}^{(n)}(t)\frac{E_0}{2} e^{j\omega t} + c.c. \tag{2.48}$$

where W is the period thickness. Substituting (2.48) into the Helmholtz equation for the slow variable envelope

$$2jk_0\bar{n}\frac{dE}{dz} = -\frac{\omega_0^2}{c^2\epsilon} P \tag{2.49}$$

we obtain

$$\frac{dE_0}{dz} = k_0 \frac{N_{2D}}{W}\frac{q^2 z_{21}^2 \tau_{coh}}{\bar{n}\epsilon} \nabla \cdot \mathrm{Im}\,\sigma_{21}^{(n)}(t)E_0 = \frac{\gamma}{2}E_0. \tag{2.50}$$

Hence the instant gain coefficient is

$$\gamma(t) = \Gamma \frac{8\pi\alpha_0 N_{2D} z_{21}^2}{n_{eff} W}\omega\tau_{coh}\sum_N f_n \frac{\mathrm{Im}\,\sigma_{21}^{(n)}(t)}{\Omega'(t)}, \tag{2.51}$$

where the Rabi frequency is in general time–dependent (to accommodate amplitude modulated signals but at a much slower rate than the optical frequency), and we introduced the confinement factor of the cavity Γ and the effective mode index n_{eff}. In THz QCLs $\Gamma \sim 1$ due to the confinement of the metal-metal waveguide, and $n_{eff} \approx \bar{n}$. For mid-IR lasers the confinement factor is somewhat smaller but the effective index is not changed much.

With the incoherent approximation (2.41) the instant gain reduces to

$$\gamma(t) = \Gamma\sum_n f^{(n)} \frac{4\pi\alpha_0}{n_{eff}}\frac{N_{2D}}{W}\frac{z_{21}{}^2\omega_o\tau_{coh}\Delta\rho^{(n)}}{(1+\Delta\bar{\omega}'^2)} \tag{2.52}$$

Now, in order to find out which FM format leads to the lowest threshold of the QCL in the presence of spatial hole burning we will eventually need to solve the equations for density

matrix elements (2.40) or (2.42) in which the variables depend not only on time and frequency but also on the spatial coordinate z, where the step of z should be much less than wavelength. This may present computational difficulties, therefore prior to going full throttle and incorporating spatial hole burning we shall investigate whether the full coherent model is necessary by considering only spectral hole burning.

Investigating the time dynamics of the QCL

While we expect some small differences between a Mid-IR and THz QCL, The device parameters used in our test of coherence have been chosen to correspond to a "diagonal transition" THz QCL that has successfully produced FCs [4, 48, 49] , having a broad gain with $\Delta\nu_{gain} = 2THz$ centered at the lasing frequency of $\nu_0 = 3THz$, a dipole moment $z_{12} = 5nm$, gain recovery time $\tau_2 = 4ps$, coherence time $\tau_{coh} = 0.7ps$ and LL depopulation time $\tau_1 = 0.5ps$. The active region of the QCL is doped with two dimensional doping density $N_{2D} = 3.5\times10^{10} cm^{-2}$ over an effective thickness of one period, W = 57nm. Injected current density is J=500 A/cm2, and the power inside the cavity is approximately 25mW corresponding to $\Omega' = 0.78$. With these values we can calculate a saturation power of ~83mW given an absolute value of average detuning $\overline{\Delta f} = 0.5THz$, hence the intracavity power of 25mW amounted to 30% of the saturation intensity and an unsaturated gain around 50 cm-1. This is sufficient to exceed the laser threshold by a factor approaching 1.5-2 and cause saturation which should make the differences between various FM regimes tested below discernible. All of these values are in general agreement with experimental results [4, 48-50]. As we have already seen from [5] which was later confirmed experimentally [39] the QCL is frequency modulated, for the purpose

of this coherence test we introduce a periodic, sinusoidal signal in order to easily control the period of frequency modulation and thus measure the temporal behavior of the system. We therefore consider periodic FM signals, with instant frequency varying as $\nu_R(t) = A_{FM}\sin(2\pi t / T_{FM})$ and monitor two parameters: average gain experienced by photons $\bar{\gamma} = T_{FM}^{-1}\int_{t}^{t+T_{FM}} \gamma(t)dt$ and the average relaxation current $\bar{J}_{rel} = q\tau_2^{-1}T_{FM}^{-1}\sum_n f_n \int_{t}^{t+T_{FM}} \Delta\rho^{(n)}(t)dt$ in order to monitor maximum emission regimes and the disparities between the two equations.

The results of modeling using both coherent (OBE) and incoherent (rate equations) approaches are shown in Fig2-5. In Fig2-5a the value of the average gain $\bar{\gamma}$ vs. T_{FM} is shown for the two approaches and compared to the no-FM case (circles). Clearly, FM does increase the effective gain experienced by the photons and reduces the wasteful relaxation current. Both "coherent" and "incoherent" approaches show the same trend for large FM periods – a steady decline as T_{FM} increases. This is a predictable trend, for a large T_{FM} the instant frequency of the laser would dwell in the same spectral region for a time longer than τ_2 and hence the spectral hole would have enough time to develop and $\bar{\gamma}$ would decrease. At the same time, population inversion outside the spectral hole region remains undepleted by stimulated emission which causes an increased relaxation current $\bar{J}_{rel}$ as can be seen from the curves in Figure 2-5b (which, as expected, are complimentary to the curves in Fig.2-5a).

However, at short FM periods the "coherent" and "incoherent" gain curves diverge with incoherent gain exhibiting a continuing increase while the coherent gain takes a sharp dive. This decline is entirely predictable as when the period of modulation becomes first commensurate

and then shorter than the coherence time the two-level system no longer responds to FM modulation and hence all the benefits of sweeping the instant frequency over the gain bandwidth get lost. In other words, the coherent model predicts that there exists the optimum frequency of FM modulation, commensurate with $\tau_2 > \tau_{coh}$ such that on one hand the frequency sweeps through the entire gain bandwidth at a rate slightly faster than the gain recovery time and on the other hand the sweep is sufficiently slow for the system to respond to it.

Once the FM period exceeds roughly τ_2 /2 both "coherent" and "incoherent" models behave similarly showing nearly identical slopes of the $\bar{\gamma}$ vs. T_{FM} curves, hence, if one restrains T_{FM} to the values commensurate with τ_2 one can use the rate equation model to determine the most efficient QCL operating regime with a high degree of confidence. We shall use this fact in our work in the sections following this one.

The results plotted in Figures 2-5 a and b have been obtained for the FM span $2A_{FM} = 1.2THz$, which is optimum as follows from the curves in Figures 2-5 c and d. The period for Figures 2-5c and 3d is 2.88ps which is the optimum value as shown in Figures 2-5a and b. Figures 2-5c and d illustrate the relation between gain and relaxation current with the span of the FM signal, in this case the span is twice that of A_{FM} in order for a direct comparison to be made with the gain bandwidth. This result is obviously intuitive since the FM amplitude should be sufficient enough to sweep the entire gain bandwidth effectively but should not be any larger. Note that both coherent and incoherent approaches yield the same value of optimum FM amplitude and also that the curves in 2-5c and 2-5d are complimentary, as expected. At this point, the model is generally ambivalent in regards to whether the modulating signal is a single

frequency, frequency chirp, or a pseudo-random signal. It is not until the introduction of spatial hole burning that the pseudo-random nature of the modulation signal comes into play.

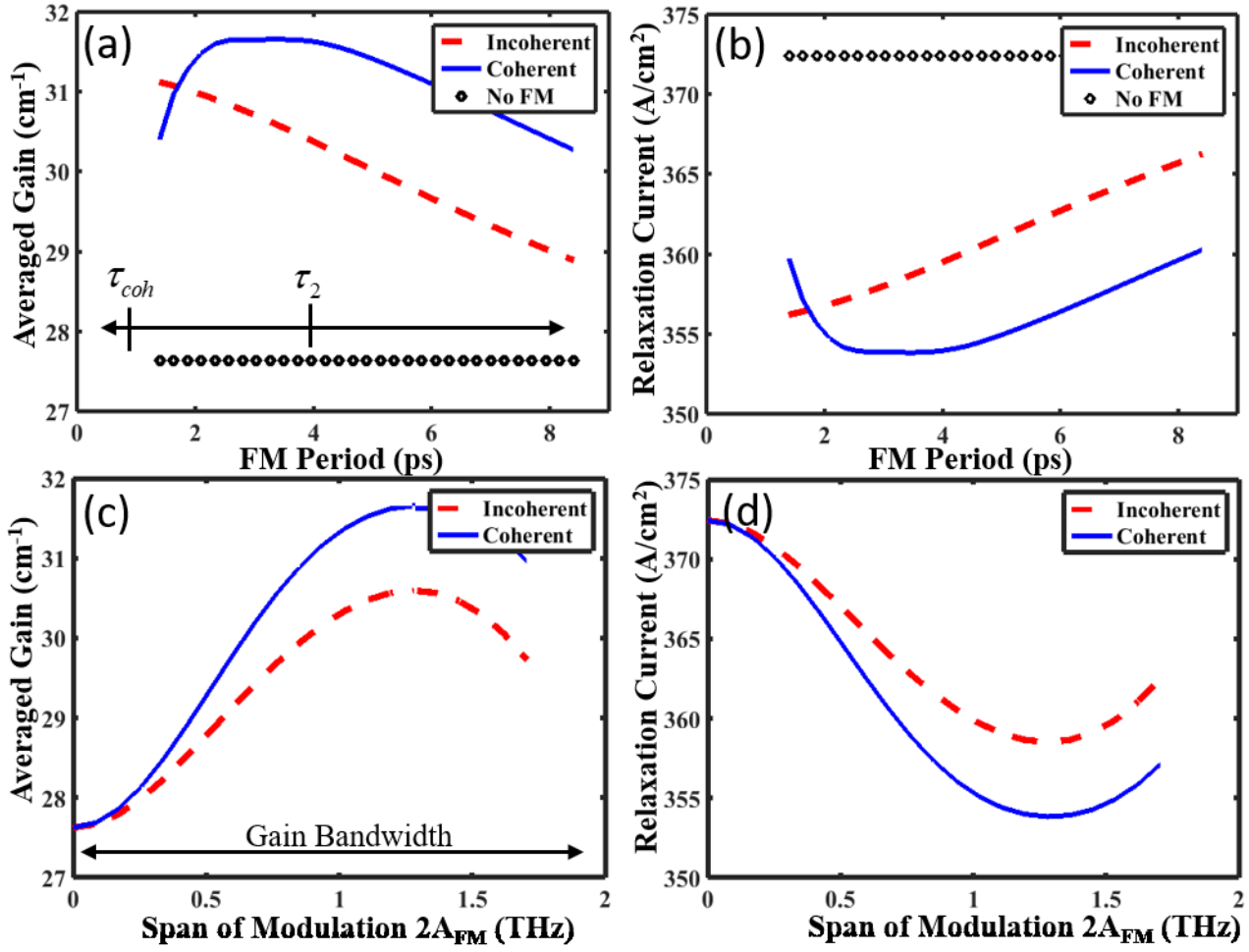

Figure 2- 5. A comparison between the incoherent, or modified rate equations, and the full coherent OBE models. Averaged gain and relaxation current vs FM signal period (a,b) and modulation amplitude (c,d) including spectral hole burning only. The data presented here is generated using a purely sinusoidal FM signal. The span of modulation used for (a,b) is 1.2THz, the optimum as shown in (c,d). The period of modulation in (c,d) is 2.88ps, the optimum shown in (a,b).

At this point, we can say with relative certainty that the dynamics captured by our customized OBEs can be done so with the adiabatic approximation introduced in (2.41), thereby greatly

reducing the computational power needed for a model that includes spatial coordinates. This is especially true for the ramp FM QCLs as the period of frequency modulation is very long and commensurate with the cavity round trip time. Thus to our knowledge all the dynamics of the QCL lasers (LWIR and THz) occur on time scales much longer than τ_{coh}, with one exception. The time period after a ramp FM QCL has completed a full span, the frequency makes a rapid jump back to the other side of the gain, this (not coincidentally) is also the time period that we see a light or dark pulse in the laser radiation. This however is hard to believe, because in fact the frequency shift is so rapid that it is doubtful that the two laser levels would even recognize it. More likely the rapid frequency jump is a measurement artifact or a strong coupling between amplitude and phase of the emission.

Amplitude Modulation with Spectral Hole Burning Only

Before introducing spatial hole burning into our model it is a useful exercise to explore the effect of introducing amplitude modulation in addition to frequency modulation. This is very likely to occur in QCL devices as a result of cavity dispersion, and in fact simultaneous AM and FM is always seen in real devices[39]. In addition to this, one can expect some level of AM to arise from the process of frequency modulation itself. As the mode is frequency modulated and approaches the edge of the gain one would expect a decrease in the gain seen and thus some modulation of intensity. As expected, and shown in Figure 2-6, the effect of AM is exactly opposite that of FM, namely the gain experienced by the light decreases with increasing AM depth. As we have mentioned already, the medium with the fast saturable gain always favors the CW amplitude and ideally (meaning no dispersion and a very broad spectrum) will keep

"flattening" the signal until CW amplitude is achieved as shown in the frequency domain model [5].

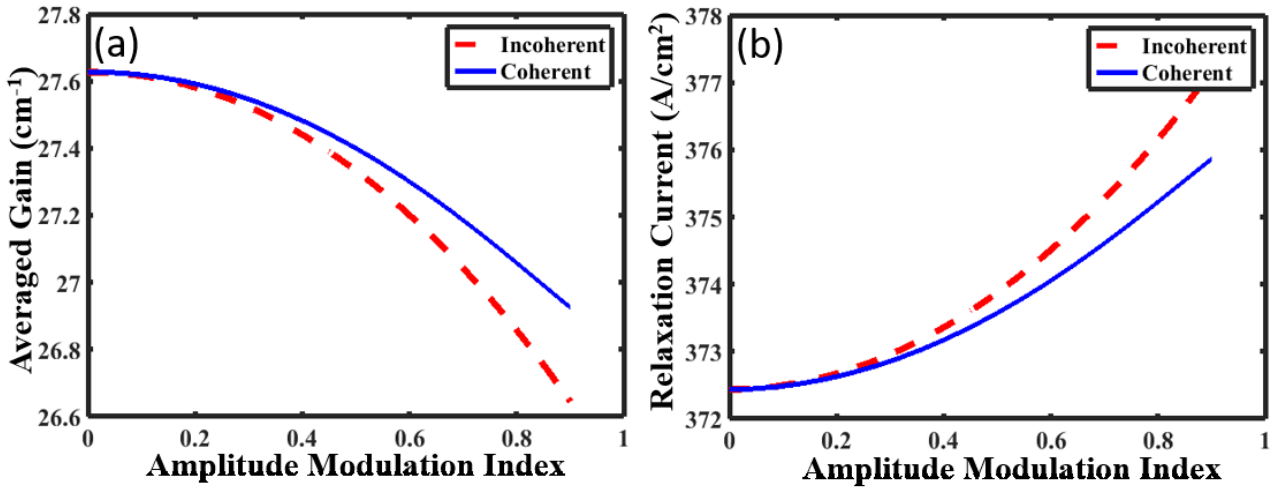

Figure 2- 6. The effect of amplitude modulation on gain**(a)** and nonradiative decay**(b).**

The results shown here are for a sinusoidal amplitude modulation in a model that has not yet included spatial hole burning, which we will soon see has a large role to play in the dynamics of the laser. We now know that QCLs do indeed have some form of amplitude modulation that is larger than expected, that some even argue to be pulses. Therefore these results can be slightly misleading, and we will address amplitude modulation further in the next chapter. What can be interpreted from these results is that in an ideal system where no spatial hole burning happens, the fast gain saturation of the system will favor a CW radiation and introduction of AM into the system will decrease the laser efficiency.

Conclusion

To conclude, in this chapter we have introduced the Maxwell Bloch equations and shown how we customize them in order to more closely model a real world quantum cascade laser. While

this laser is four levels, we reduce it to a two level system and account for continuity of current. We make a further approximation of the system under the assumption that the temporal dynamics of the laser are much slower than the rate of coherence loss. Under this assumption we show that a simple modified rate equation can appropriately quantify the gain and relaxation current of the laser under a sinusoidal frequency modulation, or detuning. We further show that amplitude modulation can harm the efficiency of the laser, this however is not ubiquitously true as will be shown later on in this dissertation.

.

Chapter 3: Investigating Spatial Hole Burning

We now turn our attention to the main issue facing us, namely how does spatial hole burning select the most effective operating regime of the QCL? This arises, as shown in Figure 1a below, from counter-propagating waves in the Fabry-Perot cavity creating a standing wave pattern. An example standing wave pattern is shown in Figure 3-1b, where two counter-propagating waves with sinusoidal FM produce the spatial pattern of peaks and troughs. For comparison, Figure 3-1b also shows the very rapid oscillations of intensity present from a single mode laser. These peaks occur when the counter-propagating waves meet with matching frequencies.

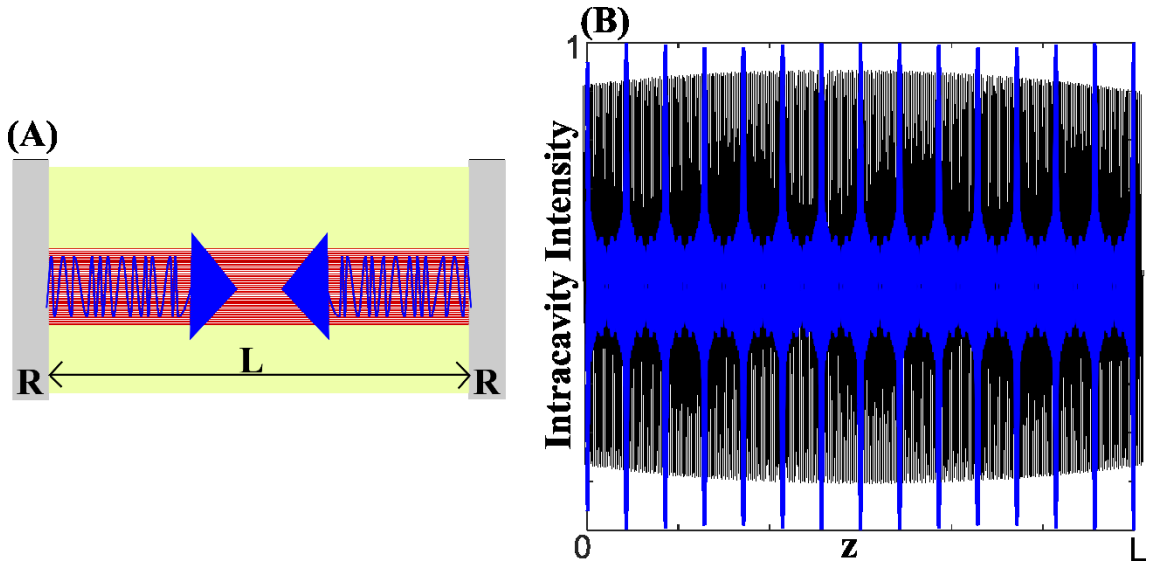

Figure 3- 1. A) Cartoon of two pseudorandom FM waves counterpropagating inside the laser cavity. B) The resulting spatial intensity from a deterministic, sinusoidal FM (blue spikes) and from a CW laser for comparison (rapid oscillation in the background).

At this point, the model is developed to be three dimensional in that it tracks the population for position, time, and spectral frequency, however it is useful to investigate the mechanisms behind spatial hole burning rather than simply plugging in a spatially dependent Rabi frequency

and seeing what results. To do that we must introduce a standard by which we will measure the extent of spatial hole burning, this is the variance of the spatial distribution, $\sigma^2 \equiv \left\langle (X-\mu)^2 \right\rangle_z$, resulting from the counter-propagating waves commonly present in a fabry-perot cavity. Thus we introduce spatial variance by considering its effect on the gain. The power density distribution inside the cavity $p(z,t)$ is normalized to the saturation power density and the gain medium acts as an "integrator" with the characteristic time equal to the gain recovery time, i.e. it responds to the averaged power

$$\left\langle p(z,t) \right\rangle_{\tau_2} = \int_{-\infty}^{t} p(z,\tau) e^{\frac{\tau - t}{\tau_2}} d\tau = \overline{p} + \delta p(z,t) \qquad (3.1)$$

where the second term describes the spatial variations in $p(z,t)$, occurring on a time scale longer than the gain recovery time, to which the gain medium can actually react. If the uniform unsaturated gain in the medium is γ_0 it then saturates as $\gamma(z,t) = \gamma_0 / (1 + p(z,t))$. The average gain experienced by the photon is then

$$\overline{\gamma} = \frac{\left\langle \gamma(z,t) p(z,t) \right\rangle_{z,t}}{\overline{p}} = \frac{\gamma_0}{\overline{p}} \left\langle \frac{\overline{p} + \delta p(z,t)}{1 + \overline{p} + \delta p(z,t)} \right\rangle_{z,t} \approx \frac{\gamma_0}{1+\overline{p}} \left[1 - \frac{\left\langle \delta p^2 \right\rangle_{z,t}}{\overline{p}(1+\overline{p})^2} \right] \approx \frac{\gamma_0}{1+\overline{p}} \left[1 - \overline{p} \sigma_p^2 \right], \quad (3.2)$$

where the variance is defined as

$$\sigma_p^2 = \left\langle \delta p^2(x,t) \right\rangle_{t,z} / \overline{p}^2. \qquad (3.3)$$

Furthermore, the relaxation current itself is proportional to the gain

$$\bar{J}_{rel} \sim \langle \gamma(z,t) \rangle_{z,t} = \gamma_0 \left\langle \frac{1}{1+\bar{p}+\delta p(z,t)} \right\rangle_{z,t} \approx \frac{\gamma_0}{1+\bar{p}} \left[1 + \frac{\langle \delta p^2 \rangle_{z,t}}{(1+\bar{p})^2} \right] \approx \frac{\gamma_0}{1+\bar{p}} \left[1 + \bar{p}^2 \sigma_p^2 \right], \quad (3.4)$$

indicating that, in accordance with expectations, the average gain and relaxation current behave in a complimentary fashion and spatial hole burning results in less gain seen by the field. For the single standing mode one can calculate that $\sigma_{p,0}^2 = \frac{1}{2\pi} \int_0^{2\pi} (2\sin^2(x) - 1)^2 = \frac{1}{2}$. This is the absolute worst-case scenario and thus we look for a variance much smaller than this value to show a marked improvement on the spatial hole burning of the FM signal over a non-modulated signal.

Conceptual analysis of FM Signals

Before calculating the intracavity variance of possible FM waveforms, we provide here a conceptual analysis of the impact of spatial hole burning. While the FD model explains why FM modulation is desirable and we can postulate why it produced a waveform with an average period commensurate with the gain recovery time τ_2, what it does not explain is why the signal is always aperiodic on a small scale within one round trip time, τ_{rt}. In Figure 3-2 we show the instant frequency for five different FM signals (column 1), their spectra (column 2) and the power density distribution inside the laser cavity (column 3) of length $L = v_g \tau_{rt} / 2$, where v_g is the group velocity. The power density profiles are the result of the addition of two counter-propagating waves, in other words the light interfering with a delayed (by $\Delta t = 2z / v_g$, $0 < \Delta t < T_c$) version of itself,

$$I(z,t) = \left| A_1(z)E(t+\Delta t/2)e^{j(kz-\omega_0 t)} + A_2(z)E(t-\Delta t/2)e^{-j(kz+\omega_0 t)} \right|^2 \quad (3.5),$$

where $$E(t) = E_0 \exp\left(-i\int \omega_{FM}(t)dt\right) \quad (3.6),$$

and the normalized amplitudes $A_1^2(z) = [2R + (2-2R)z/L]/(1+R)$ and $A_2^2(z) = [2-(2-2R)z/L]/(1+R)$ account for the boundary conditions at the edges with reflectivity R. For mid-IR, R~30% was calculated for an uncoated facet using Fresnel formula. However, for THz QCL's R is typically much higher, 70-80%, this is due to the metal-metal waveguide structure and impedance mismatch at the cavity facet [51]. Importantly, because the gain medium does not saturate instantly we use the power density averaged over the gain recovery time, or $\langle I(z,t)\rangle_{\tau_2} = \tau_2^{-1}\int_0^\infty I(z,t-\tau)\exp(-\tau/\tau_2)d\tau$. Let us now see how the character of FM affects the gain saturation.

For the non-FM signal, $\omega_{FM}(t) \equiv \omega_0$ shown in upper row (Figure 3-2a), one can see that in addition to a deep, central spectral hole, the spatial hole is also expected to be burned as the intensity represents a standing wave pattern of peaks and troughs, shown in the last column. In the next row (Figure 3-2b), the frequency mimics what has been seen experimentally, i.e. a linear frequency chirp, however we do not include amplitude modulation as that would significantly increase the spatial hole burning. This obviously gives a very good spatial distribution as the frequencies counter-propagating in the cavity can never be equal (except close to the mirrors). In Figure 3-2c the frequency is modulated with a period equal to the round trip time, $\omega_{FM}(t) = \omega_0 + 2\pi A_{FM}\sin(2\pi t/\tau_{rt})$, resulting in a dense comb spaced by the

axial frequency. The spatial intensity pattern $\langle I(z,t)\rangle_{\tau_2}$ in Figure 3-2c column 3 shows greatly reduced oscillations as the instant frequencies of two counter-propagating waves are always different except at the mirrors, thus no spatial hole burning is expected. This scenario is very similar to the ramp FM in that very little spatial hole burning is expected due to the period of the modulation. While prospects look bright in the spatial domain, the performance may suffer from spectral hole burning, just as the ramp FM QCLs might. As stated before, FM allows for the gain at some frequency to recover as the radiation detunes from its resonance. However, after the gain recovers at the rate τ_2^{-1}, further pumping is converted into non-radiative decay. Thus, for efficient operation, the radiation should return to its original frequency within the gain recovery time (τ_2). In other words for the most efficient QCL FC the period of FM modulation, T_{FM} is on the order of the gain recovery time, indicating that the FM signal shown in Figure 3-2c is not optimum. However, we must be careful because, although we can postulate what the most efficient QCL would act like, there are other factors that can affect the laser dynamics as well such as dispersion, asymmetric gain, etc [28, 46, 52]. Also the relative strengths between temporal, spatial, and spectral hole burning must be weighed as the perfect waveform to fix one kind of hole burning might worsen another.

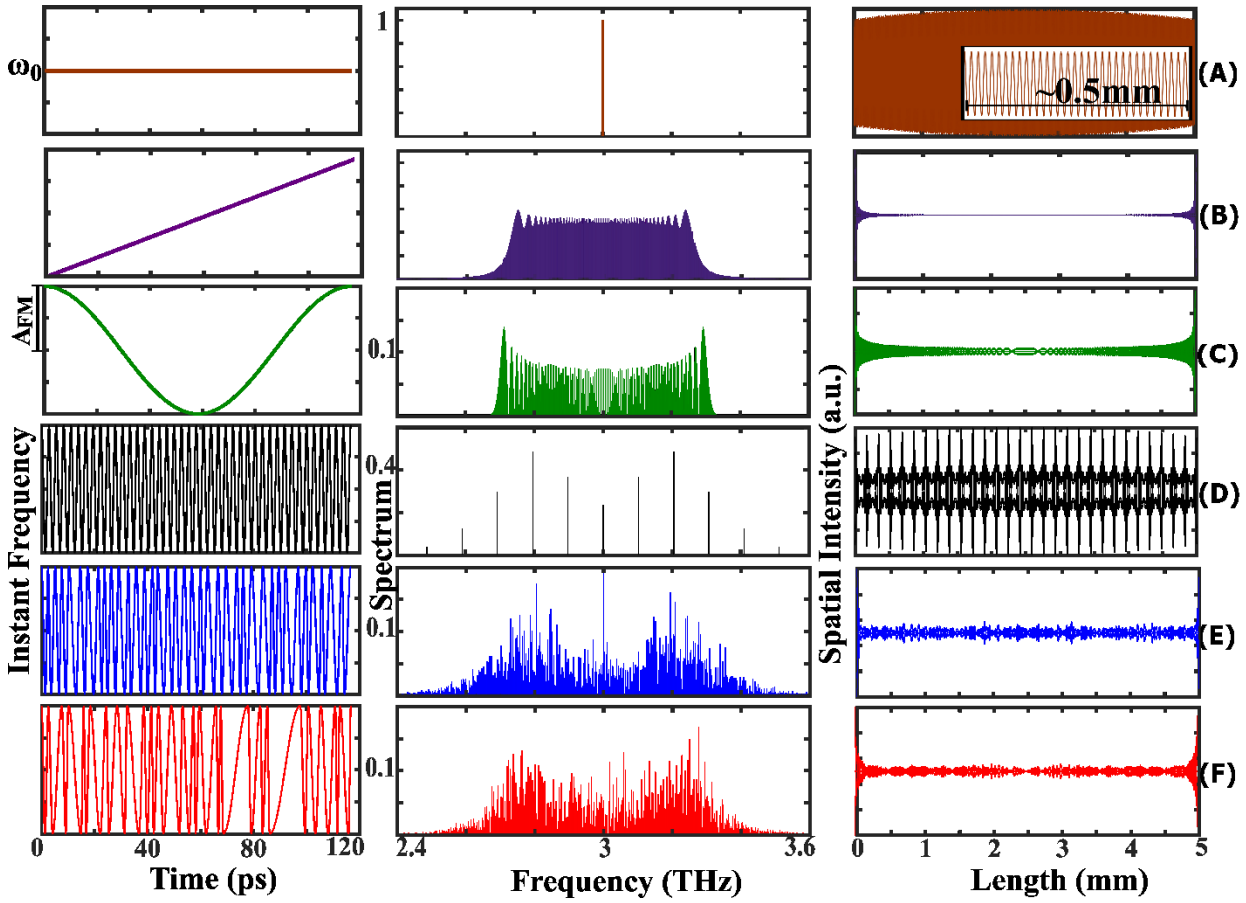

Figure 3- 2. Instant frequency deviation, power spectrum, and spatial distribution for an Intracavity field with (a) no frequency modulation (b) ramp FM frequency modulation with a period equal to the round trip time (c) non-random frequency modulation with a modulation period equal to the cavity round-trip time, (d) non-random frequency modulation with a period equal to the gain recovery time, (e) random frequency modulation, ($\delta = 0.5$) with mean period equal to the gain recovery time, (f) very random frequency ($\delta = 0.9$) modulation.

There are in fact regimes of operation in many FC QCLs where many modes are skipped [53, 54], these modes of operation appear as a function of pump power and gain saturation, implying that the FM signal is periodic at a faster scale than the cavity time, in order to mitigate spectral hole burning. Similar to this scenario, when considering the deterministic FM signal whose modulation period T_{FM} is commensurate with τ_2 , $\omega_{FM}(t) = \omega_0 + 2\pi A_{FM} \sin(2\pi t m / \tau_{rt})$, where $m \sim \tau_{rt} / \tau_2$ (Figure 3-2c). This signal produces lines separated by a much larger spacing

than τ_{rt}^{-1}. For THz lasers, $m \sim 25-50$ meaning that every 25 to 50 modes are skipped, this situation is even worse for LWIR QCLs where τ_{rt} / τ_2 is larger by one order of magnitude. It is intuitively clear that the larger the number of oscillating modes, the more efficiently can the spatial hole be filled. It can be understood even better by realizing that when two counter-propagating waves, delayed by time Δt, interfere inside the cavity they have instant frequencies that differ by some fixed amount, $\Delta\omega(z)$, hence the standing wave pattern moves with the velocity $v_{pat}(z) \sim \lambda\Delta\omega(z) / 4\pi n_{eff}$. As long as $v_{pat}(z)\tau_2 > \lambda / 2n_{eff}$, i.e. $\Delta\omega(z) > 2\pi\tau_2^{-1}$, the spatial troughs and peaks will be smoothed out and averaged giving an intensity $\langle I(z,t)\rangle_\tau$ with a fairly flat profile. However, when $z \sim KL / m$, where *K* is an integer less than *m*, the two interfering waves are delayed by exactly $\Delta t \sim KT_{FM}$ and thus have nearly identical instant frequencies, causing a non-moving standing wave pattern peak in the intensity profile. Given a deterministic, sinusoidal FM signal, one can derive the z-dependent averaged intensity as

$$\langle I(z,t)\rangle_\tau = E_0^2\left[1 + J_0\left(\frac{A_{FM}\tau_{rt}}{m}\sin m\pi z / L\right)\cos(4\pi z / \lambda)\right] \quad (3.7)$$

where $J_0(x)$ is a Bessel function of the first kind giving $m = \tau_{rt} / T_{FM}$ peaks of intensity variations along the cavity length. From (3.7) it is obvious that whenever the argument of the Bessel function is zero, the swings of the intensity reach a maximum creating an undesirable standing wave pattern.

In the presence of pseudo random FM, the counter-propagating waves rarely have matched frequencies for the time period comparable to τ_2 hence the interference pattern does not stay in place but essentially oscillates back and forth, getting smoothed out. To quantify

these observations we introduce a "degree of randomness", $0 < \delta < 1$, into the expression for instant frequency $\omega_{FM} = 2\pi A_{FM} \sin\left[\bar{\omega}_m (1 + \delta R_t) t\right]$, where $\bar{\omega}_m = 2\pi / \bar{T}_{FM}$ is the mean angular frequency of the modulation, and $-1 \le R_t \le 1$ is a time dependent random number. To assure continuity of the instant frequency, the model generates a new number every $2[1 + \delta R_t]^{-1}$, or after a half period of time has passed leading to the instant frequency changing. This is shown in the right hand columns of Figs 2d and 2e with $\delta = 0.5$ and $\delta = 0.9$ respectively. As shown in the second columns of these figures, increasing the PR nature of the FM effectively spreads the spectrum, while keeping the separation of τ_{rt}^{-1}, due to its periodic nature. Importantly, the averaged intra-cavity intensity pattern shown in the last column is smooth and thus unlikely to cause significant spatial hole burning.

Comparison of Deterministic and Pseudorandom Sinusoidal Frequency Modulation

To get an idea of the significant factors controlling the power variance of the intracavity spatial intensity distribution we turn to analytical calculations of the FM signals interfering in the fabry-perot cavity. When considering only an FM signal where the frequency modulation is a cosine with modulation index $\beta = \Delta\omega / \omega_{fm}$, as shown in the first column of Fig 3-2d, where $\Delta\omega$ is the bandwidth of the gain/or frequency deviation of the FM signal and ω_{fm} is the angular frequency of the FM signal.

$$E(z) = \frac{E_0}{2} \exp\begin{Bmatrix} -j\omega_0 (t + \Delta t/2) \\ -j\beta \cos[\omega_{fm} (t + \Delta t/2)] \end{Bmatrix} + \frac{E_0}{2} \exp\begin{Bmatrix} -j\omega_0 (t - \Delta t/2) \\ -j\beta \cos[\omega_{fm} (t - \Delta t/2)] \end{Bmatrix} \qquad (3.8)$$

we can calculate the power variance as $\sigma^2 = \left\langle \left(\frac{1}{2}\cos\left(\omega_0 \Delta t + \beta \sin \omega_{fm} t \sin \omega_{fm} \Delta t / 2\right)\right)^2 \right\rangle = \frac{1}{8}$,

i.e. the same as no modulation, however when averaging over the period of modulation, assuming the period of modulation is commensurate with the upperstate lifetime, we see that the power variance decreases significantly with modulation index, see Figure 3-3. Calculating the averaged variance is a complicated integral but can be approximated with a summation

$$\sigma^2_{av} = \frac{1}{T}\int_0^T \left[\frac{1}{2} J_0\left(\beta \sin \omega_{fm} \Delta t / 2\right)\cos(\omega_0 \Delta t)\right]^2 d\Delta t \approx \frac{1}{T}\int_0^{T_m} \frac{1}{8}\left[\sum_{k=0}^{\infty} (-1)^k \frac{[(\beta \sin \omega_{fm} \Delta t / 2)^2 / 4]^k}{(k!)^2}\right]^2 d\Delta t$$

. (3.9)

This shows the power of the modulation index, and offers the conclusion that a large frequency deviation gives a small intracavity power variance.

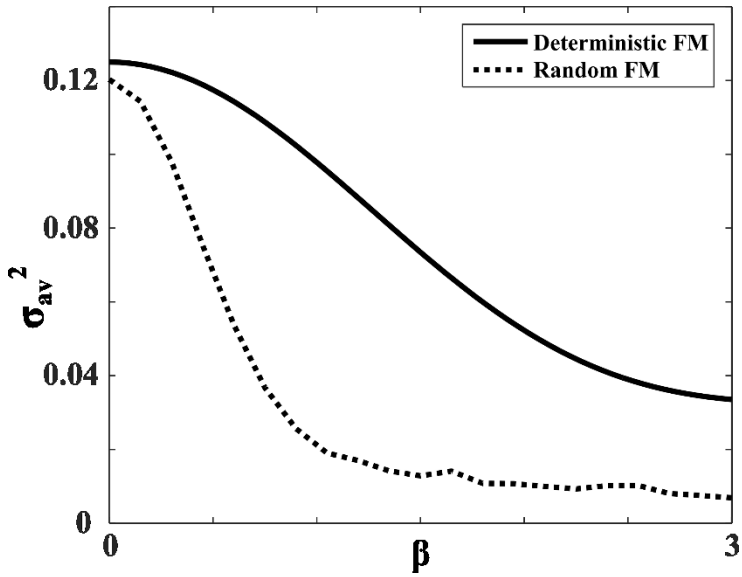

Figure 3- 3. Averaged power variance versus modulation index for a deterministic and random sinusoidal FM, with a period of oscillation commensurate with the upper state lifetime.

While much of the subsequent analysis of the inner dynamics of FC QCLs is based upon this idea of a “pseudo-random” operation, the exact form of the FM signal is less important than the insights achieved by analyzing various possible scenarios. These insights are ubiquitous to the operation of all QCLs. Much like the proposed “pseudo-random” FM QCL, the ramp FM QCL [] mitigates spatial hole burning quite well by avoiding this matching of frequencies between counter-propagating waves. It is well known that spatial hole burning can easily cause a laser to operate in multi-mode due to preferential saturation and mode competition however will also greatly reduce efficiency of the laser. By introducing a pseudo-random FM waveform more modes proliferate in the cavity and reduces spatial hole burning as shown in Fig [columns and rows fig], thus we can see the calculated variance is much lower than that of the deterministic sinusoidal variance, as shown in Fig [above].

Amplitude Modulation

Gain Saturation by a Pulse in the QCL

With the ability to measure the temporal wave-form of the radiation via SWIFTs [], significant amplitude modulation has been confirmed. There are many who believe it to be the formation of a pulse, however that is still debatable. There is too much yet unknown to fully confirm that a coherent circulating pulse is in the cavity. In typical fashion, we present here a simplistic yet very intuitive argument as to how the mode-locked pulse is not favored in the presence of a fast saturable gain. Let us now assume that a short pulse of duration τ_p propagates inside the cavity. Clearly, averaging over τ_{21} shall change the pulse duration to $\tau_p^{'} = \sqrt{\tau_p^2 + \tau_{21}^2}$.

Furthermore, if we assume that the cavity is sufficiently longer than spatial extent of the pulse,

we can neglect the effect of two counter-propagating beams interfering near the mirrors and use only averaging over the time. Therefore we can introduce the pulse energy, U_p, and calculate the averaged gain seen by the photon as

$$\bar{\gamma} = \frac{\gamma_0}{U_p} \int_0^{\tau_{rt}} \frac{p'(t)}{1+p'(t)} dt \ .$$

Next we assume some analytical form for the pulse with energy $U_p = \bar{p}\tau_{rt}$,

$$p'(t) = \frac{U_p}{\pi\tau_p'} \operatorname{sech}(t/\tau_p')$$

and

$$\frac{\bar{\gamma}}{\gamma_0} = \int_{-\tau_{rt}/2}^{\tau_{rt}/2} \frac{\frac{1}{\pi\tau_p'} \operatorname{sech}(t/\tau_p')}{1+\frac{U_p}{\pi\tau_p'} \operatorname{sech}(t/\tau_p')} dt$$

Then normalize the time to the round trip time (assuming the pulse is much shorter than round trip time) as $\tau_p'' = \tau_p' / \tau_{rt} = \tau_p' = \sqrt{\tau_p^2 + \tau_2^2} / \tau_{rt}$ so that

$$\frac{\bar{\gamma}}{\gamma_0} \approx \int_{-\infty}^{\infty} \frac{1}{\bar{p} + \pi\tau_p'' \cosh(t/\tau_p'')} dt \ .$$

The integral can be taken analytically to obtain

$$\frac{\bar{\gamma}}{\gamma_0} = \frac{4x}{\pi} \frac{\arctan\sqrt{\frac{x-1}{x+1}}}{\sqrt{x^2-1}} \ . \qquad (3.10)$$

where $x = \frac{\pi\tau_p^{''}}{\bar{p}} = \frac{\pi\tau_p^{'}}{U_p} = \sqrt{\frac{\pi^2}{\bar{p}^2}\left(\frac{\tau_p^2}{\tau_{rt}^2} + \Gamma^2\right)}$, $\tau_p^{'''} = \tau_p / \tau_{rt}$ and $\Gamma = \tau_{21} / \tau_{rt}$ plotting this for a normalize average power and choosing a realistic ratio of $\Gamma = 1/40$, one can easily see that the longer the pulse, the higher the gain as shown in Figure 3-4.

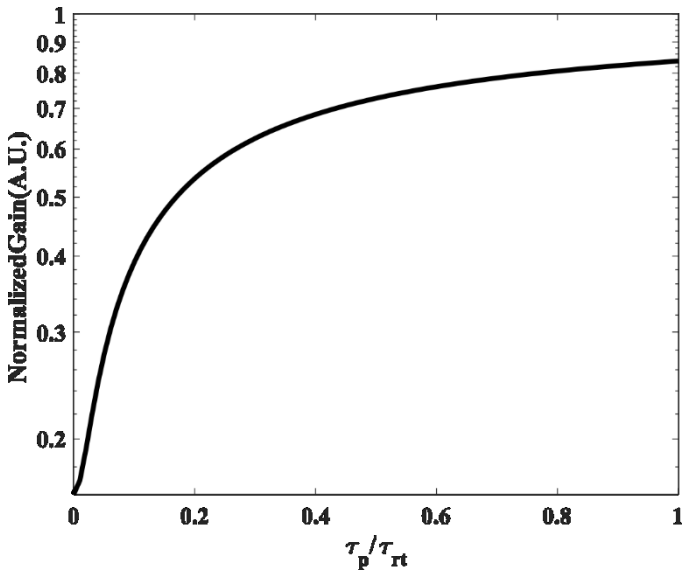

Figure 3- 4. Normalized averaged gain experience by a pulse versus the pulse length normalized to the cavity roundtrip time.

Obviously, for a fast saturable gain ($\Gamma << 1$), the longer the pulse the more efficient the laser. And thus we do not expect the amplitude modulation as shown in Fig 5a and b [,] to be a pulse. The large amplitude modulation present in ramp FM QCls always coincides with the extremely rapid phase shift that occurs after the ramp signal has completed its span and must return to its original frequency. Amplitude and phase are coupled in the semiconductor medium, so a very sharp change of phase can cause a change in amplitude. Another possible cause is dispersion of the medium. This is not to say that some amplitude modulation can be

present in the device, and may actually help to lower spatial hole burning as will be discussed next.

Sinusoidal Amplitude Modulation

Now, as mentioned previously, there have been frequency comb generating QCLs reported that show significant amplitude modulation in addition to frequency modulation. In an attempt to explain this, we calculate the power variance of a signal with deterministic, sinusoidal amplitude modulation

$$E(z,t)=\frac{E_0}{2}\exp(-j\omega_0 t)\begin{Bmatrix}\cos[\omega_m(t+\Delta t/2)]\exp[-j\omega_0\Delta t/2]\\ +\cos[\omega_m(t-\Delta t/2)]\exp[+j\omega_0\Delta t/2]\end{Bmatrix}+c.c. \qquad (3.11)$$

Squaring the electric field and taking the variance we see that $\sigma^2=\frac{1}{T_m}\int\sigma^2(\Delta t)d\Delta t=\frac{3}{16}$.

Unaveraged power variance in fact increases, effectively making spatial HB worse for oscillations slower than the gain recovery time. However, we can see that if averaged by the oscillation period, under the condition that the oscillation frequency is commensurate with the gain recovery time, the averaged power variance is halved which surprisingly leads to a variance lower than that of pure FM (for low modulation index).

$$\sigma^2=\left\langle\frac{1}{4}\cos^2(\omega_m\Delta t)\cos^2(\omega_0\Delta t)\right\rangle_{\Delta t}=\frac{1}{16}$$

In some cases, indeed amplitude modulation can help to improve spatial HB as long as the oscillations are rapid enough to be averaged by the active medium. Amplitude modulation can be especially helpful when the frequency modulation undergone by the QCL is effectively at

a low modulation index (β), as FM alone can beat out AM at higher modulation index. Further derivation of signals with both AM and FM were performed, however quickly became far too complicated. It is apparent, however, that the functions controlling the standard deviation are multiplicative and thus mitigation of spatial HB from AM and FM will act as such, in other words if the variance is high for the FM portion of the signal but low for the AM portion, the overall variance will be lowered by the amplitude modulation.

Ramp Frequency Modulation

As mentioned before, with the inception of SWIFTs, unprecedented access to the time domain profile of the FC emission revealed a linear frequency chirp or "ramp FM QCL". This behavior has now been confirmed by multiple research groups. Here we choose two prominent results to perform our analysis [40, 55], the time domain profiles of which are shown below in Figure 3- 5.

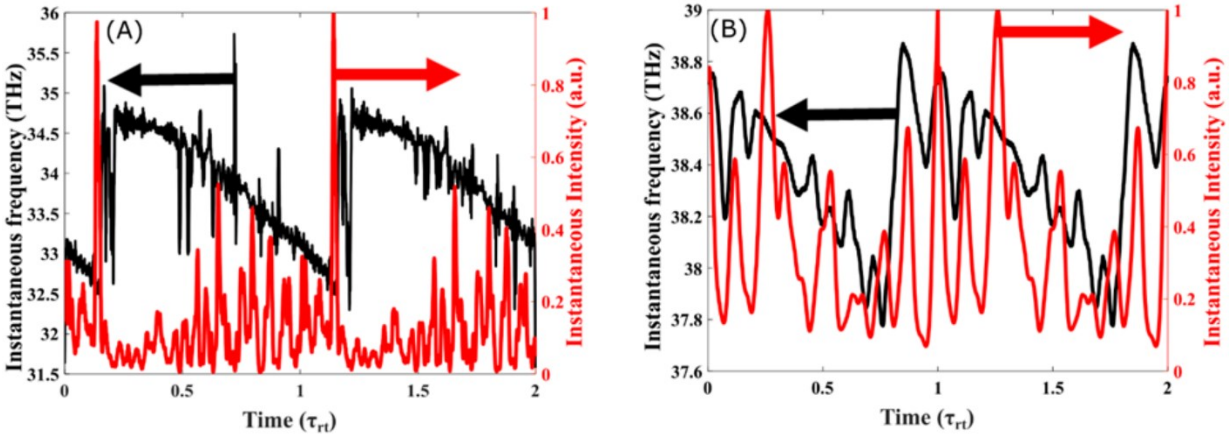

Figure 3- 5. Time domain profile measurements from the emission of a FC QCL as published in [40] (A) and [55] (B).

As we have seen, a linear frequency chirp in experiment, it is also useful to calculate the variance of the ramp FM signal versus the span of frequency. As before we start off with two

counter-propagating electric fields, however we now include a parabolic phase (the derivative of which is our ramp FM signal).

$$E(z) = \frac{E_0}{2}\exp\left(-j\omega_0(t+\Delta t/2) - j\frac{A}{2}(t+\Delta t/2)^2\right) + \frac{E_0}{2}\exp\left(-j\omega_0(t-\Delta t/2) - j\frac{A}{2}(t-\Delta t/2)^2]\right). \quad (3.12)$$

Resulting in an intensity of $|E(t)|^2 = \cos^2(\Delta t/2(At+\omega 0))$. Now we can calculate the power variance as

$$\delta S(z,t) = S - \langle S\rangle_{z,t} = |E(t,z)|^2 - \frac{1}{2} = \frac{1}{2}\cos\left[At\Delta t + \omega_0\Delta t\right] \quad (3.13)$$

with $A = \Delta\omega/\tau_{rt}$. The power variance is $\langle \delta S^2\rangle_{t,\Delta t}$ where time $t \in [-\infty, +\infty]$ and delay $\Delta t \in [0, \tau_{rt}]$. So, let us introduce the normalized variables, namely position along the cavity

$$z = \frac{\Delta t}{\tau_{rt}};\ z \in [0,1]$$

and, in anticipation of future,

$$\tau = \frac{t}{\tau_{21}};\ \tau \in [-\infty, \infty] \quad .$$

thus we get

$$\delta S(z,\tau) = \frac{1}{2}\cos\left[\Delta\omega\tau_{21}\tau z + \omega_0\tau_{rt}z\right] = \frac{1}{2}\cos\left[K\tau z + Lz\right] \quad (3.14)$$

where the "FM strength" is $K = \Delta\omega\tau_{21}$ and the normalized length is $L = \omega_0\tau_{rt}$ which is quite large so the cosine will oscillate very fast producing many standing waves. Next we need to average the intensity over the upper level lifetime, or

$$\delta\bar{S}(z,\tau)=\int_{-\infty}^{\tau}\delta S(z,\tau_1)e^{\tau_1-\tau}d\tau_1=\frac{1}{2}\int_{-\infty}^{\tau}\cos\left[K\tau z+Lz\right]e^{\tau_1-\tau}d\tau_1=$$
$$\frac{1}{2}\frac{\cos\left(K\tau z+Lz-\varphi\right)}{\sqrt{(Kz)^2+1}} \quad (3.15)$$

where $\varphi=\arctan(Kz)$. Calculating the power variance

$$\sigma^2=\left\langle\delta\bar{S}^2\right\rangle_{z,\tau}=\frac{1}{8}\left\langle\frac{1}{\left(Kz\right)^2+1}\right\rangle_{z=0..1}=\frac{1}{8}\frac{\arctan(K)}{K}\ ,(3.16)$$

the graph of which is shown below. There is a subtle difference between the variance of the two scenarios (sinusoidal FM (Figure 3-3) and frequency chirp (Fig 3-6)) namely that in the sinusoidal scenario the oscillation must be faster than the upper level lifetime as the averaging is implicitly over the period of frequency modulation. Additionally FM oscillations with a frequency faster than the averaging time (τ_{21}) will not help to improve the power variance and slower oscillations may degrade variance. With a linear frequency chirp scenario, the longer the upper state lifetime, the better the performance, regardless of the implicit period of the waveform. Thus, even though the frequency chirp looks to perform slightly worse than the sinusoidal FM, with the right specifications a frequency chirp could outperform the sinusoidal version as well.

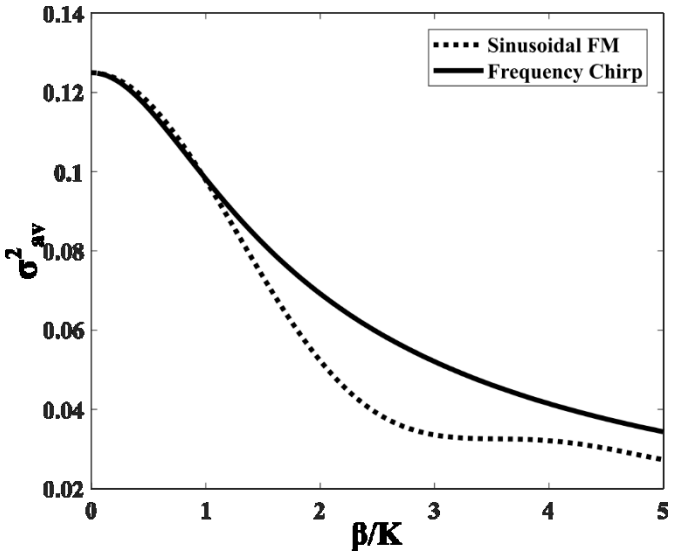

Figure 3- 6. Averaged power variance versus modulation index or K for a frequency chirp with a period equal to the cavity time.

Variance Results Compilation

It is now useful to add randomization to our sinusoidal AM signal calculations, in an attempt to further lower the variance. Figure 3-7 below presents the variance for different combinations of deterministic or random sinusoidal modulation (amplitude/frequency). Additionally, variance measurements were performed on data presented in [40] and [55], showing that the spatial HB is in fact mitigated in both, with [40] being slightly better, possibly from the faster AM. This could however be an artifact arising from the separate noise cancellation methods utilized in the data. When considering the frequency modulation index of both [40] and [55] we see that they span a peak frequency deviation of $\beta = A_m / f_{FM} \approx 2THz / 10\,\mathrm{GHz} = 200$, with this high of a modulation index it is easy to see why spatial HB may not be a problem in this scenario. This calculation of modulation index is under the assumption that the fastest frequency in the FM signal is $1/\tau_{rt}$, which is most likely not accurate, thus modulation index is most likely lower than 200. Considering the randomized AM and FM data, we must note that, unlike the

derivation described earlier, the amplitude modulation is a sinusoid added to a CW wave, so that the average of the electric field is $1/\sqrt{(2)}$ rather than zero and the modulation span $A_{AM} = 0.75$. As these are randomized we can no longer calculate the variance analytically, however we are able to show that indeed further randomization of the frequency modulation signal indeed lowers spatial HB. We also show, in Figure 3-7b, the variance measurements for a simulated frequency chirp, both with and without a pulse, as well as experimental data. Indeed the data presented here greatly resembles the analytical solution presented in Figure 3-6. As can be seen in Figure 3-7b the experimental data from [40, 55], referred to as Sdata and Bdata in the figure, lies between a chirped pulse and a chirped frequency without a pulse.

Calculating the power variance with data from both references put them right on the graph at around 0.04, while conversely a chirped pulse results in a variance of >0.1. Therefore, a high frequency modulation index is critical to lowering variance with FM in the case of sinusoidal modulation and a high upperstate lifetime and wide bandwidth are critical to lowering variance with a chirped frequency modulation. Fast amplitude modulation does indeed decrease the average variance as long as it is faster than the gain recovery time. When both AM and FM are present the derivation shows to be multiplicative, thus the dominate effects depend on the modulation index and it is possible for the amplitude modulation to compensate for peaks due to instant frequency matching in the cavity.

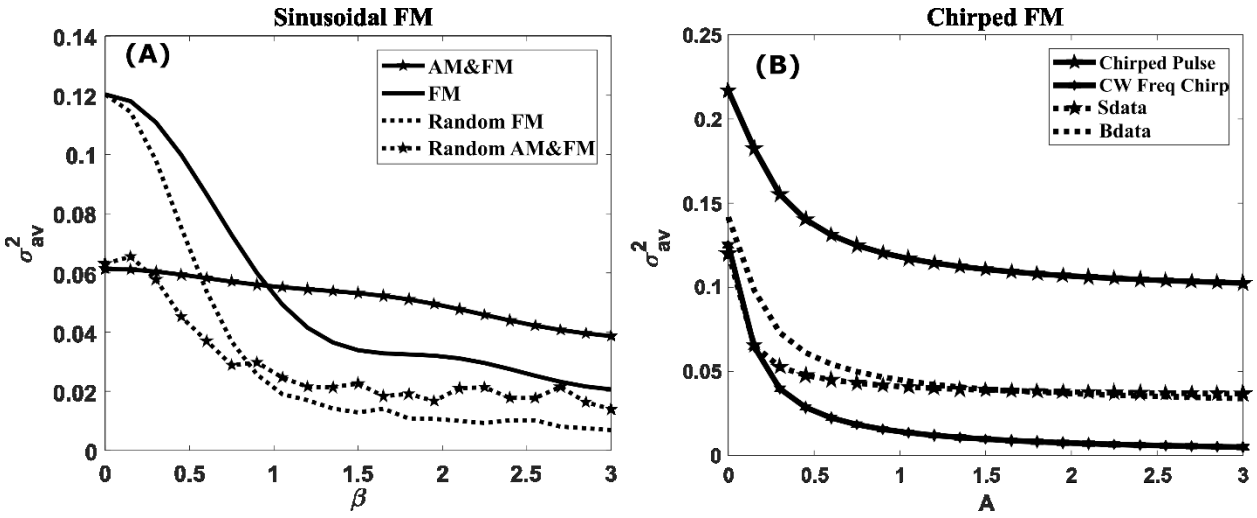

Figure 3- 7. A) Averaged variance measurements of various sinusoidal FM signals. B) Averaged variance measurements of various linearly chirped FM signals. Sdata refers to reference [40] and Bdata refers to reference [55].

Conclusion

In this chapter we have introduced a standard by which to measure the effective spatial hole burning of the system under various FM/AM waveforms. We calculate the standard deviation of the averaged intracavity intensity for various operational scenarios and analyze its effect on variance and introduce a conceptual analysis on what happens to the saturated gain under single mode and various multi-mode situations. We elucidate key factors affecting the efficiency of the laser to be factors such as the upperstate lifetime, the gain bandwidth, and the modulation index. We then postulate on the surprising results that seem to contradict [40, 55] by investigating these waveforms and conclude that indeed under certain conditions it is possible that a ramp FM QCL is the most efficient regime. Factors concerning these conditions and the resulting operation regime will be further discussed. Furthermore, we present compelling evidence that a circulating pulse inside the cavity is highly unlikely due to many

reasons. We attribute the pulse like amplitude modulation to the relation between amplitude and phase in the system, when the FM jumps very rapidly from one side of the gain spectrum to the other, this fast phase change will of course result in a modulation of amplitude. This is apparent as the pulse is always formed at the same time as this rapid phase shift.

Chapter 4: Analysis of Operational QCL

As of this point the time domain model has been fully developed to include all forms of hole burning, spectral, spatial and temporal. We have eased our calculation load by converting a customized optical Bloch equation into a simple rate equation that includes time dependent detuning. This approximation assumes that the time rate of change is slower than the internal loss of coherence and proved to follow the fully coherent equations quite well. We are now ready to test various operational scenarios and observe the outcome and the QCLs efficiency by tracking the gain and non-radiative, relaxation current. These two properties were derived earlier in Chapter 2 but we will reiterate them here.

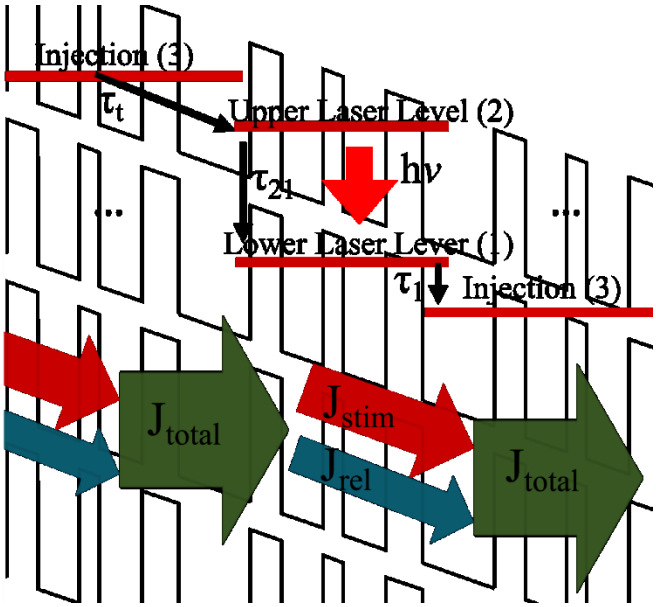

Figure 4- 1. Drawing of levels in one period of QCL with all the relevant times, and dissection of current, recycled through the periodic structure.

As shown in Figure 4-1 above, each period of the QCL experiences a current density injected onto the ULL which then splits into two current densities – one $J_{stim} \sim \gamma(z,t)I(z,t)$ is the

current associated with the stimulated emission and the other J_{rel} is associated with mostly nonradiative relaxation of the ULL, see Figure 4-1. Therefore, the "maximum emission regime" with the lowest threshold occurs when the stimulated current flowing through the entire laser structure is maximized and the averaged gain experienced by the photons reaches a maximum

$$\overline{\gamma} = \frac{\left\langle I(z,t)\gamma(z,t)\right\rangle_{z,t}}{\left\langle I(z,t)\right\rangle_{z,t}}. \tag{4.1}$$

Where

$$\gamma(z,t) = \Gamma\sum_{n} f^{(n)} \frac{4\pi\alpha_0}{n_{eff}} \frac{N_D}{W} \frac{{z_{21}}^2 \omega_o \tau_{coh} {N_{21}}^{(n)}(z,t)}{1+\tau_{coh}^2 \Delta\omega^{(n)}(t)^2}, \tag{4.2}$$

W being the effective thickness of one active period, and n_{eff} the effective index is approximately equal to the material index, values of these various parameters are listed in Table 1 later in the chapter. We can also keep track of the nonradiative relaxation current. Obviously these two parameters should act as the mirror image of each other, i.e. a peak in the gain should be a dip in the relaxation current which is defined as

$$\overline{J}_{rel} = \left\langle qN_D\tau_2^{-1}\sum_n f_n {N_2}^{(n)}(z,t)\right\rangle_{z,t}. \tag{4.3}$$

We now have the tools to investigate various operation scenarios to the time-domain model, which has been built to resemble the properties of a real world LWIR and THz QCLs by inhomogeneously broadening the gain bandwidth and introducing generally accepted specifications. We can now see how these calculations can become time consuming, especially for LWIR devices due to a much shorter wavelength than THz. For the LWIR model the number of spatial intervals $\Delta z \sim \lambda/10$ at which the spatial shape of the intensity must be calculated

exceeds 7000. Additionally, the number of temporal intervals $\Delta t \sim \tau_2 / 10$ required to adequately describe the FM shape is 2000 and the number of spectral bins needed to faithfully reproduce the gain shape is 80. Thus, each 7000 x 2000 x 80 array corresponds to just one data point in the results shown below.

The results presented in the subsequent graphs are generated using common specifications for QCLs in the LWIR and THz regimes respectively. Both devices are modeled to be 2mm long, shorter than typical devices, however proven to be long enough to illustrate properly all the trends described below. Specifications, given in Table 1, were obtained from the references [4, 12, 48-50, 56-62].

f_0	Current Density	N_{2D} / W	τ_{coh}	τ_2	τ_1	z_{21}	Intra-cavity Power	Psat	Cross-section	Gain FWHM
$3THz$	$800A/cm^2$	$3.5x10^{10}cm^{-2}/57nm$	$0.7ps$	$4ps$	$1.5ps$	$4.7nm$	$50mW$	$94.5mW$	$10\mu m$ x $25\mu m$	$2.2THz$
$30THz$	$6.4kA/cm^2$	$4x5x10^{10}cm^{-2}/68nm^*$	$0.2ps$	$0.4ps$	$0.3ps$	$2.2nm$	$250mW$	$3.4W$	$6\mu m$ X $15\mu m$	$8THz$

Table 4- 1. Laser specifications. *The QCL laser simulated contains four 5x1010 cm-2, delta doped layers per period.

For the terahertz frequency comb we attempted to closely match the specifications of the laser to that which is presented in [4]. This comb was manufactured with a dispersion compensation scheme shown in Figure 4-2a below, essentially pinching off short wave light towards one side of the cavity thus altering its effective cavity round trip time. In Figure 4-2b we see the spectrum as measured by two methods involving the interferometric measurement of a fast hot electron bolometer (HEB). Spectroscopy involving a mechanical delay element simply does not have the accuracy to measure these frequency combs (>1GHz). Shown in the spectrum is

two lobes which are a result of the double peaked gain shape caused by the strong injector anti-crossing. Results showed very weak interaction between the two regions, this behavior was not included in the time domain model.

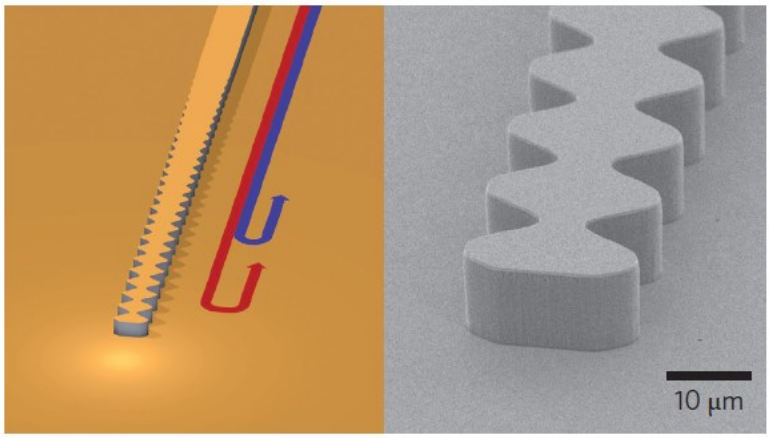

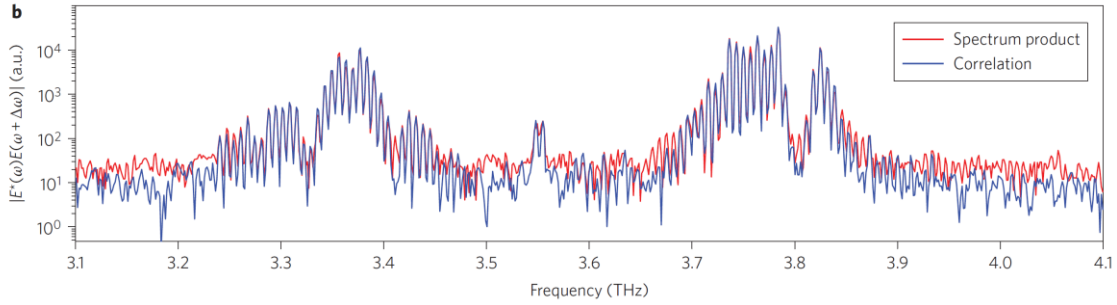

Figure 4- 2 A. Diagram of the dispersion scheme for the THz QCL on which this work was modeled. This shows how the shorter wavelengths travel less distance round trip. B. “Blue line: SWIFT correlation spectrum (calculated from homodyne interferograms). Red line: spectrum product (calculated from normal interferogram). Even though they are fundamentally different measurements, their excellent agreement indicates that most of the spectral power is in the frequency comb.” - [4]

In regards to the long wave QCL, specifications were found from various sources yet the differences between LWIR and THz will be ubiquitous for most designs. Much crucial information was collected from [60], which presents a very thorough analysis of a QCL emitting

at 8.6 μm and involving a 5 quantum well single phonon-continuum depopulation scheme, the bandstructure of which is shown in Figure 4-3.

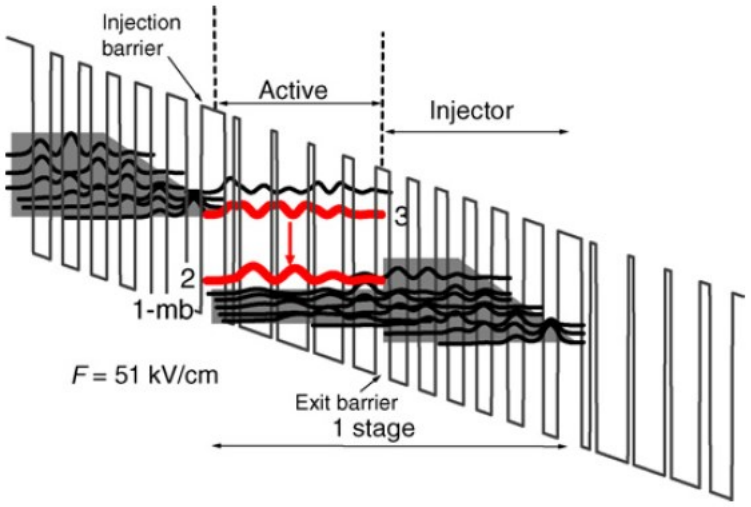

Figure 4- 3. Conduction band diagram and relevant wavefunctions of the injector and active regions, illustrating 5-well design and depopulation scheme. The designed wavelength is around 8.5μm at room temperature.[60]

While there are some similarities in the properties of the two lasers, there are a few glaring differences. As a result of the much lower upperstate lifetime, the current density needed for the long wave laser is much higher. The upperstate lifetime must be engineered to be longer in the terahertz laser because of the extremely small amount of energy involved in the transition. Thus, in order to not inject directly into the lower level and lower non radiative emission the laser transition is diagonalized spatially, thus lowering the probability of transition (Fermi's golden rule) and increasing the lifetime. Considering the difference in saturation power, this is because of a large dipole moment for the THz lasers and the very small transition energy, $\hbar$.

Pseudo-random frequency result

The first results presented in this dissertation (chapter 2) were for deterministic, sinusoidal frequency modulation. After a lengthy discussion on the importance of spatial hole burning and the characteristic outcomes defined by the waveform of the frequency modulation, it is now useful to input our various forms of FM, starting with our pseudo-random signal as defined and shown in Figure 4-4 below.

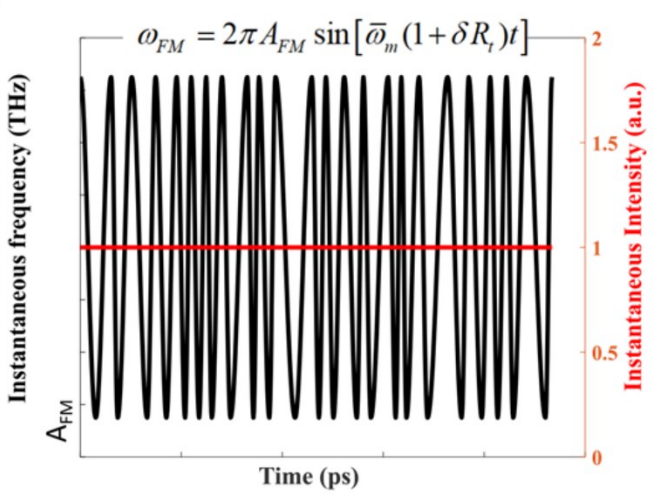

Figure 4- 4. Example of a pseudo-random frequency modulation signal and its constant intensity. Included is equation (3.8) which is the governing equation for the pseudo random FM signal.

We then run the program while spanning, A_{FM}, the FM signal to a larger bandwidth as well as increasing our measure of randomness, δ . The results shown are exactly as expected, yet again the laser acts in its most efficient regime when the FM signal spans the entire bandwidth of the laser. As predicted earlier, an increase in randomness decreases the peaks and troughs spatially present in the laser cavity and maximizes emission. The results are shown below in Figure 4-5, giving fairly accurate numbers for averaged gain and relaxation current as seen in experiment.

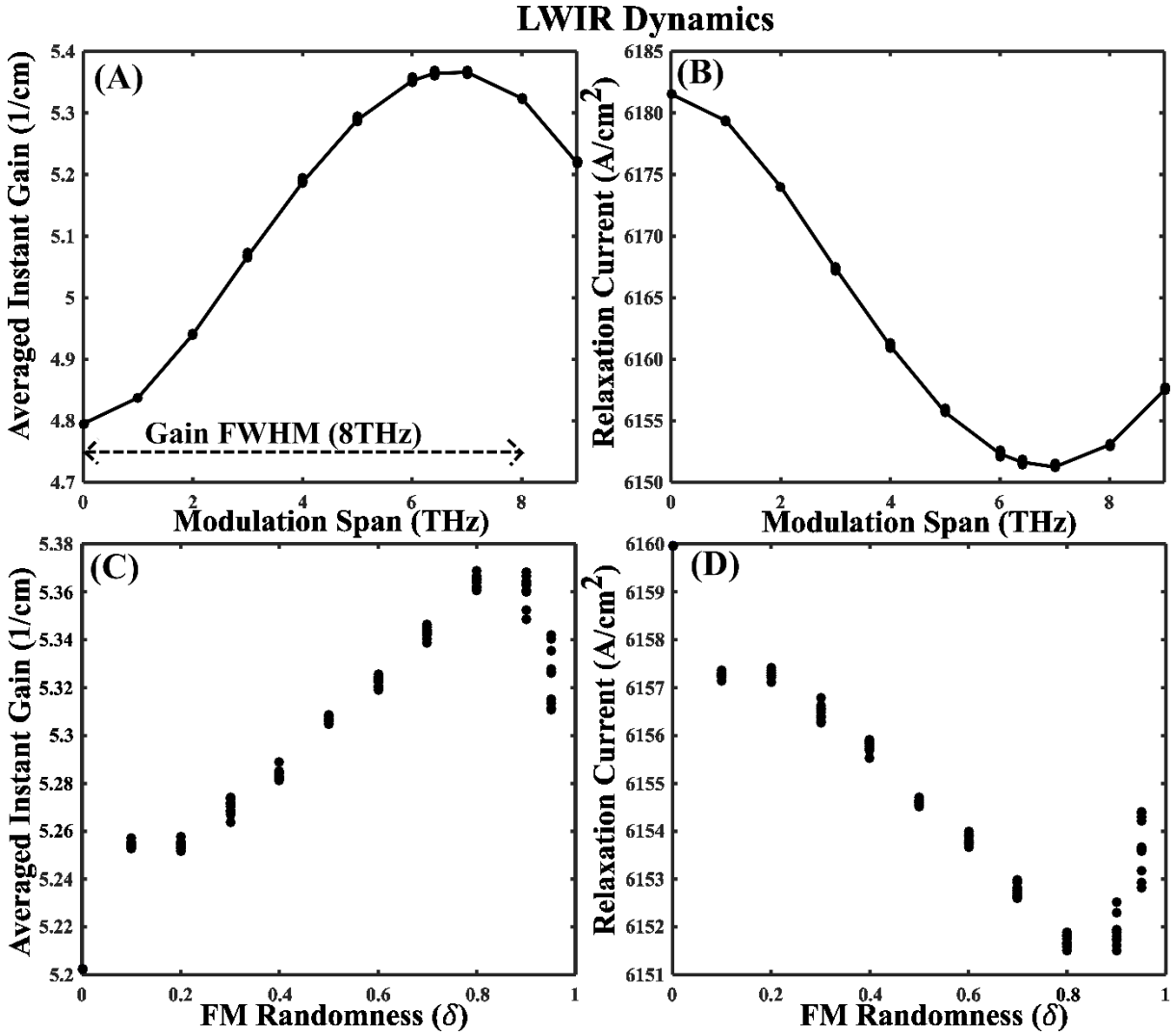

Figure 4- 5. Averaged instant gain (a and c) and relaxation current (b and d) versus frequency modulation span and randomness (δ) for an LWIR QCL.

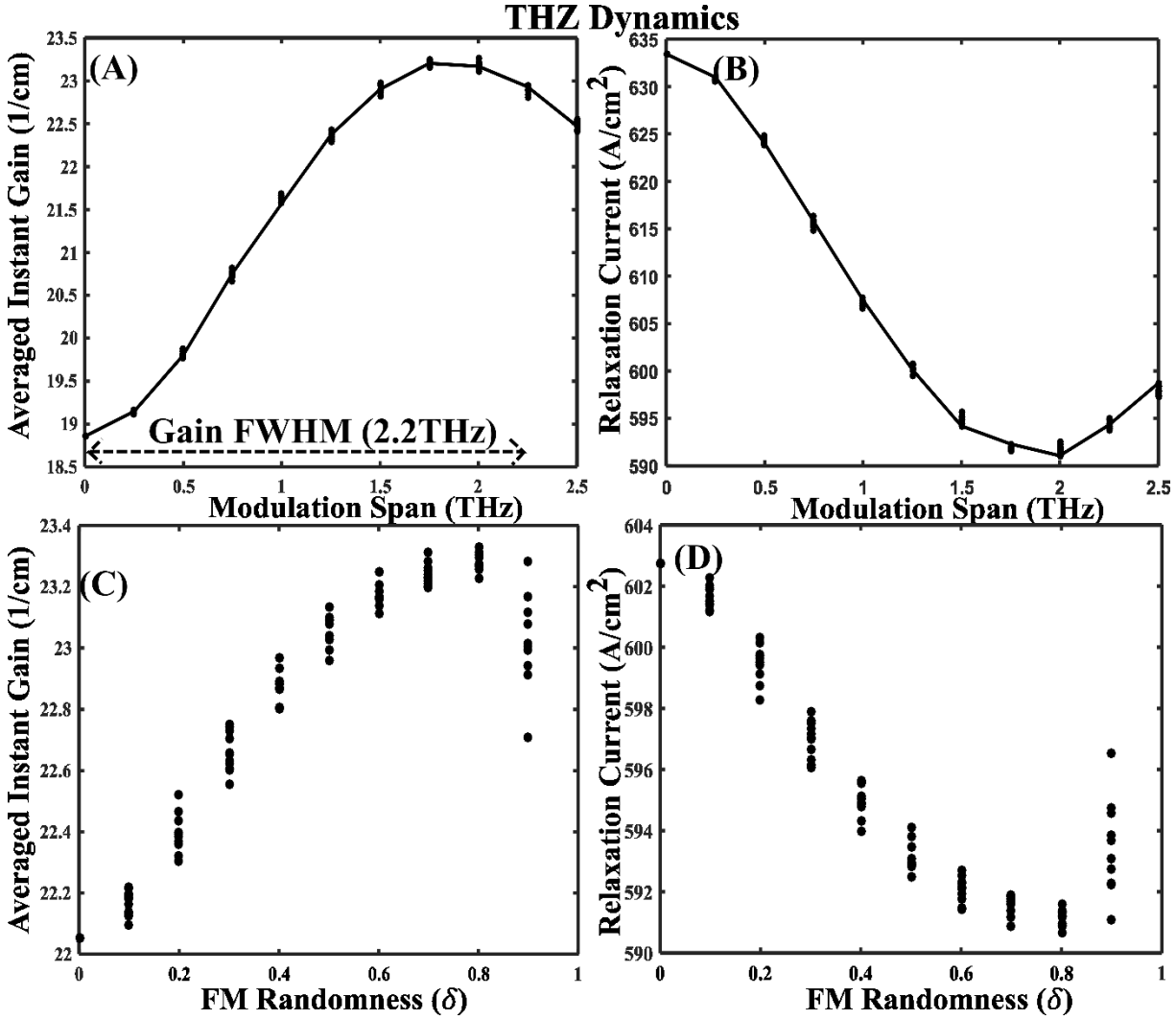

Figure 4- 6. Averaged instant gain (a,c) and relaxation current (b,d) versus frequency modulation span and randomness (δ) for a THz QCL.

The graphs showing effective gain $\bar{\gamma}$ and nonradiative current density $\bar{J}_{rel}$ vs modulation span $(2A_{FM})$ have been produced using the optimum value of $\delta = 0.8$. QCL graphs with randomness for the x-axis are produced using the optimum modulation span, 6.2THz for LWIR and 1.8 THz for THz QCLs. As expected, both δ and A_{FM} reach their optimum values and the average gain

experienced by photons increases and stimulated emission leaves fewer carriers to experience non-radiative relaxation to the LLL, confirming that the laser has reached optimum efficiency.

The key result that can be inferred from Figs 3 and 4 is the importance of randomness and therefore the suppression of spatial hole burning. As we mentioned above, non-random FM ($\delta = 0$) goes a long way to decrease spatial hole burning when compared to a single frequency scenario, however, there still exist $m = \tau_{rt} / T_{FM}$ locations in the cavity where the modal frequencies between the two counter-propagating waves match creating peaks and troughs in the gain. By introducing randomness into the FM signal, the stationary standing wave pattern is suppressed as the two waves no longer meet with similar frequencies, or at the least it does not last very long and the gain does not see the instant intensity but rather the average over the upper state lifetime, this scenario does not cause spatial holes. Of course, when δ approaches unity the change of instant frequency can become too slow (in comparison to τ_2) causing the appearance of spectral holes, hence the optimum value of δ is always less than unity. The shape of the spatial hole burning depends heavily on the modulation index, in our case A_{FM} / ω_{FM} . Thus, while an optimum FM signal must span close to the entire spectral gain at a rate of $1/\tau_2$, the fact that the spatial distribution depends heavily on the ratio between the two will broaden the set of possible FM signal solutions. This further confirms our inference that there exists an infinite number of solutions for the laser's FM signal. Even more so if we allow that the speed at which the FM signal spans the bandwidth does not have to be as fast as stated before and can actually be simply equal to the round trip time.

Real World Experimental Results

As has been explained in Chapter 3, there seems to be some evidence that the ramp FM signal mixed with some form of amplitude modulation may prove to be a superior and more efficient regime of operation for the QCL. Thus, we wish to characterize the efficiency of a spectrally broadened QCL with time domain profiles obtained from SWIFTS measurements by [55] and [40], see Figure 4, and compare. Due to the amplitude modulation present in experimental signals, both [55] and [40] produce gain values significantly lower than those present with pseudo-random sinusoidal FM signals. This is shown by the data labeled “Frq Chirp No AM” in Figure 4-7, the lack of AM means the same instant gain with a zero frequency span, however as the modulation span increases the time domain model experiences significant spectral HB and the averaged gain is not maximized. Not only does the amplitude modulation seem to lower the averaged gain experienced but spectral HB has also increased due to the slow nature of the instantaneous frequency. This leads us to conclude that if the QCL does not suffer significantly from spectral HB, the frequency chirp may lead to a lower level a spatial HB and be the dominate operation regime. Conversely, a chirped pulse given to the spectrally broadened TD model results in a very low averaged instant gain of 3.65 cm^{-1}, coinciding with our previous analysis.

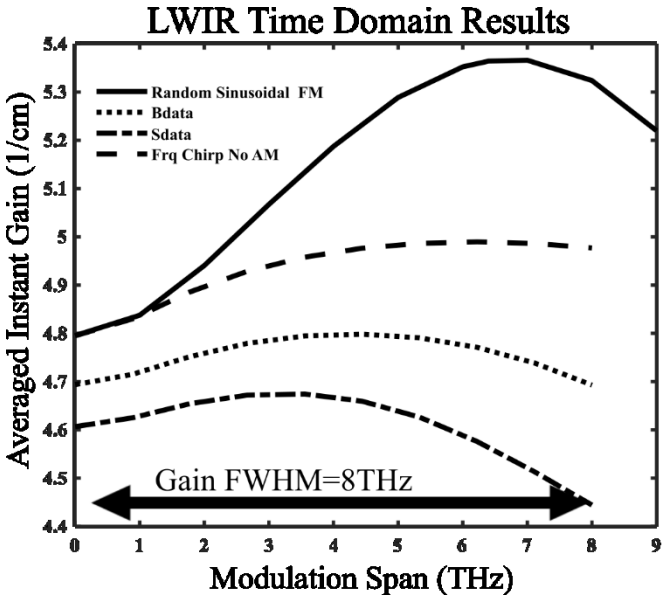

Figure 4- 7. The effective gain $\bar{\gamma}$ vs modulation span results from the TD model for sinusoidal FM, experimental FM, and a frequency chirp. Sdata refers to reference [40] and Bdata refers to reference [55].

Discussion

There are two major points of interest presented in this chapter. The first point of interest is the comparison of an ideal pseudo-random operational scenario for a highly broadened QCL suffering from spectral hole burning and the experimentally measured data showing a ramp frequency modulation. This first comparison will be discussed further in the next chapter. The second point of interest is the comparison between a THz and a LWIR laser. We can confidently postulate that spatial hole burning in THz lasers may have a larger effect due to the higher mirror reflectivity. However, the modulation index will also effect the spatial hole burning in both lasers. For a THz laser the FM signal will span a much smaller bandwidth yet, consequently, with a much faster period. Thus any increase in spatial hole burning from a higher mirror reflectivity is counterbalanced by the modulation index.

Thus, both THz and LWIR show very similar trends. Comparing averaged instant gain values between no frequency modulation and an optimum, pseudo-random FM regime, the LWIR experienced an increase of 0.6 cm^{-1} while the THz laser improved by 4 cm^{-1}. This disparity in improvement is easily reconciled by finding the percentage of improvement relative to the unsaturated gain, in this case both lasers have improved by 8%, a small percentage yet enough to influence the laser's operation. It is of note that a larger improvement is in fact seen under full OBE modeling [47] suggesting that we could be slightly underestimating the gain increase. Regarding the drop in relaxation current for both lasers, we can calculate the decrease in wasted carriers and thus the direct increase in photons. Namely, the QCL experiences an increase in photons of $7x10^7$ cm^{-2} for LWIR and $1.1x10^9$ cm^{-2} for the THz laser, note we do not include loss other than through the mirrors. It should also be noted that the data point taken to be the most inefficient, and thus the data used as the base for comparison, might not be completely physical in the sense that this regime of operation, namely multi-mode with no FM or AM, would not occur. In fact, without FM the multi-mode laser would certainly exhibit amplitude modulation.

We can therefore conclude that, given the data produced by our model, frequency comb operation is very similar for both LWIR and THz lasers. While there are in fact many differences, the underlying principles of the two lasers (which are the causing factors of the strange QCL operation) remain and thus they possess very similar properties. More experiments can be conducted to prove this, such as placing the laser in a ring cavity and thus removing any possibility of spatial hole burning. This experiment has actually been performed and resulted in

a very narrow comb formation, with a questionable temporal profile. This obviously shows how crucial spatial hole burning is to multimode formation [63].

A study of QCL operational regimes

Throughout the author's study of the free running, frequency comb generating, QCL, it has become plainly obvious that there are an infinite number of possible regimes in which the QCL can operate. As mentioned previously, the natural regime of operation will be that which possesses the lowest threshold and thus is the most efficient, i.e. the regime achieving maximum emission. The determination of this lowest threshold has been the study of this work thus far. It has become apparent that external perturbations and the design of the QCL determines how it will behave. Many fingers have been pointed in an attempt to elucidate factors contributing to the QCL's operational characteristics such as asymmetric gain, spatial hole burning, group velocity dispersion, coherent tunneling, etc. There is a strong push to mold the QCL into a passively locked, pulsed comb (while this has been achieved actively [64-66] the resulting combs are far from optimal) in order to achieve a broad and stable comb yet the simplest analysis of the QCL, as a result its short upper-state lifetime, tells us that pulses in the laser will not maintain. Therefore, it is the author's belief that the best course of action is to pursue a purely frequency modulated QCL with extremely efficient mode coupling, this way the bandwidth is limited by Carson's rule, which, given control over the characteristics of the laser, will supply us with more knobs to turn.

The Influence of Spectral Hole Burning

Because the averaged gain for a slow FM QCL is so much lower than that for a fast FM QCL, as shown earlier, it is reasonable to conclude that the spectral hole burning does not play a significant role in the experimentally tested QCLs. This appears a bit counterintuitive, especially for lasers with two different active periods, and requires extremely short intra-subband scattering times on the scale of 100fs or even less for broad band lasers, but the presence of spectral hole burning was never confirmed by literature. Therefore, we have studied the influence of inhomogenous broadening on the preferred operating regime. As shown in Figure 4-, a chirped FM regime is superior to the pseudo-random regime when the total bandwidth ΔB_{TOT} is close the homogenous bandwidth $\Delta B_H = 1/2\pi\tau_{coh}$. We evaluate the values of the averaged gain experienced by photons for the chirped $\overline{\gamma}_{ch}$ and pseudo-random FM $\overline{\gamma}_{pr}$ cases (for the same average laser power) and then plot the relative difference between them in percentage points $\Delta\overline{\gamma} = (\overline{\gamma}_{ch} - \overline{\gamma}_{pr}) / \overline{\gamma}_{pr} \times 100\%$, the y-axis of Figure 4-8. It can be seen that as long as the amount of inhomogeneous broadening is insignificant, the chirped, slow FM appears to be the most favorable regime of QCL operation, but once inhomogeneous broadening increases the spectral hole burning reduces the gain for the chirped regime and the pseudo-random, fast FM becomes preferred. While this difference is only a few percent, this small difference in efficiency is sufficient to make the linear chirp a preferred operating regime. This leads us to conclude that if the QCL does not suffer significantly from spectral HB, the frequency chirp may lead to a lower level of spatial HB and be dominate.

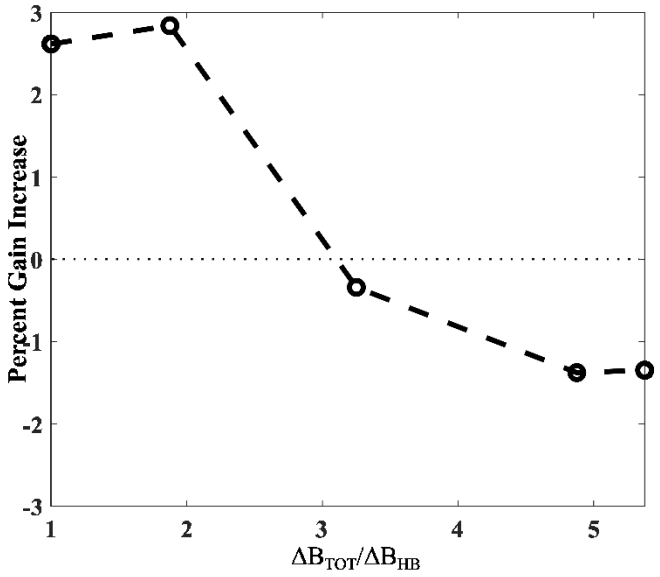

Figure 4- 8. Percent increase of the gain vs inhomogeneous broadening using a chirped FM as compared to a pseudorandom, faster FM.

As mentioned above, absence of spectral HB in a broad gain QCL has not been fully explained yet. One can argue that if the inhomogeneous broadening is caused by variation of the active region thicknesses (whether intentional, as in a two-active region QCLs, or not) the fact that the same current flows through the different active regions may prevent spectral hole formation. Whether the current is continuous on sub-picosecond scale (i.e. there is no fluctuating charge build-up in the injector) needs to be studied. It is more difficult to explain what prevents spectral hole formation if the active regions are non-uniform in the plane of growth, and the only reasonable assumption is then that when the growth is of sufficiently high quality that this non-uniformity is avoided. However, the experimental data supported now by our TD model strongly indicates that spectral hole burning appears not to be a defining factor and it is precisely this fact that makes a chirped FM the lowest threshold operating regime for a free running QCL.

Frequency Chirp Stability in the Frequency Domain Mode

The above TD results indicate that linear chirp is indeed a viable operating mode given very little spatial hole burning, but it is not clear how stable it is. To study this we go back to the FD model and introduce initial conditions where the amplitudes and phases are similar to [40], i.e. quadratic in time and broadband modes. We then run the model with chirped initial conditions under the presence of noise and see that indeed this mode of operation is stable. This stability is manifested by the FD model maintaining ramp-like instantaneous frequency after many iterations and further strengthened by the instability of a pulsed initial condition.

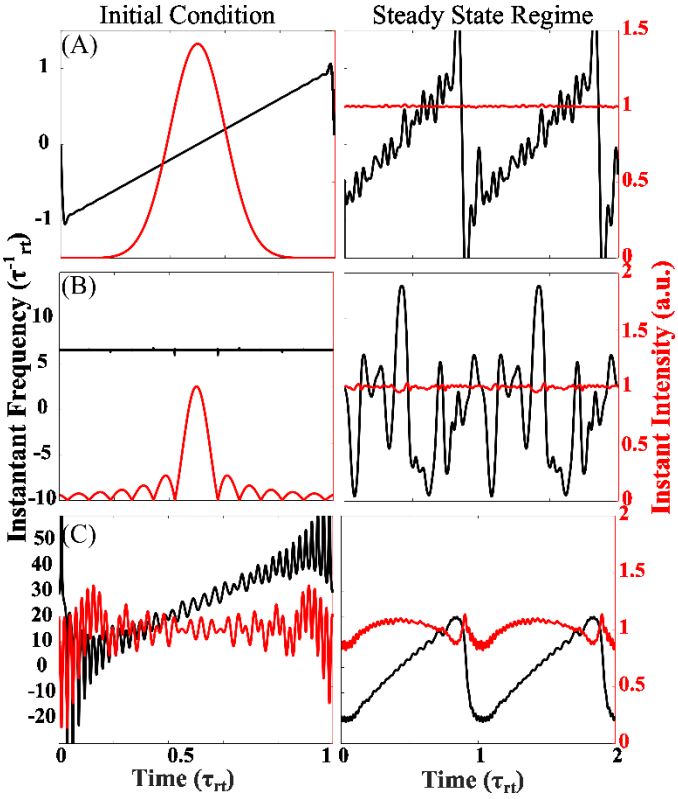

Figure 4- 9. Initial conditions and FD model results of three scenarios: A) Pulse waveform with equal phases. B) A broadband chirped FM waveform with quadratic phase relation. C) A Chirped pulse that is narrowband.

Three scenarios, shown in Figure 4-9, have been tested for stability in a fast saturatable gain. The first being a pulse with frequency chirp, the second equally phased modes (i.e. short pulse), and the third a broadband frequency chirp. As can be seen by comparing the first column (initial conditions) to the second (steady state regime), the FD model favors smooth CW radiation, regardless of the initial condition. In the first row, a chirped pulse was given to the FD model which retains its frequency chirp, although with a very narrow band, and smooths the pulse amplitude to be CW. In the second row a pulse is rapidly smoothed into CW radiation as predicted by [5]. However, introduction of a wideband, frequency chirped signal obviously shows stability in the phase relations between the modes, as shown in row 3. Interestingly, the data produced from the FD for a frequency chirp introduces residual AM that is correlated with the instantaneous frequency, much like what is seen in experiment (Figure 3c), namely a spike in the intensity as the frequency undergoes a rapid negative slope. Thus, according to the FD model, while a short pulse (strong AM) is not stable and will always be smoothed, a long pulse or weak AM and a linear frequency chirp is. In the presence of some external influence forcing the initial phase relation between modes to be quadratic in addition to very little spectral HB, a stable, linear frequency chirp emerges as a stable regime. It should be noted that while the FC is by no means perfectly periodic, the periodicity is good enough for spectroscopy. For more discussion on the noise involved in QCL FC refer to [42]

Presence of Amplitude Modulation

The above work still does not explain the presence of amplitude modulation seen in the ramp FM QCLs. While the frequency domain model did show some connection between the rapid movement of the instant frequency and a spike in intensity, it does not quite match what has

been seen in experiment. It is well known that there is an amplitude and phase coupling in the semiconductor medium [42]. Furthermore, while the SWIFTs technique is very robust, it is still a fairly new innovation and there is a possibility that the peak in amplitude is an artifact. The rapid change of frequency at the end of the frequency chirp is somewhat non-physical, this fast of a change in frequency would never be seen by the two laser levels. Therefore, it is possible that this is present in order to force periodicity. Often the simplest explanation is the answer, the gain medium of the QCL is the exact opposite of a saturable absorber which stores energy for a pulse. In this case a pulse in the QCL is not stable as shown in the work above.

Some affirming work has just been released measuring the FC emission from a ring cavity QCL [63]. This is important work in that, with a ring geometry the light will, hopefully, travel in one direction and thus eliminate spatial hole burning. This work reports that there is no longer a quadratic phase relationship, as is seen for a ramp FM QCL. In the absence of spatial hole burning the superiority of the chirped or ramp FM signal is no longer applicable and a different operational regime has emerged as the most efficient. The work also reports strong amplitude modulation, which again is unexpected and not completely convincing. Furthermore, the bandwidth of the resulting modes is quite narrow as there is no spatial hole burning to enforce multimode operation. Additionally, the production of the intensity waveform from a SWIFTs measurement is similar to the addition of Fourier components to retrieve a time domain signature. Missing just a few of these components can drastically change, or modulate the amplitude of the intensity.

Conclusion

This work represents the majority of the author's research in pursuit of a doctorate and thus it is only appropriate that an interim conclusion be included. The analysis of FC generating QCLs has been anything but straight forward. These lasers are chaotic in their operation, inherently due to the fact that they are let to "run free" as they are built to be broadband and have no wavelength guiding elements. A theoretical analysis of these lasers must therefore elucidate important cogs in the lasers rather than simply trying to encompass all aspects of the QCL operation and force them to fit into a mathematical analysis, from which we will receive little insight. Further work must be done to understand all the cogs and their effects, gain shape and saturation plays an important role as it is inherently tied to dispersion. Spatial hole burning is obviously tremendously important, and has been used to create a very stable laser. Spectral hole burning is less of a factor than initially assumed, and we postulate that this arises from the fact that the current is injected at a steady rate through all periods of the QCL. It is the authors hope that these insights can help advance control over FC generating QCLs, but even more importantly illustrate a methodology to approaching the study of QCLs in a way to identify all key components of a broad and stable frequency comb.

Chapter 5: Calculating the Linewidth of an Optical Frequency Comb with Arbitrary Temporal Profile

The optical linewidth of a laser refers to the width of its optical spectrum, or more precisely the power density spectrum. Aside from the natural linewidth of the cold cavity, the linewidth of a laser is strongly related to the temporal coherence of the emitted radiation and by phase noise present in the cavity. Phase noise can be introduced in many ways such as changes in the effective length of the cavity, thermal fluctuations, and noise introduced by the pump source. Most fundamentally, however, noise is introduced by spontaneous emission. The calculation of a single mode linewidth is fairly straight forward, and when calculating the linewidth of a FC where all spectral components are locked the resulting linewidth is still fairly narrow, which is essential for FC applications. Frequency combs generated from mode locked lasers [67, 68], that are subsequently broadened by a non-linear material [69-71], as well as continuous wave pumping of non-linear microresonators [72-77] effectively lock all the spectral components of the comb with an equal phase. In this case the linewidth of the FC can be essentially the same as that of the laser that pumps it as spontaneous emission is no generated without gain and it is experimentally well known that the linewidth of the mode locked lasers is comparable to the linewidth a single mode laser of equal average power since all the modes are locked into the same phase [77, 78]. The linewidth and phase noise of mode locked lasers has been theoretically explored in a number of works [79-81] where it was assumed that all the modes are locked into the same phase since until recently that was the only practical way to lock all the phases using saturable absorber or an active intensity of phase modulator. But as QCL FC

with its mostly FM character appeared it became important to understand what kind of linewidth can be achieved in them. Measurements34 have shown that the linewidth is indeed very narrow, comparable to the linewidth of a single-mode QCL operating at the same power. In this work we provide an intuitive and physically transparent picture of why the linewidth of these FCs is so narrow.

Schawlow and Townes Derivation of Laser Linewidth

The theoretical analysis presented in this chapter is based on the Schawlow-Townes (ST) derivation and thus it is worth-while to introduce it here. . According to the original work of Schawlow and Townes [82] refined by Lax [83] the linewidth of a single mode laser is inversely proportional to the power P_{out} , or to the total number of photons in the cavity N_p. One would think then that the linewidths of the modes in a multimode laser would be inversely proportional to the number of photons in each individual mode, however due to phase-locking the width of the modes does not necessarily increase.

While there are multiple methods to deriving the ST equation we will begin by considering the normalized rate equations for a four-level laser. While one can calculate the steady state solution of a laser above threshold, in order to investigate how the laser reaches this mode one must include the spontaneous emission term, β_{sp} .

$$\begin{aligned} \frac{dn_2}{dt} &= \frac{1}{\tau_2}(p - n_2 - n_2 n_p) \\ \frac{dn_p}{dt} &= \frac{n_p}{\tau_p}(n_2 - 1) + \beta_{sp}\frac{n_2}{\tau_2} \end{aligned} \tag{5.1}$$

Where the variable $n_2 = N_2 / N_t$ is the upper level population normalized to threshold $N_t = \left(\sigma_{21} v_g \tau_p\right)^{-1}$, $n_p = N_p / N_{p,sat}$ is the number of photons normalized to saturation $N_{p,sat} = \left(\sigma_{21} v_g \tau_2\right)^{-1}$, and lastly $p = R_p / R_{p,t}$ is the pump power normalized to threshold $R_{p,t} = \left(\sigma_{21} v_g \tau_p \tau_2\right)^{-1}$. In this case τ_p is the photon lifetime, τ_2 is the upper laser level lifetime, and σ_{21} is the cross-section of the medium.

Now, including the spontaneous emission term, the steady state solution is

$$n_p = \beta_{sp} \frac{n_2}{\tau_2} \frac{\tau_p}{1 - n_2} \tag{5.2}$$

For the case of very weak pumping $n_2 << 1$ and we have $n_p \approx \beta_{sp} \frac{n_2}{\tau_2} \tau_p$ which makes a lot of sense as the photon density is a product of the photon injection rate and the photon lifetime. Now let us consider what the linewidth is under these conditions. As it is related to the photon lifetime, we redefine our lifetime as $\tau_p' = \frac{\tau_p}{1 - n_2}$ and we can now calculate the linewidth to be

$$\Delta\omega_{1/2}^{las} = \tau_p'^{-1} \Delta\omega_{1/2}^{las} = \tau_p^{-1}(n_2 - 1) = \tau_p^{-1} \beta_{sp} \frac{\tau_p}{n_p \tau_2} = \frac{\beta_{sp}}{n_p \tau_2} \tag{5.3}$$

Thus the linewidth depends on the ratio of spontaneous emission into the mode and the stimulated emission in the mode. Now, we must calculate the total rate of spontaneous emission into the small interval of frequencies $d\omega$ as

$$\frac{dN_{p,sp,total}}{dt} = A_{21} N_2 \frac{V_a}{V_c} g(\omega) d\omega \tag{5.4}$$

where we have made distinction between the gain volume V_a and the cavity volume V_c. The number of all modes in that frequency interval is $N_m(\omega) = V_c n^3 \omega^2 d\omega / \pi^2 c^3$

Thus we obtain for the rate of spontaneous emission into one mode

$$\frac{dN_{p,sp}}{dt} = \frac{dN_{p,sp,total}}{dt} \frac{1}{N_{\mathrm{mod}es}(\omega)} = A_{21} \frac{g(\omega)}{\rho(\omega)} N_2 \frac{V_a}{V_c^2} N_2 \tag{5.5}$$

Now, since $\sigma_{21}(\omega) = \hbar$) $/ v_g$ we obtain

$$\frac{dN_{p,sp}}{dt} = \sigma_{21}(\omega) \frac{c}{n} \frac{V_a}{V_c^2} N_2 \tag{5.6}$$

Now we can re-normalize the variables as before, however we now include the volume ratio in the threshold carrier population term, $N_t = V_c / V_a v_g \sigma_{21} \tau_p$ giving us

$$\frac{dn_{p,sp}}{dt} = \sigma_{21}(\omega) v_g \frac{\tau_2}{\tau_p V_c} n_2 = (N_{p,sat} V_c)^{-1} \frac{n_2}{\tau_2} \equiv \beta_{sp} \frac{n_2}{\tau_2} \tag{5.7}$$

And therefore

$$\frac{\beta_{sp}}{\tau_2} = \frac{1}{V_c N_{p,sat} \tau_p} \tag{5.8}$$

And from (5.3) we can then calculate the expression for the linewidth

$$\Delta\omega_{1/2}^{(las)} = (n_p N_{p,sat} V_c)^{-1} \frac{1}{\tau_p} = \frac{1}{N_p V_c} \frac{1}{\tau_p} = \frac{\hbar}{P_{out}} \omega_{1/2}^2 \tag{5.9}$$

This expression was obtain under assumption that $N_1 = 0$. Since in general this is not true we can introduce a spontaneous emission factor, $n_{sp} = \frac{N_2}{N_2 - N_1} > 1$, to obtain the expression for the Schawlow-Townes linewidth.

$$\Delta\omega_{1/2}^{(las)} = \frac{\hbar}{P_{out}} \cdot n_{sp} \Delta\omega_{1/2}^2 \tag{5.10}$$

Thus one can see that in order to have a narrow linewidth one needs a very long cavity. Long cavities tends to keep the laser photons inside for longer. Furthermore, in a long cavity the spontaneous emission is split among larger number of modes, hence fraction of spontaneous emission going into the given mode decreases. Therefore, very long cavities or, equivalently, external resonators are often used for this purpose. Next we move to our analysis of a multimode, phase coherent FC with an arbitrary time domain profile. In this case a four-level approximation with a very low population of the lower level is a good fit for the QCL.

Derivation of QCL Linewidth

As stated before, this work begins with a simple derivation of the Schawlow-Townes (ST) linewidth for arbitrary laser FCs based on the orthogonality of modes and the fact that the spontaneous noise amplitudes in each mode are uncorrelated. We also provide a simple intuitive and physically transparent picture of why only a small fraction of spontaneous noise actually affects the linewidth of the arbitrary FC. We consider the situation in which the steady phase locking of the modes has already taken place, and as explained in [79], following the standard methods in calculating oscillator linewidths,[84] we assume that the noise sources are

not strong enough to disrupt the phase relationship between modes, and hence, the total field can be written as

$$E(t,z)=\sum_{n=1}^{N}E_n(t)e^{-j\omega_n t}a_n(z)=A(t)\sum_{n=1}^{N}f_n e^{-j\omega_n t}a_n(z), \tag{5.11}$$

where ω_n is a frequency of n-th mode, $a_n(z)\sim\sin(\omega_n z/v)$ is the normalized shape of the n-th orthogonal mode, v is the phase velocity of light, $\int a_m a_n dz=\delta_{mn}$,and the Fourier amplitudes f_n have been normalized as $\sum_{n=1}^{N}\left|f_n\right|^2=1$ .The average power can then be defined as $\bar{P}=\left|A\right|^2$.

The normalized distribution of normalized instant electric field $E(z)$ inside the cavity and one of the modes $a_m(z)$ is shown in Figure 5-1a. Let us now write the expression for the temporal development of the slow-varying amplitude of the n-th mode [5, 85]

$$\frac{dE_n(t)}{dt}=\frac{1}{2}g_n\left(\bar{P}\right)E_n-\frac{1}{2}\frac{E_n}{\tau_c}+iD_nE_n+\sum_{l\neq n}^{N}\sum_{m\neq l,n}^{N}g_{nlm}\left(\bar{P}\right)\kappa_{nlm}E_lE_m^*E_{n+m-l}+\frac{S_n(t)}{\tau_c} \tag{5.12}$$

where $\frac{1}{2}g_n\left(\bar{P}\right)$ is the gain that includes both self-saturation and cross-saturation, $g_{nlm}\left(\bar{P}\right)\kappa_{nlm}$ is the four-wave mixing (FWM) term (but in case of active mode locking it may have a different shape corresponding to the sideband generation), τ_c is the cavity lifetime, $D_n=2n^2\pi^2\tau_c^{-2}\beta_2 v_g$ is the dispersive term, v_g is the velocity and β_2 is the GVD and $S_n(t)$ is the noise complex amplitude in the n-th mode. The gain and FWM terms dependence on average power becomes important further on (see (5.18)) because in order to estimate the linewidth one must take into account the fact that the population inversion is not pinned at the threshold but is slightly less than that. The noise can be caused by the spontaneous emission of photons in the n-th mode,

but it can also be due to a far more mundane causes such as cavity length oscillations due to random vibrations. The noise amplitudes of different modes are not correlated, $\left\langle S_n^*(t)S_m(t')\right\rangle = S^2\delta_{nm}\delta(t-t')$ Upon substituting (5.11) into (5.12) we obtain

$$\frac{dA(t)}{dt}f_n = \frac{1}{2}g_n\left(\bar{P}\right)A(t)f_n + iD_nA(t)f_n - \frac{A(t)f_n}{2\tau_c} + A(t)\left|A(t)\right|^2\sum_{l\neq n}^{N}\sum_{m\neq l,n}^{N}g_{nlm}\left(\bar{P}\right)\kappa_{nlm}f_lf_m^*f_{n+m-l} + \frac{S_n(t)}{\tau_c}$$

(5.13)

The FWM terms under double summation have "amplitude" or in-phase parts and "phase" or quadrature parts. The quadrature terms cause a frequency chirp and once the stable regime has been reached (i.e. once the relative phases and amplitudes of modes f_n get locked while the amplitude of the envelope $A(t)$ can still experience change on a slow scale) they get compensated by the group velocity dispersion terms D_n ,i.e.

$$|A(t)|^2\ \mathrm{Im}\sum_{l\neq n}^{N}\sum_{m\neq l,n}^{N}g_{nlm}\left(\bar{P}\right)\kappa_{nlm}f_lf_m^*f_{n+m-l} + iD_nA(t)f_n = 0 \qquad (5.14)$$

Multiply now both sides of (5.13) by f_n^* and perform summation. The amplitude terms only cause the energy redistribution between the modes, hence once the stable operational regime has been reached they all sum up to zero. i.e.

$$\mathrm{Re}\sum_{n}^{N}\sum_{l\neq n}^{N}\sum_{m\neq l,n}^{N}g_{nlm}\left(\bar{P}\right)\kappa_{nlm}f_lf_m^*f_{n+m-l}f_n^* = 0 \qquad (5.15)$$

The new differential equation then becomes

$$\frac{dA(t)}{dt} = \frac{1}{2}g\left(\bar{P}\right)A(t) - \frac{A(t)}{2\tau_c} + \sum_{n=1}^{N}S_n(t)f_n^* \qquad (5.16)$$

Obviously any small deviations from (5.14) and (5.15) can be treated as additional sources of noise and simply added to (5.16). Deviation from (5.14) caused by the stochastic nature of power $|A(t)|^2$ are nothing but additional phase noise due to gain/index coupling which can be taken care of by introducing the linewidth enhancement factor [86] α later on and which we are not considering here for the sake of simplicity as it is known to be small in the QCLs. Let us now examine the noise term. Since the phases of complex noise amplitudes in each mode are random one must sum up the noise powers, i.e. total noise power is $\left\langle |S_{tot}|^2 \right\rangle = \sum_{n=1}^{N} \left\langle |S_n|^2 \right\rangle |f_n|^2$.

Under a reasonable assumption that all the noise powers $\left\langle |S_n|^2 \right\rangle$ are identical, i.e. we obtain $\left\langle |S_{tot}|^2 \right\rangle = \left\langle |S_n|^2 \right\rangle$, i.e. the total noise added to a given stable phase-locked signal is equal to the noise in any given mode, and we have

$$\frac{dA(t)}{dt} = \frac{1}{2} g\left(\bar{P}\right) A(t) - \frac{A(t)}{2\tau_c} + \frac{S_{tot}(t)}{\tau_c} \tag{5.17}$$

where $S_{tot}(t)$ is the noise source whose power is equal to the power of noise in any given mode.

In other words, this equation looks exactly like the equation for a single mode laser and is therefore bound to yield the linewidth that is determined by the total average power $\bar{P} = |A|^2$ rather than by a power in a given mode. One easy way to interpret this situation is to simply assume that one can take any linear combination of modes in the cavity and just call it an eigenmode of the system [87]. Of course, as different modes do have different frequencies their linear combination does not necessarily amount to an eigenmode, which after all is

supposed to have a well-defined frequency, but this is still a useful analogy which allows equation (5.17) to be obtained instantly.

One can now obtain the ST linewidth for the case when the only noise source is the spontaneous emission following the framework in original ST work [82] introducing the photon number in the cavity as $N_p = |A|^2 \tau_{rt} / \hbar$ where τ_{rt} is the cavity round trip time, so that (5.17) becomes

$$\frac{dN_p}{dt} = \left[g\left(N_p\right) - \frac{1}{\tau_c} \right] N_p + n_{sp} g\left(N_p\right) \tag{5.18}$$

where $n_{sp} \geq 1$ is the excess noise factor caused by the finite population of the lower laser level (subband in case of QCL) . In steady state the saturated gain is $g(N_p) = N_p \tau_c^{-1} / \left(N_p + n_{sp}\right)$ and the linewidth can be introduced as the effective photon decay rate,

$$\Delta\nu_{ST} = [\tau_c^{-1} - g(N_p)] / 2\pi = \frac{n_{sp}}{N_p + n_{sp}} \tau_c^{-1} / 2\pi \approx \Delta\nu_0 n_{sp} N_p^{-1} \tag{5.19}$$

where $\Delta\nu_0 = \tau_c^{-1} / 2\pi$ is the cold cavity linewidth. Relating the photon density inside the cavity to the output power as $P_{out} = \hbar$ ∇_p where η_{out} is the outcoupling efficiency, the ST linewidth assumes a more familiar shape $\Delta\nu_{ST} = 2\pi\eta_{out}\Delta\nu_0^2\hbar$

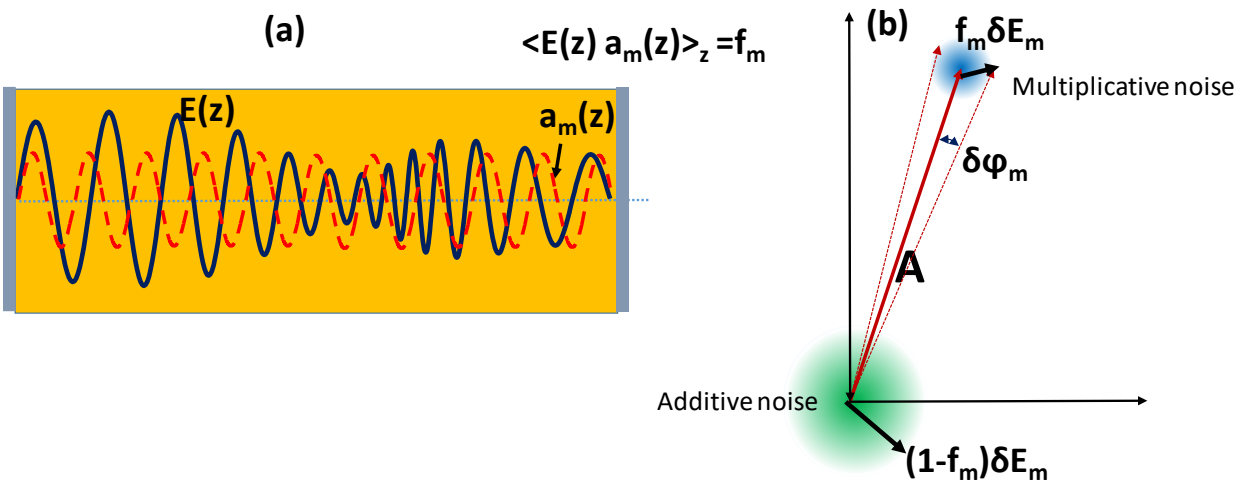

Figure 5- 1. (a) Spatial distribution of one of the cavity modes $a_m(z)$ and instant field $E(z)$ inside the laser cavity (b) Phasor representation of the phase noise and linewidth in arbitrary FC. The amplitude of the coherent electric field FC is A. The electric field of a photon emitted into the m-th mode is δE_m. The averaged over the cavity length product of the two fields, proportional to the weight of the m-th mode in the total laser field f_m, engenders the multiplicative noise that in the end contributes to the linewidth. The rest of the spontaneous electric field, proportional to $1-f_m$ is orthogonal in space to the coherent field and only generates additive noise.

Physical interpretation

Let us now consider the physical interpretation of the result – how come that despite the fact that each of N modes contributes to the spontaneous emission, only $1/N_{th}$ of that radiation contributes to both phase and amplitude noise of the laser comb? For a short (mode-locked with all phases equal) pulse the interpretation in time domain is obvious: the pulse sequence containing N cavity modes has the duty cycle of exactly 1/N – hence only 1 of each N spontaneously emitted photons will affect the phase (and amplitude) of the pulse – the rest of them will appear as additive noise which can always be filtered out. For FM frequency comb a similar time domain interpretation can be made: assume for simplicity that the laser simply jumps from one mode to another – i.e. instant frequency is always equal to one of the cavity

frequencies. Obviously the spontaneous emission into other N-1 modes does not contribute to the multiplicative phase noise but simply presents an additive noise.

To understand the narrow linewidth of the arbitrary comb rather than using temporal domain it is helpful to turn instead to the spatial dependence of the signal and consider the change of phase imposed by the emission of a single photon into the m-th mode. According to (5.18) each photon is emitted every $\delta t_m = \tau_c / n_{sp}$ and the power of that photon, $\delta P_m = |\delta E_m|^2 = \hbar$. Therefore, the phase change imposed by this photon is (see Figure 5-1a)

$$\delta\varphi_m = \int E(t,z)\delta E_{mQ} a_m(z)dz / \int E^2(t,z)dz = f_m \delta E_{mQ} / |A| \tag{5.20}$$

where δE_{mQ} is the quadrature component of the spontaneous emission and we have used the orthogonality of the laser modes in space. Now, in the time interval Δt there will be $\Delta N_m = \Delta t / \delta t_m = n_{sp}\tau_c^{-1}\Delta t$ photons emitted into the m-th mode and according to random walk process theory the variance of the phase will be

$$\left\langle \delta\varphi^2 \right\rangle = |f_m|^2 \frac{|\delta E_{mQ}|^2}{|A|^2} \Delta N_m = \frac{\hbar}{|A|^2} \frac{f_m|^2}{\tau_{rt}} \frac{\Delta t}{} = \frac{n_{sp}\tau_c^{-1}}{N_p} |f_m|^2 \Delta t \tag{5.21}$$

But according to the theory for the random walk process with the variance $\left\langle \delta\varphi^2 \right\rangle = 2\pi C\Delta t$ the power spectral density of the phase noise can be found as $S_\varphi(\omega) = C/\omega^2$ with the linewidth being $\Delta\nu = C$. Therefore, the linewidth can be found as

$$\Delta\nu = \left\langle \delta\varphi^2 \right\rangle / 2\pi\Delta t = \frac{n_{sp}\Delta\nu_0}{N_p} |f_m|^2 \tag{5.22}$$

Comparing (5.22) with (5.19) one can state that the linewidth's contribution from spontaneous emission in the m-th mode is proportional to its relative weight f_m^2 , i.e. roughly 1/N. Thus

physical interpretation in spatial domain is simple – since the spontaneous emission into a given resonator mode only weakly overlaps in space with actual distribution of the laser field inside the cavity, most of this emission ends up as an additive noise and does not contribute to the phase/frequency noise and linewidth. This situation is schematically explained in Figure. 5-1b.

Conclusion

The key conclusion reached in this work is that we have confirmed the previously made argument that the linewidth of a given multi-mode phase locked laser emission does not depend on exactly what is the phase relation between the individual modes as long as this relation exists, i.e. as long as the locking mechanism (which can be a fast saturable absorption as in conventional mode locked laser or a fast saturable gain in QCL) is strong enough to overcome dispersion of group velocity and gain. The FC signal may indeed be a short pulse [67], an FM signal [5], or a combined AM/FM signal [39, 40] - from the point of view of most practical FC applications the character of comb in time domain is irrelevant and the measurements with all kinds of combs can be expected to yield the results with roughly the same precision.

Let us compare FC obtained directly from the phase-locked multimode laser with the one generated in a micro-resonator pumped by a single mode laser [76]. For equal average powers both lasers would have similar linewidth but the multimode laser will have substantially higher additive noise due to spontaneous emission. This noise can easily be filtered out from the single mode laser. But the efficiency of the laser FC generation is typically much higher (precisely due to the presence of laser gain at each mode) therefore the micro-resonator comb must be amplified and the spontaneous emission in the amplifier will of course generate significant additive noise which will negate all the purported advantages of micro-resonator comb.

Therefore, an FC generated by the free-running lasers with fast saturable gain media, such as QCLs can provide measurements just as good if not superior to the comb produced using nonlinear processes in micro-resonators given comparable signal to noise ratios combined the simplicity, smaller size and higher efficiency of the free running laser FCs

Chapter 6: Offset frequency stabilization through dispersion engineering

The last body of work included in this dissertation introduces a novel methodology to improve the stability of QCL FCs through simple geometric design in an effort to further increase the bandwidth and spectroscopic resolution. While this study is tailored for QCLs, the theory behind stabilization of the offset frequency applies to all frequency combs. As stated in Chapter 1, a FC spectrum consists of discrete lines described as $f_p = f_{off} + p\Delta f$, where Δf is the free spectral range (FSR) and f_{off} is the offset frequency (Figure. 6-1a, inset), a consequence of inequality between the phase and group velocities. In order to retrieve the absolute frequency of a comb line, one must know both the repetition rate of the comb, equal to the FSR Δf , and the offset frequency f_{off} , both of which experience time dependent drift resulting in phase noise. While QCL FCs have been successfully used for practical measurements in both the IR and THz regions [88, 89] the stability of these lasers still offers room for improvement. Stabilizing FCs presents a difficult challenge that is usually addressed by locking the frequency to an external source [90-92], which can complicate the setup and delay data acquisition time. If instead the frequency was naturally locked through engineering of the dispersion in the medium we expect phase noise to be significantly improved, however more importantly, the laser will be relatively unaffected by the countless environmentally introduced perturbations.

Phase Noise in Frequency Combs

As stated earlier, if both the FSR, Δf , and the offset frequency, f_{off} , also referred to as the carrier-envelope offset frequency when concerning pulses, the absolute frequency of all the comb lines are also known. Under these circumstances, the spectral line under interrogation can be measured by obtaining the beat notes on a fast detector. The lowest beat note is the frequency distance between the unknown line and the closest comb line. Identifying the closest comb line can then be achieved by taking a less accurate spectral measurement and inferring the sign of the beatnote (as it is the absolute value of the spacing between combs) by tuning the frequency comb up or down.

Phase noise mitigation is a critical challenge in comb-based spectroscopy and communications. In dual-comb spectroscopy, offset phase noise sets the ultimate limit to the resolution of the system. While typical free-running linewidths may be acceptable for the measurement of broadband absorbers such as solid samples, phase-stabilized sources are needed for applications such as Doppler-limited molecular spectroscopy [92]. In addition, mutual coherence of the two comb sources is required to resolve the intensities of the individual lines. While mutual incoherence can be overcome through the usage of phase-correction techniques, larger fluctuations necessitate the usage of more sophisticated algorithms that may preclude real-time averaging. In contrast, repetition rate fluctuations are typically much easier to detect and stabilize, as they can be measured with a simple fast detector and can frequently be electrically measured from the laser itself, using self-detection.

Noise in FCs is a very complicated issue as there are many different sources that can introduce many different types of noise into the system. Environmental or external noise can include perturbations such as mirror vibration, thermal fluctuations, and pump noise. Also of note is quantum noise such as spontaneous emission, with optical losses, and a linewidth enhancement factor with is the result of coupling between intensity noise and phase noise. Due to strong coupling of all the modes in a mode locked laser the quantum limited noise of the laser is mostly determined by the laser power, just as in the Schawlow-Townes limit of a single mode laser. It was also shown that this is also true for QCLs as described in [].

All these various noises can show up in the FC in many different ways yet can be expressed as two different scenarios, and can be visualized using the "elastic tape picture" [93]. This visualizes the FC as a rubber band that is randomly stretched while held at some fixed point. Common mode fluctuation is one of the mentioned scenarios which, for example, results from a change between the group and phase delay of the resonator while the ratio of the two remain constant. Vibrations in the cavity mirrors result in a change in the cavity length and causes stretching in the frequency comb at a very low fix point. In this case one can imagine that the FSR is greatly affected by this scenario, however the offset frequency sees very little. In another case, the difference of the group and phase delay changes while one of them is held constant. This is an example of the result of thermal fluctuations, in this case the fixed point of the rubber band will be on the order of the optical frequency resulting in a large change in the offset frequency.

Measurement of the FSR is relatively easy, all it requires is a fast detector to identify the beat note of the FC. The mechanism of stabilization for the FSR is done so that it compensates

noise originating from changes in the cavity length, an example of compensation would be to use a piezoelectric mirror in a feedback loop to stabilize the FSR. However, in this case the time response of the mirror [94] can still result in excess noise. An example of stabilizing the offset frequency is the slight tilting of a cavity mirror, which strongly effects the group delay however does not change the cavity length [95]. It is also possible to obtain a comb with zero offset by accessing parts of the comb through difference frequency generation.

Quantifying the phase noise in FCs is usually done using the power spectral density of the phase noise but analysis of the offset and FSR drift is also accomplished with Allan deviation measurements. Shown in Figure 6-1 below is an Allan deviation measurement of a very low noise frequency comb generated from a femtosecond, semiconductor saturable absorber mirror (SESAM) mode-locked, Er:Yb:glass (ERGO) laser [96]. In this case the figure shows a comparison of the fluctuations of frequency offset between a commonly used fiber laser and the ERGO laser which is phase stabilized with a piezo electric mirror and feedback supplied to the pump laser current.

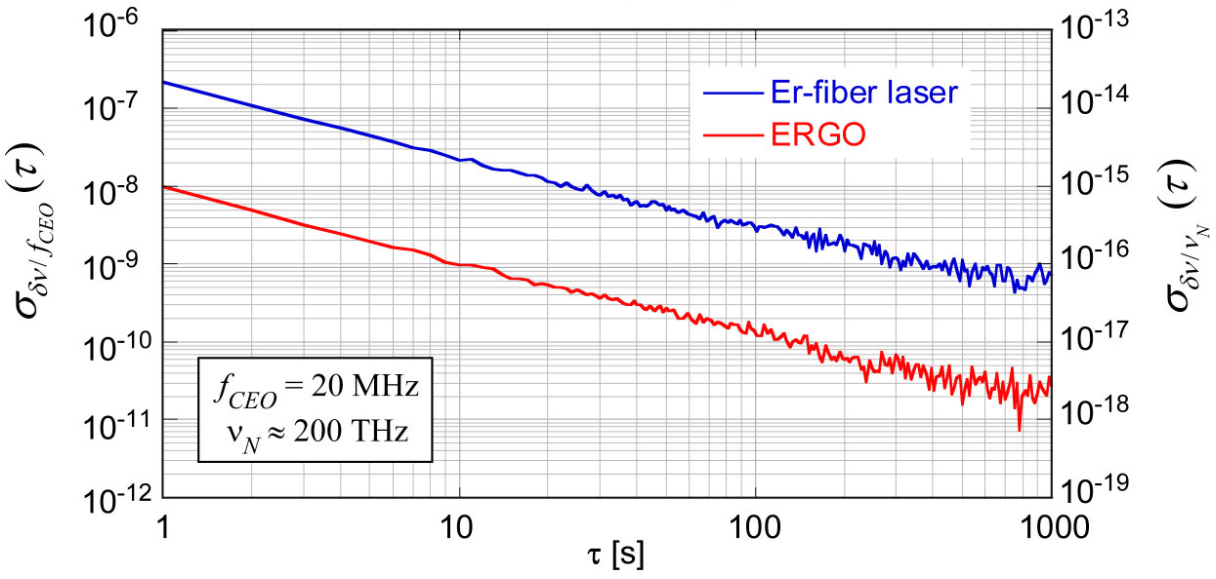

Figure 6- 1. Allan deviation of the offset frequency for a commercial fiber laser comb and a comb developed in [96]. The left axis is the stability in reference to the offset frequency and the right axis is in reference to the optical frequency.

For QCLs phase noise is also still an issue, however much work has been done to achieve a fairly stable comb. Tactics to stabilizing both FSR and offset are similar to those used with other frequency comb sources. Shown in the figure below is a QCL frequency comb that employs purely current driven locking of the phases. This is very advantageous as it uses no moving parts. In order to control the FSR drift of the FC, this paper injection locks the QCL at a frequency approaching the roundtrip frequency of the laser. Offset frequency stabilization is then performed by stabilizing any mode of the RF comb to a local oscillator using a phased locked loop acting on the drive current.

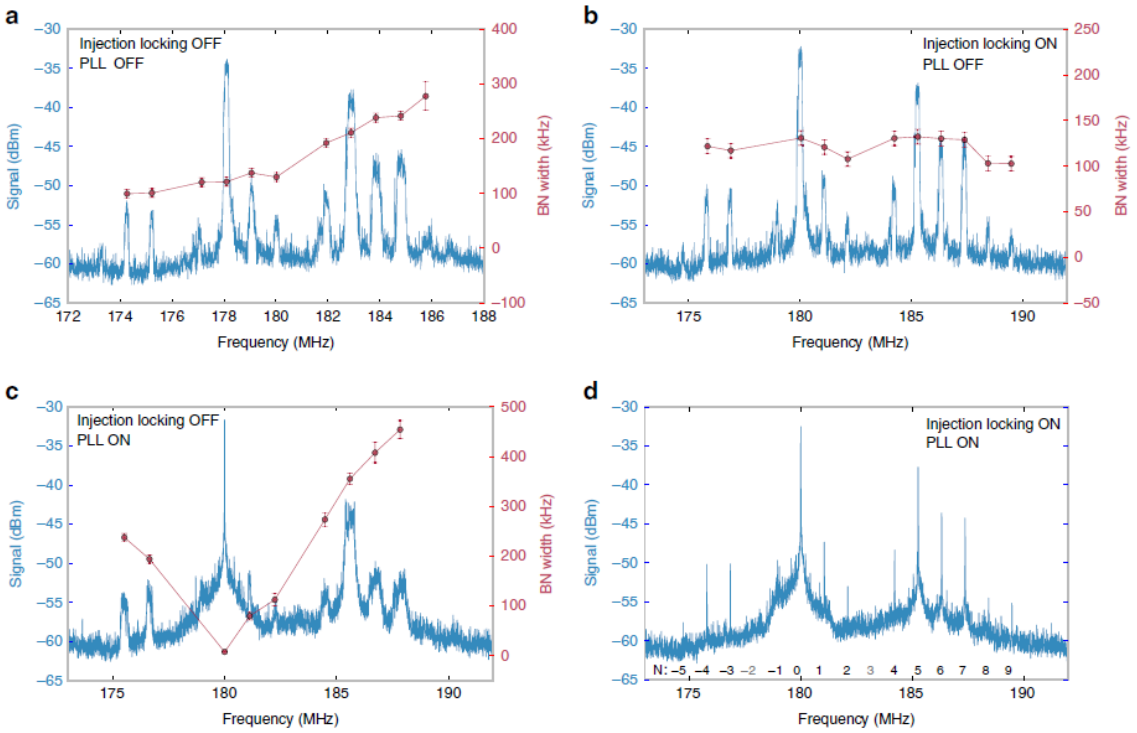

Figure 6- 2. RF comb spectra (blue-line) and beat note linewidth (red) of a A) free running, B) stabilized FSR and free running offset frequency, C) free running FSR and stabilized offset D) fully stabilized QCL.

While not all noise contributes to the linewidth of a beat-note, its PSD must be above a certain value called the β-line [97], the above figure clearly illustrates the independent locking mechanisms employed in this system. In Figure 6-2a and the beat note linewidths show a linear increase with the comb order, N, which signifies a drift in the FSR. Offset frequency stabilization can be seen in Figure 6-2b, where a reference oscillator is employed to stabilize offset frequency. Here we see that the beat note linewidth is fairly constant and independent of the mode number. Employing both techniques we see very narrow beatnote linewidths, enabling this technology to perform extremely high resolution measurements. However, utilizing this stabilization scheme does have some effect on the bandwidth of the comb and injection locking is extremely energy inefficient. Thus another method of stabilization may be advantageous.

Power Law Dispersion

Several methods have been used to computationally de-noise FC data [98, 99], usually combined with dispersion compensation [31, 100] . However, it is much more difficult to continuously measure the offset frequency which requires a reference source that can greatly complicate the platform. Introduced here [101] is a completely novel, passive technique of mitigating the phase noise in optical FCs by reducing the drift of the offset frequency. This can be achieved by customizing the dispersion to attain a power law dependence of the wave vector on frequency, k(ω)~ωα, insuring a constant ratio between group and phase velocities. When this condition is maintained, the drift offset frequency is passively mitigated as the group and phase velocities are held in a constant ratio and phase noise is reduced. This desired power law dispersion can be easily engineered by properly adjusting the thickness of the QCL active region and a stable offset frequency can be combined with low residual group velocity dispersion. However, it should be noted that it might not be possible to achieve a power law dispersion while also completely optimizing the group velocity dispersion.

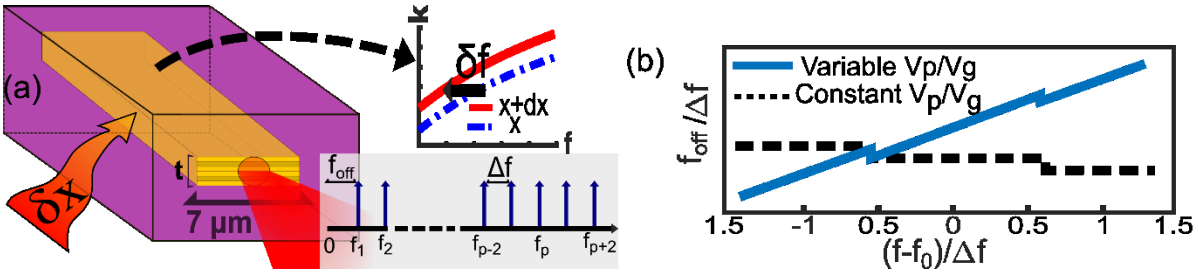

Figure 6- 3. A) Geometry of the QCL ridge waveguide and the FC produced by it with an inset showing external perturbation δx and its impact on the dispersion δf (inset). B) Offset frequency vs frequency drift for the arbitrary dispersion with variable phase-group velocity ratio (solid) and customized constant phase-group velocity ratio (dashed).

Frequency offset, f_{off}, and FSR, Δf, both vary as a result of unavoidable changes in the permittivity of the waveguide that can be caused by temperature fluctuations, mechanical vibration, carrier density fluctuations, and so on. The frequency offset varies far more rapidly than the modal spacing, the cause of which can be traced to disparity between the group, v_g, and phase, v_p, velocities. To the first order, as conditions (such as temperature, vibrations, humidity, etc) change by δx the dispersion curve $k(f)$ shifts by $\delta f \sim f \delta x / x$ (inset of Figure 6-3), with a commensurate change in both v_g and v_p. The FSR will experience a gradual drift (better envisioned as expansion/compression) with change in v_g, but, as shown in Figure 6-3b, f_{off} will experience jumps when δf exceeds what is essentially the FSR, $\Delta f_p = v_p / 2L$ in addition to a steady drift between jumps. These jumps are unavoidable, however changes in permittivity are typically small, due to, for example, the low temperature coefficient of refractive index of InGaAs about 1×10^{-4} [102, 103], and a similarly weak dependence of index on carrier density. To have $\delta f \sim \Delta f_p$ would require temperature change by as much as 5K, far more than a typical temperature fluctuation. Within one FSR, the drift of f_{off} ,as shown by the solid line in Figure 6-3b, can be quite substantial for an arbitrary dispersion. However, we shall show that if the ratio of v_g / v_p can be made constant, this drift will be reduced to zero as indicated by the dashed line in Figure 6-3b.

We shall explore how the offset drift develops and is mitigated, by starting with the condition for the oscillation of the central frequency, which we designate the p^{th} mode. Its frequency is

$$f_p = m v_p \left(f_p \right) / 2L , \quad (6.1)$$

where $v_p(f_p) = k_p / \omega_p$ and k_p is the propagation constant. Note that on the other hand, the FSR that determines the optical comb period in frequency space is determined by the group velocity as $\Delta f = v_g / 2L$. We can equivalently state that the condition for the oscillation of the p^{th} mode is

$$f_p = f_{off} + p\frac{v_g}{2L}. \qquad (6.2)$$

Due to difference in phase and group velocities, integer $p \neq m$ and the relation between the two can be established from (6.1) and (6.2) as

$$p = Int\left(\frac{f_p}{v_g / 2L}\right) = Int\left(m\frac{v_p}{v_g}\right). \qquad (6.3)$$

We assume that the m^{th} mode is the central mode near the peak of the gain from which the comb expands via four-wave mixing (FWM) and therefore the FSR is determined by the group velocity at the frequency $f_p \equiv f_0$, at the peak of the gain spectrum. Substitution of (6.3) into (6.2) yields the expression for the offset frequency

$$f_{off} = \Delta f\left[m\frac{v_p}{v_g} - Int\left(m\frac{v_p}{v_g}\right)\right]. \qquad (6.4)$$

and the change in offset frequency caused by the aforementioned shift, δf, of the dispersion curve

$$\delta f_{off} = f_{off}\delta v_g / v_g + \Delta f\,\delta\left[m\frac{v_p}{v_g} - Int\left(m\frac{v_p}{v_g}\right)\right]. \qquad (6.5)$$

Upon close inspection, the term in the square brackets lead to a large shift in offset frequency, a small change of v_p / v_g gets multiplied by a very large number *m* which is on the order of a few thousand.

Therefore, one can facilitate stabilization of offset frequency by assuring that the ratio v_p / v_g remains constant for as long as $\delta f < \Delta f_p$, i..e between the "jumps" in Figure 6-3b. This condition can be written as

$$v_p / v_g = (\omega / k)(dk / d\omega) = \alpha > 1, \qquad (6.6)$$

and it easily follows that $\partial k / k = \alpha(\partial\omega / \omega)$ and finally we arrive at a power law conditioned dispersion

$$k(\omega) = \frac{\omega_0}{c}(\omega / \omega_0)^{\alpha}, \quad (6.7)$$

where ω_0 is the frequency of the central mode. This equation highlights the mutual exclusivity between full GVD compensation (although it is not clear that such full compensation is needed [28]) and a stable offset frequency as that would require an unattainable $\alpha = 1$, i.e. constant phase velocity. Since we know that achieving a perfect GVD compensation typically calls for a complicated solution, such Gires-Tournouis Interferometer, grating, or coupled waveguides[31, 100, 104], it is reasonable to expect that a "designer" dispersion of Eq (6.7) also requires elaborate features added to the simple ridge waveguide of a QCL. Yet surprisingly the power-law dispersion (6.7), over a reasonably wide frequency range, can be achieved by simply adjusting the width of the active layer of a ubiquitous buried ridge waveguide (which means that the solution is applicable to a broad variety of FC platforms). It should be noted that change in v_p / v_g inside the waveguide is the main, but not the only reason for f_{off} drift. External factors, such optical feedback can also cause the drift, which can be expressed as a function of ratio of group and phase delays – stabilizing that ratio would require introduction of these external factors into the waveguide dispersive elements.

Designing a ridge waveguide for lower offset drift.

As a proof of concept, we design here a buried ridge waveguide, typical of MWIR (4.7 μm) QCLs [105], using a two-dimensional, finite-difference time-domain (FDTD) mode solver to calculate GVD and offset drift. The geometry of the buried ridge waveguide is shown in Figure 6-3a. The model consists of an active core region sandwiched between upper and lower cladding layers of InP. Wavelength dependent indices of refraction where calculated using Adachi's method[106]. The index of the active layer was calculated for InGaAs and then artificially lowered to incorporate aluminum present in the superlattice. Additionally, dispersion from gain was introduced by Kramers-Kronig method using a super-Gaussian distribution of the gain, with peak value of 10cm^{-1}. The active layer was modeled as 7 μm wide with varying thickness. Dispersion from material, gain, and waveguide geometry have all been incorporated. If we define the change in frequency as δf , we can equate it to the relative change in effective index, $\delta n / n$. It is readily apparent that this relates to the relative change in temperature, or even more generally to some other relative, yet more general parameter, $\delta x / x$. The change of the ratio v_p / v_g versus index change is shown in Figure 6-4a for different active layer thicknesses. Active layer thickness of $1800 \pm 10 nm$ results in an almost perfectly constant ratio and the 10nm tolerance is easily attainable with MBE or MOCVD. We can now evaluate the slope, *r*, of the offset frequency drift from Eq (6.5) with respect to δn , $r = (\delta f_{off} / \delta n) n$. See Figure 6-4b, where *r* is plotted versus the active layer thickness. It is obvious that a low *r* is crucial to low phase noise and high resolution spectroscopy, as the frequency noise power is related to r^2.

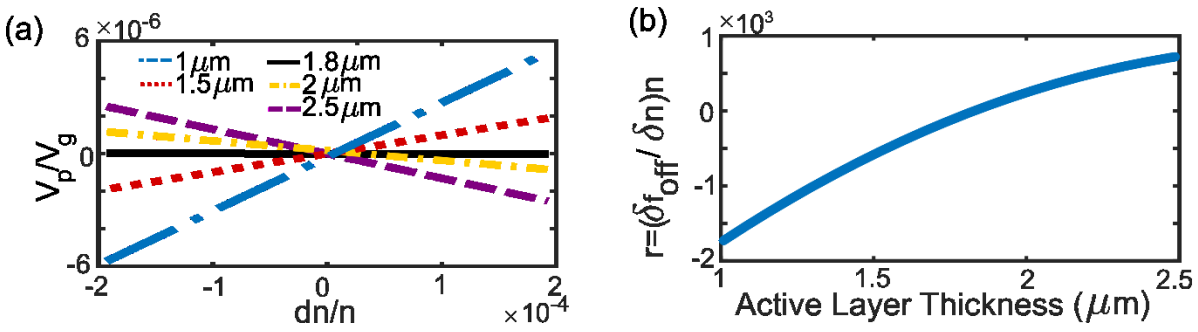

Figure 6- 4. A) Ratio of phase and group velocities for varying active layer thicknesses. The curves are shifted along vertical axis to have a common origin, so that the slopes are easily compared. B) The rate of frequency drift due to change of refractive index.

Now with this information we can calculate the offset frequency drift vs dx/x. A comprehensive picture of the results is presented in Figure 6-5 which is composed of four plots for five different active layer thicknesses. The first column of plots in Figure 6-5a shows the modeled and fitted (to the power-law (6.7)) dispersions , subtracting a fit to the first order to more easily identify the match between our effective propagation constant (k) (shown in blue) and a power law fit (k_α) (shown in red and dashed). The value of α , regardless of waveguide thickness, is 1.033, determined primarily by the material dispersion. Figure 6-5b shows the resulting frequency offset as calculated according to Eq (6.5) . As expected, the offset frequency experiences a jump each time the environmentally-caused frequency shift exceeds the FSR combined with a gradual slope between jumps. Figure 6-5c is a zoomed version of the second column and displays the offset frequency over a single FSR. Finally, Figure 6-5d shows the calculated GVD. This clearly highlights the conflict between achieving a low GVD (as illustrated with a $2.5\mu m$ thickness) and a stable frequency offset (illustrated by a $1.8\mu m$ thickness).

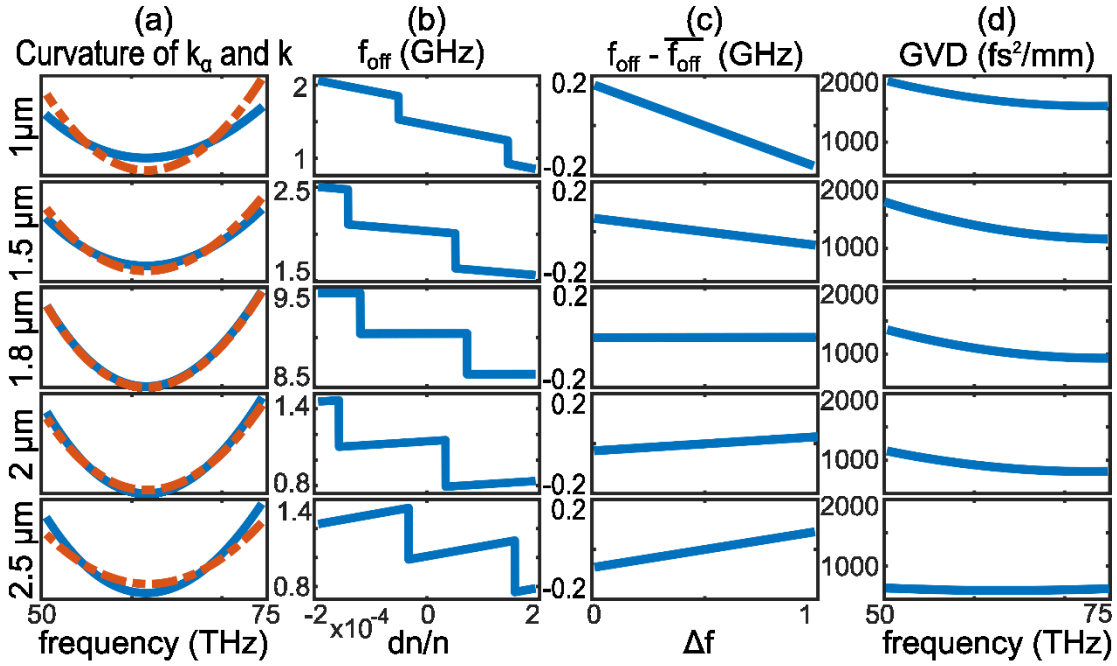

Figure 6- 5. A) Waveguide dispersion and power-law fit. B) Offset drift versus change in refractive index and (C) zoom of offset frequency drift and D) GVD.

Impact of the residual GVD

It is apparent that when designing for a power law dispersion, the resulting GVD will not be zero. It is therefore worthwhile to estimate the effects of residual GVD on the FC. Focusing on cavity dispersion, and thus omitting the FWM terms from equations in [5], we can write the expression for the temporal development of the m^{th} mode amplitude

$$\frac{dA_m}{d\tau} = A_m[G-1+jD], \qquad (6.8)$$

where the mode index is counted from the central frequency, time is normalized to the photon lifetime t_c, G is normalized gain, $D = \Delta\omega_m t_c$ is the dispersion-related phase shift accumulated over the photon

lifetime, and $\Delta\omega_m$ is the difference between the actual frequency of the m^{th} mode ω_m and the m^{th} line of the FC. In the presence of GVD, β_2 can be found as

$$\Delta\omega_m = \omega_m - m\Delta\omega = \frac{1}{2}m^2\Delta\omega^2\beta_2 v_g, \qquad (6.9)$$

where $\Delta\omega = 2\pi\Delta f$. Now, if the comb bandwidth is B, the maximum value of m is $B/2\Delta f$, and the maximum value of the dispersion term in (6.8) is

$$D_{\max} = \frac{\pi^2}{2}B^2\beta_2 v_g t_c. \quad (6.10)$$

Substituting the roundtrip time $t_{rt} = \Delta f^{-1} = 2L/v_g$, one finally obtains

$$D_{\max} = \pi^2 B^2 \frac{t_c}{t_{rt}} L\beta_2. \quad (6.11)$$

The ratio $t_c / t_{rt} = F/2\pi$, where F is the finesse of the cavity. In QCLs this ratio is actually less than unity due to large loss in the waveguide. For example in the QCL of [105] $t_{rt} = 100\,ps$ while $t_c = 26\,ps$. Conservatively, we can assume this ratio to be 1. Then for dispersion to have small impact on the bandwidth we can demand $D_{\max} \le 1/2$ and the dispersion limited bandwidth of comb becomes

$$B \le \frac{1}{\pi\sqrt{2L\beta_2}}. \quad (6.12)$$

Plugging in numbers from Figure 6-5, $\beta_2 \sim 2000\,fs^2/mm$ and L=4.5mm we get a bandwidth of 2.3 THz, actually wider than most experimentally measured combs. We can therefore assert that the residual GVD will not be detrimental to the width of the comb, essentially the same conclusion as the one obtained in [85].

We have shown that despite the common belief that the best FC generating QCLs must be designed for low GVD, this may not be the best practice for obtaining absolute frequency measurements with ease. Although GVD may be low, a variability in the ratio of phase and group velocities causes a drift in the offset frequency, given some perturbation such as temperature fluctuation or carrier density. We have shown analytically that one can achieve a perfect zero offset frequency drift and reduced phase noise, as long as external perturbation is relatively small and the oscillation frequency does not change by more than the order of a single FSR. Furthermore, by performing numerical modeling of the waveguide dispersion we have demonstrated that cancellation of the offset frequency drift can be accomplished by simply choosing the proper geometrical parameters of the waveguide. However, each optical set up is different and in order for this to work experimentally, careful measurements must be taken on the system such that further external perturbations (such as optical feedback, or parasitic GTIs) are also compensated for. Hopefully, these results will facilitate all type of precision measurements with QCL and other frequency combs.

Conclusion

In summary, this body of work provides a theoretical groundwork for predicting the operational characteristics of a free-running QCL laser that produces coherent frequency combs with an emission that is both frequency and, somewhat less so, amplitude modulated. Through a simple time-domain model derived from the Maxwell-Bloch equations we are able to calculate the efficiency of the laser under various emission profiles of the frequency and amplitude modulation. The operational scenario with the highest gain will effectively have the lowest threshold, and will thus be the first regime to lase. We identify the importance of spatial hole burning on the time domain profile, and analyzed the effect of spectral hole burning through inhomogenous broadening. We confirm theoretically that the experimentally seen frequency ramp QCL FCs are a result of dominant spatial hole burning with very little spectral hole burning. In this scenario the chirped FM profile [40, 55] is the most efficient to reduce spatial hole burning. Using a previously developed frequency domain model [5] we are able to confirm the stability of a ramped FM signal with a quadratic relationship between phases.

As phase coherence is of the utmost importance to the applicability of FCs the next major grouping in this dissertation concerns studying the phase noise and offering a method to improve the stability and noise levels of the QCL FCs. First we offer a fairly straightforward derivation of the beatnote linewidth in a FC producing QCL. We show that despite the fact that the phases of the multiple modes are not equal, the linewidth is still narrow because of the locked phase relation between modes. Thus, a narrow linewidth can be achieved by a free-running QCL with a quadratic phase relation of modes just as it can be achieved by a saturable

absorber. Thus the time-domain profile of the laser emission is irrelevant to the laser linewidth. Thus free-running QCLs have the potential to have a frequency comb comparable with more developed methods combined with a much higher simplicity and efficiency of a QCL. Now, reducing phase noise in a QCL is often achieved with active locking [92], a modulation of the injection current. Unfortunately this also significantly narrows the resulting FC. Here we present a much more natural and less intrusive method for reducing phase noise in which we design the cavity to have a dispersion that follows the so called power law dispersion. In other words the ratio of the group and phase velocities stays equal with wavelength. This can be easily achieved with the design of the cavity dispersion and will still result in a broad, free-running QCL. It is the hope of the author that this work will help influence the way other scientists approach this somewhat mysterious scientific problem resulting in more stable and reproducible spectroscopic systems in the Infrared and Terahertz.

References

1. Hugi, A., et al., *Mid-infrared frequency comb based on a quantum cascade laser.* Nature, 2012. **492**(7428): p. 229-233.
2. Hall, J.L., *Nobel Lecture: Defining and measuring optical frequencies.* Reviews of Modern Physics, 2006. **78**(4): p. 1279.
3. Hänsch, T.W., *Nobel lecture: passion for precision.* Reviews of Modern Physics, 2006. **78**(4): p. 1297.
4. Burghoff, D., et al., *Terahertz laser frequency combs.* Nature Photonics, 2014. **8**(6): p. 462-467.
5. Khurgin, J., et al., *Coherent frequency combs produced by self frequency modulation in quantum cascade lasers.* Applied Physics Letters, 2014. **104**(8): p. 081118.
6. Arthur, J. and J. LePore, *GaAs, GaP, and GaAs x P 1− x Epitaxial Films Grown by Molecular Beam Deposition.* Journal of Vacuum Science and Technology, 1969. **6**(4): p. 545-548.
7. Cho, A.Y., *Film deposition by molecular-beam techniques.* Journal of Vacuum Science and Technology, 1971. **8**(5): p. S31-S38.
8. Gornik, E. and D. Tsui, *Voltage-tunable far-infrared emission from Si inversion layers.* Physical Review Letters, 1976. **37**(21): p. 1425.
9. West, L. and S. Eglash, *First observation of an extremely large-dipole infrared transition within the conduction band of a GaAs quantum well.* Applied Physics Letters, 1985. **46**(12): p. 1156-1158.
10. Levine, B., et al., *New 10 μm infrared detector using intersubband absorption in resonant tunneling GaAlAs superlattices.* Applied physics letters, 1987. **50**(16): p. 1092-1094.
11. Faist, J., et al., *Quantum cascade laser.* Science, 1994. **264**(5158): p. 553-556.
12. Khurgin, J.B., et al., *Role of interface roughness in the transport and lasing characteristics of quantum-cascade lasers.* Applied Physics Letters, 2009. **94**(9): p. 091101.
13. Khurgin, J.B. and Y. Dikmelik, *Transport and gain in a quantum cascade laser: model and equivalent circuit.* Optical Engineering, 2010. **49**(11): p. 111110.
14. Hecht, J., *The Birth of the Diode Laser.* Optics and photonics news, 2007. **18**(7): p. 38-43.
15. Kazarinov, R. and R. Suris, *Electric and electromagnetic properties of semiconductors with a superlattice.* Soviet Physics Semiconductors-USSR, 1972. **6**(1): p. 120-+.
16. Sun, G. and J.B. Khurgin, *Optically pumped four-level infrared laser based on intersubband transitions in multiple quantum wells: feasibility study.* IEEE journal of quantum electronics, 1993. **29**(4): p. 1104-1111.
17. Vitiello, M.S., et al., *Quantum cascade lasers: 20 years of challenges.* Optics express, 2015. **23**(4): p. 5167-5182.
18. Ishida, A., et al., *AlN/GaN near-infrared quantum-cascade structures with resonant-tunneling injectors utilizing polarization fields.* Japanese journal of applied physics, 2002. **41**(11B): p. L1303.
19. Beck, M., et al., *Continuous wave operation of a mid-infrared semiconductor laser at room temperature.* Science, 2002. **295**(5553): p. 301-305.

20. Köhler, R., et al., *Terahertz semiconductor-heterostructure laser.* Nature, 2002. **417**(6885): p. 156-159.
21. Williams, B.S., et al., *3.4-THz quantum cascade laser based on longitudinal-optical-phonon scattering for depopulation.* Applied Physics Letters, 2003. **82**(7): p. 1015-1017.
22. Kainz, M.A., et al., *Thermoelectric-cooled terahertz quantum cascade lasers.* Optics express, 2019. **27**(15): p. 20688-20693.
23. Troccoli, M., et al., *High-performance quantum cascade lasers grown by metal-organic vapor phase epitaxy and their applications to trace gas sensing.* Journal of Lightwave Technology, 2008. **26**(21): p. 3534-3555.
24. Schnatz, H., et al., *First phase-coherent frequency measurement of visible radiation.* Physical Review Letters, 1996. **76**(1): p. 18.
25. Udem, T., R. Holzwarth, and T.W. Hänsch, *Optical frequency metrology.* Nature, 2002. **416**(6877): p. 233-237.
26. Bartels, A., D. Heinecke, and S.A. Diddams, *10-GHz self-referenced optical frequency comb.* Science, 2009. **326**(5953): p. 681-681.
27. Fujii, S. and T. Tanabe, *Dispersion engineering and measurement of whispering gallery mode microresonator for Kerr frequency comb generation.* Nanophotonics, 2020. **1**(ahead-of-print).
28. Opačak, N. and B. Schwarz, *Theory of Frequency-Modulated Combs in Lasers with Spatial Hole Burning, Dispersion, and Kerr Nonlinearity.* Physical Review Letters, 2019. **123**(24): p. 243902.
29. Villares, G., et al., *Dispersion engineering of quantum cascade laser frequency combs.* Optica, 2016. **3**(3): p. 252-258.
30. Pal, P., et al., *Self referenced Yb-fiber-laser frequency comb using a dispersion micromanaged tapered holey fiber.* Optics express, 2007. **15**(19): p. 12161-12166.
31. Bidaux, Y., et al., *Coupled-Waveguides for Dispersion Compensation in Semiconductor Lasers.* Laser & Photonics Reviews, 2018. **12**(5): p. 1700323.
32. Bidaux, Y., et al., *Plasmon-enhanced waveguide for dispersion compensation in mid-infrared quantum cascade laser frequency combs.* Optics letters, 2017. **42**(8): p. 1604-1607.
33. Schiller, S., *Spectrometry with frequency combs.* Optics letters, 2002. **27**(9): p. 766-768.
34. Schliesser, A., N. Picqué, and T.W. Hänsch, *Mid-infrared frequency combs.* Nature Photonics, 2012. **6**(7): p. 440.
35. Hugi, A., et al., *External cavity quantum cascade laser tunable from 7.6 to 11.4 μ m.* Applied Physics Letters, 2009. **95**(6): p. 061103.
36. Walrod, D., et al., *Observation of third order optical nonlinearity due to intersubband transitions in AlGaAs/GaAs superlattices.* Applied physics letters, 1991. **59**(23): p. 2932-2934.
37. Friedli, P., et al., *Four-wave mixing in a quantum cascade laser amplifier.* Applied Physics Letters, 2013. **102**(22): p. 222104.
38. Tiemeijer, L.F., et al., *Passive FM locking in InGaAsP semiconductor lasers.* IEEE Journal of Quantum Electronics, 1989. **25**(6): p. 1385-1392.
39. Burghoff, D., et al., *Evaluating the coherence and time-domain profile of quantum cascade laser frequency combs.* Optics express, 2015. **23**(2): p. 1190-1202.

40. Singleton, M., et al., *Evidence of linear chirp in mid-infrared quantum cascade lasers.* Optica, 2018. **5**(8): p. 948-953.
41. Tang, C. and H. Statz, *Maximum-emission principle and phase locking in multimode lasers.* Journal of Applied Physics, 1967. **38**(7): p. 2963-2968.
42. Khurgin, J.B., et al., *Linewidth of the laser optical frequency comb with arbitrary temporal profile.* Applied Physics Letters, 2018. **113**(13): p. 131104.
43. Schwarz, S. and P. Gordon, *Hamilton's Principle and the Maximum-Emission Coincidence.* Journal of Applied Physics, 1969. **40**(11): p. 4441-4447.
44. Anderson, D., *Variational approach to nonlinear pulse propagation in optical fibers.* Physical review A, 1983. **27**(6): p. 3135.
45. Duda, B.J. and W.B. Mori, *Variational principle approach to short-pulse laser-plasma interactions in three dimensions.* Physical Review E, 2000. **61**(2): p. 1925.
46. Piccardo, M., et al., *Frequency-modulated combs obey a variational principle.* Physical Review Letters, 2019. **122**(25): p. 253901.
47. Henry, N., et al., *Pseudorandom dynamics of frequency combs in free-running quantum cascade lasers.* Optical Engineering, 2017. **57**(1): p. 011009.
48. Kumar, S., Q. Hu, and J.L. Reno, *186 K operation of terahertz quantum-cascade lasers based on a diagonal design.* Applied Physics Letters, 2009. **94**(13): p. 131105.
49. Burghoff, D., et al., *A terahertz pulse emitter monolithically integrated with a quantum cascade laser.* Applied Physics Letters, 2011. **98**(6): p. 061112.
50. Burghoff, D., et al., *Gain measurements of scattering-assisted terahertz quantum cascade lasers.* Applied Physics Letters, 2012. **100**(26): p. 261111.
51. Kohen, S., B.S. Williams, and Q. Hu, *Electromagnetic modeling of terahertz quantum cascade laser waveguides and resonators.* Journal of applied physics, 2005. **97**(5): p. 053106.
52. Tzenov, P., et al., *Time domain modeling of terahertz quantum cascade lasers for frequency comb generation.* Optics express, 2016. **24**(20): p. 23232-23247.
53. Mansuripur, T.S., et al., *Single-mode instability in standing-wave lasers: The quantum cascade laser as a self-pumped parametric oscillator.* Physical Review A, 2016. **94**(6): p. 063807.
54. Columbo, L. and M. Brambilla, *Multimode regimes in quantum cascade lasers with optical feedback.* Optics Express, 2014. **22**(9): p. 10105-10118.
55. Burghoff, D. *Terahertz quantum cascade laser frequency combs*. in *2018 IEEE International Semiconductor Laser Conference (ISLC)*. 2018. IEEE.
56. Choi, H., et al., *Gain recovery dynamics and photon-driven transport in quantum cascade lasers.* Physical review letters, 2008. **100**(16): p. 167401.
57. Gelmont, B., V. Gorfinkel, and S. Luryi, *Theory of the spectral line shape and gain in quantum wells with intersubband transitions.* Applied physics letters, 1996. **68**(16): p. 2171-2173.
58. Owschimikow, N., et al., *Resonant second-order nonlinear optical processes in quantum cascade lasers.* Physical review letters, 2003. **90**(4): p. 043902.
59. Aellen, T., et al., *Doping in quantum cascade lasers. I. In Al As–In Ga As⁄ In P midinfrared devices.* Journal of applied physics, 2006. **100**(4): p. 043101.

60. Fujita, K., et al., *High-Performance Quantum Cascade Lasers With λ~8.6 μm Single Phonon-Continuum Depopulation Structures.* IEEE Journal of Quantum Electronics, 2010. **46**(5): p. 683-688.
61. Kočinac, S., et al., *Gain optimization in electrically pumped AlGaAs quantum cascade lasers.* JOSA B, 2002. **19**(10): p. 2357-2364.
62. Gmachl, C., et al., *Continuous-wave and high-power pulsed operation of index-coupled distributed feedback quantum cascade laser at λ≈ 8.5 μ m.* Applied physics letters, 1998. **72**(12): p. 1430-1432.
63. Meng, B., et al., *Mid-infrared frequency comb from a ring quantum cascade laser.* Optica, 2020. **7**(2): p. 162-167.
64. Barbieri, S., et al., *Coherent sampling of active mode-locked terahertz quantum cascade lasers and frequency synthesis.* Nature Photonics, 2011. **5**(5): p. 306.
65. Revin, D., et al., *Active mode locking of quantum cascade lasers in an external ring cavity.* Nature Communications, 2016. **7**(1): p. 1-7.
66. Barbieri, S., et al., *Phase-locking of a 2.7-THz quantum cascade laser to a mode-locked erbium-doped fibre laser.* Nature Photonics, 2010. **4**(9): p. 636-640.
67. Udem, T., et al., *Absolute optical frequency measurement of the cesium D 1 line with a mode-locked laser.* Physical review letters, 1999. **82**(18): p. 3568.
68. Diddams, S.A., et al., *Direct link between microwave and optical frequencies with a 300 THz femtosecond laser comb.* Physical review letters, 2000. **84**(22): p. 5102.
69. Fortier, T.M., A. Bartels, and S.A. Diddams, *Octave-spanning Ti: sapphire laser with a repetition rate> 1 GHz for optical frequency measurements and comparisons.* Optics Letters, 2006. **31**(7): p. 1011-1013.
70. Jones, D.J., et al., *Carrier-envelope phase control of femtosecond mode-locked lasers and direct optical frequency synthesis.* Science, 2000. **288**(5466): p. 635-639.
71. Fatemi, F., J. Lou, and T. Carruthers, *Frequency comb linewidth of an actively mode-locked fiber laser.* Optics letters, 2004. **29**(9): p. 944-946.
72. Del'Haye, P., et al., *Optical frequency comb generation from a monolithic microresonator.* Nature, 2007. **450**(7173): p. 1214-1217.
73. Kippenberg, T.J., R. Holzwarth, and S.A. Diddams, *Microresonator-based optical frequency combs.* science, 2011. **332**(6029): p. 555-559.
74. Wang, C.Y., et al., *Mid-infrared optical frequency combs at 2.5 μm based on crystalline microresonators.* Nature communications, 2013. **4**(1): p. 1-7.
75. Herr, T., et al., *Universal formation dynamics and noise of Kerr-frequency combs in microresonators.* Nature photonics, 2012. **6**(7): p. 480-487.
76. Griffith, A.G., et al., *Silicon-chip mid-infrared frequency comb generation.* Nature communications, 2015. **6**(1): p. 1-5.
77. Brasch, V., et al., *Photonic chip–based optical frequency comb using soliton Cherenkov radiation.* Science, 2016. **351**(6271): p. 357-360.
78. Rush, D., G. Burdge, and P.-T. Ho, *The linewidth of a mode-locked semiconductor laser caused by spontaneous emission: experimental comparison to single-mode operation.* IEEE journal of quantum electronics, 1986. **22**(11): p. 2088-2091.
79. Ho, P.-T., *Phase and amplitude fluctuations in a mode-locked laser.* IEEE journal of quantum electronics, 1985. **21**(11): p. 1806-1813.

80. Haus, H.A. and A. Mecozzi, *Noise of mode-locked lasers.* IEEE Journal of Quantum Electronics, 1993. **29**(3): p. 983-996.
81. Jiang, L.A., et al., *Noise of mode-locked semiconductor lasers.* IEEE Journal of Selected Topics in Quantum Electronics, 2001. **7**(2): p. 159-167.
82. Schawlow, A.L. and C.H. Townes, *Infrared and optical masers.* Physical Review, 1958. **112**(6): p. 1940.
83. Lax, M., *Classical noise. V. Noise in self-sustained oscillators.* Physical Review, 1967. **160**(2): p. 290.
84. Mullen, J.A., *Background noise in nonlinear oscillators.* Proceedings of the IRE, 1960. **48**(8): p. 1467-1473.
85. Villares, G. and J. Faist, *Quantum cascade laser combs: effects of modulation and dispersion.* Optics express, 2015. **23**(2): p. 1651-1669.
86. Henry, C., *Theory of the linewidth of semiconductor lasers.* IEEE Journal of Quantum Electronics, 1982. **18**(2): p. 259-264.
87. Cappelli, F., et al., *Intrinsic linewidth of quantum cascade laser frequency combs.* Optica, 2015. **2**(10): p. 836-840.
88. Klocke, J.L., et al., *Single-shot sub-microsecond mid-infrared spectroscopy on protein reactions with quantum cascade laser frequency combs.* Analytical chemistry, 2018. **90**(17): p. 10494-10500.
89. Scalari, G., J. Faist, and N. Picqué, *On-chip mid-infrared and THz frequency combs for spectroscopy.* Applied Physics Letters, 2019. **114**(15): p. 150401.
90. Hillbrand, J., et al., *Coherent injection locking of quantum cascade laser frequency combs.* Nature Photonics, 2019. **13**(2): p. 101-104.
91. Villares, G., et al., *Dual-comb spectroscopy based on quantum-cascade-laser frequency combs.* Nature communications, 2014. **5**(1): p. 1-9.
92. Consolino, L., et al., *Fully phase-stabilized quantum cascade laser frequency comb.* Nature communications, 2019. **10**(1): p. 1-7.
93. Telle, H.R., B. Lipphardt, and J. Stenger, *Kerr-lens, mode-locked lasers as transfer oscillators for optical frequency measurements.* Applied Physics B, 2002. **74**(1): p. 1-6.
94. Adler, F., et al., *Phase-stabilized, 1.5 W frequency comb at 2.8–4.8 μm.* Optics letters, 2009. **34**(9): p. 1330-1332.
95. Reichert, J., et al., *Measuring the frequency of light with mode-locked lasers.* Optics communications, 1999. **172**(1-6): p. 59-68.
96. Schilt, S., et al., *Fully stabilized optical frequency comb with sub-radian CEO phase noise from a SESAM-modelocked 1.5-μm solid-state laser.* Optics express, 2011. **19**(24): p. 24171-24181.
97. Di Domenico, G., S. Schilt, and P. Thomann, *Simple approach to the relation between laser frequency noise and laser line shape.* Applied optics, 2010. **49**(25): p. 4801-4807.
98. Burghoff, D., Y. Yang, and Q. Hu, *Computational multiheterodyne spectroscopy.* Science advances, 2016. **2**(11): p. e1601227.
99. Sterczewski, L.A., J. Westberg, and G. Wysocki, *Computational coherent averaging for free-running dual-comb spectroscopy.* Optics express, 2019. **27**(17): p. 23875-23893.
100. Hillbrand, J., et al., *Tunable dispersion compensation of quantum cascade laser frequency combs.* Optics letters, 2018. **43**(8): p. 1746-1749.

101. Henry, N.C., D. Burghoff, and J.B. Khurgin, *Mitigating offset frequency drift in frequency combs using a customized power law dispersion.* Optics Letters, 2020. **45**(13): p. 3525-3528.
102. Melati, D., et al., *Wavelength and composition dependence of the thermo-optic coefficient for InGaAsP-based integrated waveguides.* Journal of Applied Physics, 2016. **120**(21): p. 213102.
103. Della Corte, F.G., et al., *Temperature dependence of the thermo-optic coefficient of InP, GaAs, and SiC from room temperature to 600 K at the wavelength of 1.5 μm.* Applied Physics Letters, 2000. **77**(11): p. 1614-1616.
104. Burghoff, D., et al., *Microelectromechanical control of the state of quantum cascade laser frequency combs.* Applied Physics Letters, 2019. **115**(2): p. 021105.
105. Yang, Q., et al., *onHigh-peak-power strain-compensated GaInAs/AlInAs quantum cascade lasers (λ ∼ 4.6 μ m) based on a slightly diagonal active region design.* Applied Physics Letters, 2008. **93**(25): p. 251110.
106. Adachi, S., *Optical dispersion relations for GaP, GaAs, GaSb, InP, InAs, InSb, Al x Ga1− x As, and In1− x Ga x As y P1− y.* Journal of Applied Physics, 1989. **66**(12): p. 6030-6040.

Biographic Statement and Publications

Nathan's background is in optoelectronics and semiconductor physics, a field in which he has worked for over a decade. As a junior studying for his bachelor's degree, Nathan began working under the tutelage of Dr. Sanjay Krishna where he discovered his interests in optoelectronics and semiconductor fabrication. After graduating with his bachelor's degree he began work at Night Vision Electronic Sensors Directorate (NVESD), where he performed research on fabrication methods to develop a relatively novel infrared focal plane array material system based on III-V superlattices. These cameras are typically fairly large and used primarily on vehicles, they must be cooled to low temperatures and require a lot of optics. Cameras developed from this program are now being utilized by the army today. He soon realized he wanted to further develop my education and in 2015 began his PhD program at Johns Hopkins University.

Aside from work Nathan is an avid outdoor enthusiast. Often seen hanging from cliff-sides on a rope, camping in the middle of nowhere, or snowboarding through the trees.

Publications

1. Henry, N.C., D. Burghoff, and J.B. Khurgin, Mitigating offset frequency drift in frequency combs using a customized power law dispersion. Optics Letters, 2020. 45(13): p. 3525-3528.

2. Knorr Jr, D.B., et al., Method of passivating and encapsulating III-V surfaces. 2019, US Patent 10,355,150.

3. Henry, N., et al., Study of Spatio-Temporal Character of Frequency Combs Generated by Quantum Cascade Lasers. IEEE Journal of Selected Topics in Quantum Electronics, 2019. 25(6): p. 1-9.

4. Burghoff, D., et al., Microelectromechanical control of the state of quantum cascade laser frequency combs. Applied Physics Letters, 2019. 115(2): p. 021105.

5. Burghoff, D., et al. Optomechanical Control of the State of Chip-Scale Frequency Combs. in CLEO: Science and Innovations. 2019. Optical Society of America.

6. Burghoff, D., et al. Optomechanical control of quantum cascade laser frequency combs. in Novel In-Plane Semiconductor Lasers XVIII. 2019. International Society for Optics and Photonics.

7. Knorr Jr, D., et al., Bonding of cysteamine on InAs surfaces. Applied Surface Science, 2018. 462: p. 489-501.

8. Khurgin, J.B., et al., Linewidth of the laser optical frequency comb with arbitrary temporal profile. Applied Physics Letters, 2018. 113(13): p. 131104.

9. Henry, N.C. and J.B. Khurgin. The Role of Spatial and Spectral Hole Burning in QCL Frequency Comb Formation. in CLEO: Science and Innovations. 2018. Optical Society of America.

10. Henry, N., et al., Temporal characteristics of quantum cascade laser frequency modulated combs in long wave infrared and THz regions. Optics express, 2018. 26(11): p. 14201-14212.

11. Henry, N. and J.B. Khurgin. Time domain analysis of self-frequency modulated combs in quantum cascade lasers. in CLEO: Science and Innovations. 2017. Optical Society of America.

12. Henry, N. and J.B. Khurgin. Time domain model for Quantum Cascade lasers generating frequency combs via stochastic frequency modulation. in 2017 51st Annual Conference on Information Sciences and Systems (CISS). 2017. IEEE.

13. Henry, N., et al., Pseudorandom dynamics of frequency combs in free-running quantum cascade lasers. Optical Engineering, 2017. 57(1): p. 011009.

14. Henry, N.C., et al., Surface conductivity of InAs/GaSb superlattice infrared detectors treated with thiolated self assembled monolayers. Applied Physics Letters, 2016. 108(1): p. 011606.

15. Henry, N.C., et al., Chemical and physical passivation of type II strained-layer superlattice devices by means of thiolated self-assembled monolayers and polymer encapsulates. Infrared Physics & Technology, 2015. 70: p. 48-52.

16. Baril, N., et al., Low operating bias InAs/GaSb strain layer superlattice LWIR detector. Infrared Physics & Technology, 2015. 70: p. 58-61.

17. Williams, K.S., et al., First principles investigation of water adsorption and charge transfer on III–V (110) semiconductor surfaces. Surface science, 2014. 622: p. 71-82.

18. Knorr Jr, D.B., et al., Use of 3-aminopropyltriethoxysilane deposited from aqueous solution for surface modification of III-V materials. Applied surface science, 2014. 320: p. 414-428.

19. Gautam, N., et al., Band engineered HOT midwave infrared detectors based on type-II InAs/GaSb strained layer superlattices. Infrared Physics & Technology, 2013. 59: p. 72-77.